

# Analysis and Optimisation of a Receiver Tube for Direct Steam Generation in a Solar Parabolic Trough Collector

by

**Henriette Christine Nolte**

Submitted in partial fulfilment  
of the requirements for the degree

**Master of Engineering**

in the

Department of Mechanical and Aeronautical Engineering  
Faculty of Engineering, Built Environment and Information Technology

University of Pretoria  
Pretoria

Supervisors: Prof T Bello-Ochende and Prof JP Meyer

**November 2014**

---

# ABSTRACT

- Title:** Analysis and Optimisation of a Receiver Tube for Direct Steam Generation in a Solar Parabolic Trough Collector
- Author:** Henriette Christine Nolte
- Supervisors:** Prof. T. Bello-Ochende  
Prof. J.P. Meyer
- Department:** Department of Mechanical and Aeronautical Engineering
- Degree:** Master of Engineering
- Keywords:** Solar Thermal Energy, Direct Steam Generation (DSG), Receiver Tube, Two-Phase Flow, Second Law Analysis, Entropy Generation, Optimisation.

This study focused on a numerical second law analysis and optimisation of a receiver tube operating in a parabolic trough solar collector for small-scale application. The receiver functioned in a Rankine cycle. The focus was on entropy generation minimisation in the receiver due to the high quality exergy losses in this component. Water functioned as the working fluid and was heated from ambient conditions (liquid) to a superheated state (vapour), consequently, the receiver tube was subject to both single phase as well as two-phase flow.

Entropy generation in the receiver tube was mainly due to finite temperature differences as well as fluid friction. The contribution of each of these components was investigated. Geometrical as well as operating conditions were investigated to obtain good guidelines for receiver tube and plant design. An operating pressure in the range of 1 *MPa* ( $T_{sat} = 180^{\circ}\text{C}$ ) to 10 *MPa* ( $T_{sat} = 311^{\circ}\text{C}$ ) was considered. Furthermore a mass flow range of 0.15 *kg/s* to 0.4 *kg/s* was investigated.

## ABSTRACT

---

Results showed that beyond a diameter of 20 *mm*, the main contributor to the entropy generation was the finite temperature differences for most conditions. Generally, operating pressures below 3 *MPa* showed bad performance since the fluid friction component was too large for small operating pressures. This phenomenon was due to long two-phase lengths and high pressure drops in this region. The finite temperature difference component increased linearly when the tube diameter was increased (due to the increase in exposed area) if the focused heat flux was kept constant. However, the fluid friction component increased quadratically when the diameter was reduced.

In general when the concentration ratio was increased, the entropy generation was decreased. This was due to more focused heat on each section of the receiver pipe and, in general, resulted in shorter receiver lengths. Unfortunately, there is a limit to the highest concentration ratio that can be achieved and in this study, it was assumed to be 45 for two-dimensional trough technology.

A Simulated Annealing (SA) optimisation algorithm was implemented to obtain certain optimum parameters. The optimisation showed that increasing the diameter could result in a decrease in entropy generation, provided that the concentration ratio is kept constant. However, beyond a certain point gains in minimising the entropy generation became negligible. Optimal operating pressure would generally increase if the mass flow rate was increased. Finally, it was seen that the highest operating pressure under consideration (10 *MPa*) showed the best performance when considering the minimisation of entropy in conjunction with the maximisation of the thermodynamic work output.

---

# ACKNOWLEDGEMENTS

- I would like to thank the University of Pretoria, University of Stellenbosch, NRF, TESP, SANERI/SANEDI, CSIR, EEDSM hub and NAC for the funding during the course of this work.
- I would also like to express my gratitude towards my supervisors Prof T Bello-Ochende and Prof JP Meyer for their invaluable advice and guidance during the course of this work.
- I would like to thank N Botha for her insight and help during the course of this work.
- I would also like to thank my fellow students for their help and insights.
- Finally I would like to thank my family for their support.

---

# CONTENTS

<b>Abstract</b>	<b>i</b>
<b>Acknowledgements</b>	<b>iii</b>
<b>Nomenclature</b>	<b>viii</b>
<b>List of Figures</b>	<b>xv</b>
<b>List of Tables</b>	<b>xix</b>
<b>1 INTRODUCTION</b>	<b>1</b>
1.1 BACKGROUND . . . . .	1
1.2 PROBLEM STATEMENT . . . . .	2
1.3 PURPOSE OF STUDY . . . . .	3
1.4 OUTLINE OF DISSERTATION . . . . .	3
1.4.1 CHAPTER 2: Literature Review . . . . .	3
1.4.2 CHAPTER 3: Numerical Work . . . . .	3
1.4.3 CHAPTER 4: Results . . . . .	3
1.4.4 CHAPTER 5: Optimisation . . . . .	4
1.4.5 CHAPTER 6: Conclusion . . . . .	4

## CONTENTS

---

<b>2</b>	<b>LITERATURE REVIEW</b>	<b>5</b>
2.1	INTRODUCTION . . . . .	5
2.2	SOLAR COLLECTORS . . . . .	5
2.3	SUN-TRACKING . . . . .	7
2.4	ENERGY CYCLES . . . . .	9
2.5	PARABOLIC TROUGH COLLECTORS . . . . .	11
2.6	RECEIVER THERMAL ANALYSIS . . . . .	14
2.6.1	Bare Tube . . . . .	14
2.6.2	Glass-covered Tube . . . . .	17
2.7	TWO-PHASE FLOW . . . . .	19
2.7.1	Two-Phase Heat Transfer . . . . .	19
2.7.2	Two-Phase Pressure Drop . . . . .	25
2.8	SECOND LAW ANALYSIS . . . . .	27
2.8.1	Finite Temperature Differences . . . . .	27
2.8.2	Fluid Friction . . . . .	27
2.8.3	Exergy Destruction in Collectors . . . . .	29
2.8.4	Entropy Generation in Isothermal Collectors . . . . .	31
2.8.5	Non-Isothermal Collectors . . . . .	32
2.8.6	Internal Flow Entropy Generation . . . . .	32
2.8.7	Bejan Number . . . . .	33
2.9	CONCLUSION . . . . .	33
<b>3</b>	<b>NUMERICAL WORK</b>	<b>34</b>
3.1	INTRODUCTION . . . . .	34
3.1.1	Single-Phase Region . . . . .	34
3.1.2	Two-Phase Region . . . . .	35

## CONTENTS

---

3.2	ASSUMPTIONS . . . . .	35
3.3	OPERATING PRESSURES . . . . .	35
3.4	FLUID PROPERTIES . . . . .	36
3.5	INITIAL CONDITIONS . . . . .	37
3.6	OPTICAL EFFICIENCY AND CONCENTRATION RATIO . . . . .	38
3.7	LIQUID REGION . . . . .	39
3.7.1	Solution Process . . . . .	39
3.7.2	Validation . . . . .	41
3.8	TWO-PHASE REGION . . . . .	45
3.8.1	Solution Process . . . . .	45
3.8.2	Validation . . . . .	47
3.9	VAPOUR REGION . . . . .	48
3.9.1	Solution Process . . . . .	48
3.9.2	Validation . . . . .	51
3.10	CONCLUSION . . . . .	51
<b>4</b>	<b>RESULTS</b>	<b>55</b>
4.1	INTRODUCTION . . . . .	55
4.2	REGION LENGTHS . . . . .	55
4.3	ENTROPY GENERATION . . . . .	57
4.3.1	Entropy Generation due to Finite Temperature Differences . . . . .	57
4.3.2	Entropy Generation due to Fluid Friction . . . . .	59
4.3.3	Total Entropy Generation . . . . .	61
4.4	SENSITIVITY ANALYSIS . . . . .	63
4.4.1	Sky Temperature . . . . .	64
4.4.2	Wind Velocity . . . . .	64

## CONTENTS

---

4.4.3	Maximum Focused Heat . . . . .	65
4.4.4	Glass Cover Clearance . . . . .	66
4.5	CONCLUSION . . . . .	67
<b>5</b>	<b>OPTIMISATION</b>	<b>68</b>
5.1	BACKGROUND . . . . .	68
5.2	METHOD . . . . .	70
5.3	RESULTS . . . . .	70
5.3.1	Contour Plot . . . . .	70
5.3.2	Results for Simulated Annealing Optimisation . . . . .	73
5.3.3	Multi-Objective Optimisation . . . . .	75
5.4	CONCLUSION . . . . .	76
<b>6</b>	<b>CONCLUSION</b>	<b>78</b>
6.1	DISCUSSION . . . . .	78
6.2	FUTURE WORK . . . . .	79
<b>A</b>	<b>ADDITIONAL GRAPHS</b>	<b>83</b>
A.1	TWO-PHASE FLOW VALIDATION . . . . .	83
A.2	SENSITIVITY ANALYSIS . . . . .	84
A.3	MULTI-OBJECTIVE OPTIMISATION . . . . .	86

---

# NOMENCLATURE

## Symbols

Symbol	Description	Units
$A$	Cross-sectional area	$m^2$
$A_s$	Exposed heat transfer surface	$m^2$
$A_{LD}$	Dimensionless area occupied by liquid $[A_i(1 - \varepsilon_{void})/D_i^2]$	-
$A_{GD}$	Dimensionless area occupied by vapour $[A_i\varepsilon_{void}/D_i^2]$	-
$Be$	Bejan number	-
$C_p$	Constant pressure specific heat	$J/(kg\ K)$
$C_R$	Concentration ratio	-
$C_{R,ideal,2dim}$	Ideal $C_R$ for 2D focusing	-
$C_{R,ideal,3dim}$	Ideal $C_R$ for 3D focusing	-
$D$	Diameter	$m$
$E_{friedel}$	Friedel correlation dimensionless factor	-
$E$	Exergy	$W$

NOMENCLATURE
 

---

Symbol	Description	Units
$E_{des}$	Destroyed exergy	$W$
$E_{bz}$	Boltzmann energy	-
$F$	View factor	-
$F_a$	Incident angle modifier	-
$F_{friedel}$	Friedel correlation dimensionless factor	-
$Fr_{H,friedel}$	Friedel correlation dimensionless factor	-
$Fr_L$	Liquid Froude number [ $G^2/(\rho_L^2 g D_i)$ ]	-
$Fr_G$	Vapour Froude number [ $G^2/(\rho_G^2 g D_i)$ ]	-
$Fr_G$	Vapour Froude number (used by Mori et al.) [ $G^2/(\rho_G g D_i (\rho_L - \rho_G))$ ]	-
$f$	Friction factor	-
$G$	Mass velocity	$kg/(m^2 s)$
$g$	Gravitational constant	$m/s^2$
$H_{friedel}$	Friedel correlation dimensionless factor	-
$h$	Heat transfer coefficient	$W/m^2 K$
$h_{ent}$	Enthalpy	$J/kg$
$h_{fg}$	Enthalpy of vapourisation	$J/kg$
$h_{LD}$	Dimensionless vertical height of liquid	-
$I_b$	Solar beam radiation	$W/m^2$
$k$	Thermal conductivity	$W/(m K)$
$k_{bz}$	Boltzmann constant	-

---

NOMENCLATURE
 

---

$L$	Receiver length	$m$
$M$	Molecular weight	$g/mol$
$\dot{m}$	Mass flow rate	$kg/s$
$Nu$	Nusselt number	-
$p$	Focal length	$m$
$Pr$	Prandtl number	-
$P$	Pressure	$Pa$
$P_{crit}$	Critical pressure	$Pa$
$P_r$	Reduced pressure $P_r = P/P_{crit}$	-
$P_{bz}$	Boltzmann probability	-
$Q$	Heat transfer	$W$
$Q_{fluid}$	Heat transferred to the working fluid	$W$
$q$	Heat flux	$W/m^2$
$q_{crit}$	Critical heat flux of nucleate boiling	$W/m^2$
$r$	Radius	$m$
$r_r$	Rim radius	-
$Ra$	Rayleigh number	-
$Re$	Reynolds number	-
$S_{gen}$	Entropy generation	$W/K$
$S_{gen,dT}$	$S_{gen}$ due to temperature differences	$W/K$
$S_{gen,dP}$	$S_{gen}$ due to fluid friction	$W/K$

---

NOMENCLATURE
 

---

$S_{gen,tot}$	Total entropy generation	$W/K$
$s$	Entropy	$J/(kg K)$
$S_r$	Absorbed solar energy	$W/m^2$
$S_p$	Length of parabolic trough	$m$
$T$	Temperature	$^{\circ}C$ or $K$
$T_H$	High temperature	$^{\circ}C$ or $K$
$T_L$	Low temperature	$^{\circ}C$ or $K$
$T_{\infty}$	Temperature of surroundings	$^{\circ}C$ or $K$
$T_s$	Temperature of surface	$^{\circ}C$ or $K$
$T_f$	Film temperature	$^{\circ}C$ or $K$
$T_{sky}$	Effective sky temperature	$^{\circ}C$ or $K$
$T_{sun}$	Apparent sun temperature	$^{\circ}C$ or $K$
$T_{sun,blackbody}$	Apparent blackbody temperature of the sun	$^{\circ}C$ or $K$
$T_{sat}$	Saturation temperature	$^{\circ}C$ or $K$
$T_w$	Wall temperature	$^{\circ}C$ or $K$
$T_b$	Bulk fluid temperature	$^{\circ}C$ or $K$
$U_r$	Overall heat transfer coefficient	$W/m^2 K$
$V$	Velocity	$m/s$
$\bar{v}$	Local specific volume	$m^3/kg$
$W$	Thermodynamic work	$W$
$W_a$	Aperture area	$m$
$We_L$	Liquid Weber number $[G^2 D_i / (\rho_L \sigma_{surr})]$	-

## NOMENCLATURE

---

$We_{L,friedel}$	Liquid Weber number used by Friedel [ $G^2 D_i / (\rho_H \sigma_{surr})$ ]	-
$We_G$	Vapour Weber number [ $G^2 D_i / (\rho_G \sigma_{surr})$ ]	-
$x$	Quality	% or fraction
$x_{IA}$	Quality that separates intermittent and annular zones	% or fraction
$X$	Design vector	-
$Y$	Two-phase flow multiplying factor	-

## Greek Symbols

Symbol	Description	Units
$\alpha$	Thermal diffusivity	$m^2/s$
$\alpha_{abs}$	Absorptance	-
$\beta$	Thermal expansion coefficient	$1/K$
$\delta$	Liquid film thickness	$m$
$\varepsilon$	Emissivity	-
$\varepsilon_{void}$	Void fraction	-
$\gamma$	Shape factor due to inexact concentration ratio	-
$\eta_{carnot}$	Carnot efficiency	-
$\eta_{opt}$	Optical efficiency	-
$\theta$	Angle of incidence	$rad$
$\theta_r$	Rim angle	$rad$
$\theta_m$	Half-acceptance angle	$rad$

---

## NOMENCLATURE

---

Symbol	Description	Units
$\theta_{dry}$	Dry angle	<i>rads</i>
$\mu$	Dynamic viscosity	<i>kg/(m s)</i>
$\nu$	Kinematic viscosity	<i>m<sup>2</sup>/s</i>
$\rho$	Density	<i>kg/m<sup>3</sup></i>
$\rho$	Density	<i>kg/m<sup>3</sup></i>
$\rho_0$	Surface reflectivity	-
$\sigma$	Stefan-Boltzmann constant	<i>W/(m<sup>2</sup>K<sup>4</sup>)</i>
$\sigma_{surr}$	Surface tension	<i>N/m</i>
$\Phi^2$	Two-phase flow multiplier	-
$\phi_r$	Rim angle	<i>rad</i>
$\tau$	Transmissivity	-

## Subscripts

Symbol	Description
<i>i</i>	Inner
<i>o</i>	Outer
<i>g</i>	Glass
<i>go</i>	Glass cover outer
<i>gi</i>	Glass cover inner
<i>di</i>	Dryout inception
<i>de</i>	Dryout completion
<i>bz</i>	Boltzmann probability function

## NOMENCLATURE

---

<b>Symbol</b>	<b>Description</b>
<i>L</i>	Liquid
<i>G</i>	Vapour
<i>H</i>	Homogeneous
<i>amb</i>	Ambient
<i>r</i>	Receiver
<i>rad</i>	Radiation
<i>conv</i>	Convection
<i>mom</i>	Momentum
<i>fric</i>	Friction
<i>in</i>	Inlet
<i>out</i>	Outlet
1	State 1: pump inlet
2	State 2: receiver inlet
3	State 3: turbine inlet
4	State 4: turbine outlet
<i>tp</i>	Two-phase
<i>dry</i>	Dry perimeter
<i>wet</i>	Wet perimeter
<i>cb</i>	Convection boiling
<i>nb</i>	Nucleate boiling
<i>s</i>	Isentropic
<i>opt</i>	Optimal

---

## LIST OF FIGURES

2.1 Schematic of a flat-plate collector. . . . .	6
2.2 A parabolic trough and parabolic dish collector illustrating the difference between line focusing and point focusing. . . . .	6
2.3 Illustration of a zero and non-zero incident angle. . . . .	7
2.4 Schematic depicting the acceptance angle and rim angle. . . . .	8
2.5 Temperature-Entropy (T-s) diagram of a Carnot cycle, where $T_H$ is the high temperature and $T_L$ is the low temperature. . . . .	9
2.6 Temperature-Entropy (T-s) diagram of a simple Rankine cycle. . . . .	10
2.7 Once-through system. . . . .	11
2.8 Recirculation system. . . . .	12
2.9 Longitudinal schematic view of a section of a receiver tube. . . . .	12
2.10 Schematic depicting the rim angle, rim radius and the aperture. . . . .	13
2.11 Partial cross-section of a receiver tube exposed to ambient. . . . .	14
2.12 Receiver tube and glass cover showing the respective surfaces. . . . .	17
2.13 Partial cross-section of an evacuated absorber tube. . . . .	18
2.14 Flow regimes for two-phase boiling in a horizontal tube. . . . .	19
2.15 Example of a flow pattern map for water at $250.35\text{ }^\circ\text{C}$ , $G = 305\text{ kg/m}^2\text{s}$ , $q = 101.8\text{ kW/m}^2$ and $D_i = 0.025\text{ m}$ . . . . .	22

LIST OF FIGURES
 

---

2.16	Heat transfer across a finite temperature difference. . . . .	27
2.17	Exergy flow diagram of the receiver. . . . .	29
2.18	Diagram showing the heat flow to the working fluid and ambient. . . . .	31
3.1	Iterative process for the solving of a unit section for the liquid and vapour single-phase regions. . . . .	40
3.2	Process for obtaining the total entropy generation for an entire single-phase region. . . . .	41
3.3	Fluid and receiver temperature changes throughout liquid region for $D_i = 0.025\text{ m}$ , $\dot{m} = 0.2\text{ kg/s}$ , $T_{sat} = 250.4\text{ °C}$ and an operating pressure of $4\text{ MPa}$ . . . . .	42
3.4	Glass cover temperature changes throughout liquid region for $D_i = 0.025\text{ m}$ , $\dot{m} = 0.2\text{ kg/s}$ , $T_{sat} = 250.4\text{ °C}$ and an operating pressure of $4\text{ MPa}$ . . . . .	42
3.5	Heat losses throughout liquid region for $D_i = 0.025\text{ m}$ , $\dot{m} = 0.2\text{ kg/s}$ , $T_{sat} = 250.4\text{ °C}$ and an operating pressure of $4\text{ MPa}$ . . . . .	43
3.6	Heat into the working fluid for each liquid unit section where $D_i = 0.025\text{ m}$ , $\dot{m} = 0.2\text{ kg/s}$ , $T_{sat} = 250.4\text{ °C}$ and an operating pressure of $4\text{ MPa}$ . . . . .	43
3.7	Entropy generation due to finite temperature differences for each liquid unit section where $D_i = 0.025\text{ m}$ , $\dot{m} = 0.2\text{ kg/s}$ , $T_{sat} = 250.4\text{ °C}$ and an operating pressure of $4\text{ MPa}$ . . . . .	44
3.8	Entropy generation due to fluid friction for each liquid unit section where $D_i = 0.025\text{ m}$ , $\dot{m} = 0.2\text{ kg/s}$ , $T_{sat} = 250.4\text{ °C}$ and an operating pressure of $4\text{ MPa}$ . . . . .	44
3.9	Iterative process for the solving of a section for the two-phase regions. . . . .	46
3.10	Two-phase multiplier for the quality range where $D_i = 0.025\text{ m}$ , $\dot{m} = 0.2\text{ kg/s}$ , $T_{sat} = 250.4\text{ °C}$ and an operating pressure of $4\text{ MPa}$ . . . . .	47
3.11	Change in heat transfer coefficient for the quality range where $D_i = 0.025\text{ m}$ , $\dot{m} = 0.2\text{ kg/s}$ , $T_{sat} = 250.4\text{ °C}$ and an operating pressure of $4\text{ MPa}$ . . . . .	48
3.12	Change in receiver temperatures for the quality range where $D_i = 0.025\text{ m}$ , $\dot{m} = 0.2\text{ kg/s}$ , $T_{sat} = 250.4\text{ °C}$ and an operating pressure of $4\text{ MPa}$ . . . . .	48
3.13	Change in glass temperatures for the quality range where $D_i = 0.025\text{ m}$ , $\dot{m} = 0.2\text{ kg/s}$ , $T_{sat} = 250.4\text{ °C}$ and an operating pressure of $4\text{ MPa}$ . . . . .	49
3.14	Heat into the working fluid for the quality range where $D_i = 0.025\text{ m}$ , $\dot{m} = 0.2\text{ kg/s}$ , $T_{sat} = 250.4\text{ °C}$ and an operating pressure of $4\text{ MPa}$ . . . . .	49

LIST OF FIGURES
 

---

3.15	Entropy generation due to finite temperature differences for the quality range where $D_i = 0.025\text{ m}$ , $\dot{m} = 0.2\text{ kg/s}$ , $T_{sat} = 250.4\text{ °C}$ and an operating pressure of $4\text{ MPa}$ . . . . .	50
3.16	Entropy generation due to fluid friction differences for the quality range where $D_i = 0.025\text{ m}$ , $\dot{m} = 0.2\text{ kg/s}$ , $T_{sat} = 250.4\text{ °C}$ and an operating pressure of $4\text{ MPa}$ . . . . .	50
3.17	Fluid and receiver temperature changes throughout the superheated vapour region where $D_i = 0.025\text{ m}$ , $\dot{m} = 0.2\text{ kg/s}$ , $T_{sat} = 250.4\text{ °C}$ and an operating pressure of $4\text{ MPa}$ . . . . .	51
3.18	Glass cover temperature changes throughout the superheated vapour region where $D_i = 0.025\text{ m}$ , $\dot{m} = 0.2\text{ kg/s}$ , $T_{sat} = 250.4\text{ °C}$ and an operating pressure of $4\text{ MPa}$ . . . . .	52
3.19	Heat losses for each superheated vapour unit section where $D_i = 0.025\text{ m}$ , $\dot{m} = 0.2\text{ kg/s}$ , $T_{sat} = 250.4\text{ °C}$ and an operating pressure of $4\text{ MPa}$ . . . . .	52
3.20	Heat into the working fluid for each superheated vapour unit section where $D_i = 0.025\text{ m}$ , $\dot{m} = 0.2\text{ kg/s}$ , $T_{sat} = 250.4\text{ °C}$ and an operating pressure of $4\text{ MPa}$ . . . . .	53
3.21	Entropy generation due to finite temperature differences for each liquid unit section where $D_i = 0.025\text{ m}$ , $\dot{m} = 0.2\text{ kg/s}$ , $T_{sat} = 250.4\text{ °C}$ and an operating pressure of $4\text{ MPa}$ . . . . .	53
3.22	Entropy generation due to fluid friction for each superheated unit section where $D_i = 0.025\text{ m}$ , $\dot{m} = 0.2\text{ kg/s}$ , $T_{sat} = 250.4\text{ °C}$ and an operating pressure of $4\text{ MPa}$ . . . . .	54
4.1	Entropy generation due to finite temperature differences for low operating pressures $1\text{ MPa}$ to $5\text{ MPa}$ . (a) $\dot{m} = 0.15\text{ kg/s}$ , (b) $\dot{m} = 0.4\text{ kg/s}$ . . . . .	57
4.2	Heat transfer coefficient for $1\text{ MPa}$ , $\dot{m} = 0.15\text{ kg/s}$ and $D_i = 15\text{ mm}$ . . . . .	58
4.3	Entropy generation due to finite temperature differences for high operating pressures of $6\text{ MPa}$ to $9\text{ MPa}$ . (a) $\dot{m} = 0.15\text{ kg/s}$ , (b) $\dot{m} = 0.4\text{ kg/s}$ . . . . .	58
4.4	Entropy generation due to fluid friction for low operating pressures $1\text{ MPa}$ to $5\text{ MPa}$ . (a) $\dot{m} = 0.15\text{ kg/s}$ , (b) $\dot{m} = 0.4\text{ kg/s}$ . . . . .	59
4.5	Entropy generation due to fluid friction for high operating pressures of $6\text{ MPa}$ to $9\text{ MPa}$ . (a) $\dot{m} = 0.15\text{ kg/s}$ , (b) $\dot{m} = 0.4\text{ kg/s}$ . . . . .	60
4.6	Total entropy generation for low operating pressures of $1\text{ MPa}$ to $5\text{ MPa}$ . (a) $\dot{m} = 0.15\text{ kg/s}$ , (b) $\dot{m} = 0.4\text{ kg/s}$ . . . . .	61
4.7	Bejan number for low operating pressures of $1\text{ MPa}$ to $5\text{ MPa}$ . (a) $\dot{m} = 0.15\text{ kg/s}$ , (b) $\dot{m} = 0.4\text{ kg/s}$ . . . . .	62

---

LIST OF FIGURES
 

---

4.8	Total entropy generation for high operating pressures of 6 MPa to 9 MPa. (a) $\dot{m} = 0.15 \text{ kg/s}$ , (b) $\dot{m} = 0.4 \text{ kg/s}$ . . . . .	62
4.9	Bejan number for high operating pressures of 6 MPa to 9 MPa. (a) $\dot{m} = 0.15 \text{ kg/s}$ , (b) $\dot{m} = 0.4 \text{ kg/s}$ . . . . .	63
4.10	Effects of changing the effective sky temperature on the total entropy generation for different operating pressures, where $D_i = 25 \text{ mm}$ and $\dot{m} = 0.2 \text{ kg/s}$ . . . . .	64
4.11	Effects of changing the wind velocity on the total entropy generation for different operating pressures, where $D_i = 25 \text{ mm}$ and $\dot{m} = 0.2 \text{ kg/s}$ . . . . .	65
4.12	Effects of changing the maximum focused heat per unit section on the total entropy generation for different operating pressures, where $D_i = 25 \text{ mm}$ and $\dot{m} = 0.2 \text{ kg/s}$ . . . . .	66
4.13	Effects of changing the glass cover clearance on the total entropy generation for different operating pressures, where $D_i = 25 \text{ mm}$ and $\dot{m} = 0.2 \text{ kg/s}$ . . . . .	67
5.1	Similarity between a minimisation and maximisation problem. . . . .	69
5.2	Contour plot for the base case parameters of 4 MPa and $\dot{m} = 0.2 \text{ kg/s}$ . . . . .	71
5.3	One dimensional plot of function values along the constraint $g(X) = 45$ . . . . .	71
5.4	Contour plot for the high operating pressure and high mass flow rate (10 MPa and $\dot{m} = 0.4 \text{ kg/s}$ ). . . . .	72
5.5	Example of a Pareto diagram for two objective functions. . . . .	75
5.6	Maximum work output (kW) vs total entropy generation (W/K) for a fixed diameter of $D_i = 20 \text{ mm}$ and various mass flow rates. . . . .	76
5.7	Maximum work output (kW) vs total entropy generation (W/K) for highest mass flow ( $\dot{m} = 0.4 \text{ kg/s}$ ). . . . .	77
A.1	Two-phase flow validation for R22, $\dot{G} = 150 \text{ kg/m}^2\text{s}$ , $D_i = 13.84 \text{ mm}$ , $T_{sat} = 5^\circ\text{C}$ and $q = 3.6 \text{ kW/m}^2$ . . . . .	83
A.2	Sensitivity analysis results at a low mass flow rate of $\dot{m} = 0.15 \text{ kg/s}$ ( $D_i = 25 \text{ mm}$ ). . . . .	84
A.3	Sensitivity analysis results at a high mass flow rate of $\dot{m} = 0.4 \text{ kg/s}$ ( $D_i = 25 \text{ mm}$ ). . . . .	84
A.4	Sensitivity analysis results at a large diameter of $D_i = 50 \text{ mm}$ and moderate mass flow of $\dot{m} = 0.2 \text{ kg/s}$ . . . . .	85

---

## LIST OF FIGURES

---

A.5	Sensitivity analysis results at a small diameter of $D_i = 15mm$ and moderate mass flow of $\dot{m} = 0.2 kg/s$ . . . . .	85
A.6	Maximum work output ( $kW$ ) vs total entropy generation ( $W/K$ ) for a large diameter of $D_i = 50 mm$ and various mass flow rates. . . . .	86

---

# LIST OF TABLES

2.1	Tracking method comparisons shown in percentage of full tracking (adapted from Kalogirou (2009)) . . . . .	8
3.1	Operating pressures, saturation temperature, enthalpy of evaporation and turbine inlet temperature. . . . .	36
3.2	Summary of fixed values as used by the base case analysis. . . . .	37
3.3	Concentration ratios for various diameters for $\dot{Q}_{sun} = 2\,000\,W$ and $S_r = 720\,W/m^2$ . . . . .	39
4.1	Region-length comparison for a high and low mass flow rate and inner-tube diameter of $D_i = 15\,mm$ . . . . .	56
4.2	Region-length comparison for low mass flow rate of $\dot{m} = 0.15\,kg/s$ and inner-tube diameter of $D_i = 50\,mm$ . . . . .	56
4.3	Average Friedel two-phase flow multiplier and corresponding pressure drop for two-phase flow region where $\dot{m} = 0.2\,kg/s$ and an inner-tube diameter of $D_i = 25\,mm$ . . . . .	61
4.4	Concentration ratios for the larger amount of focussed heat of $Q_{sun} = 3000\,W$ and $S_r = 720W/m^2$ . . . . .	66
5.1	Global optimum for design vector $X = (D_i, \dot{m}, P)$ ( $T_0 = 2\,000$ , $n = 200$ , $c = 0.6$ , $k = 2$ ). . . . .	74
5.2	Optimum pressure for various mass flow rates, where $D_i = 20\,mm$ . . . . .	74

---

---

# CHAPTER 1

---

## INTRODUCTION

### 1.1 BACKGROUND

Population increases and mounting energy demands have become a growing concern of late since it is recognised that fossil fuels are exhaustible. Due to this and global warming concerns, the focus on electricity generation by means of fossil fuels has shifted to alternative greener energy resources such as hydro-, solar and wind power. Currently, most of South Africa's electrical power is derived from coal sources. However it is generally accepted that South Africa has sufficient solar insolation to produce feasible solar power plants. Some well-known solar power plants are located in the Mojave desert in California, USA, for example, SEGS (Solar electric generating systems) plants. Recently, other countries such as Spain and Australia have also invested in solar power plants. Research is often conducted on small-scale prototype plants to investigate the feasibility of the specific region where the plant is built as well as the plant configuration (for example, parabolic trough technology or central receiver technology). Major advantages of solar technologies are sustainability and minimal adverse effects to the environment. However, the challenges, of solar power generation include the efficient harnessing of the solar energy as well as the storage of the energy (Fluri, 2009; Mills, 2004; Pegels, 2010; Price *et al.*, 2002; Viebahn *et al.*, 2011).

In the past, various thermodynamic power cycles have been considered for power generation, such as the Brayton, Stirling and Rankine cycles. The advantage of a Rankine steam cycle for solar application is that the peak working fluid temperature (turbine inlet temperature) is considerably lower than temperatures associated with the Brayton cycle. Greater temperatures translate into higher thermal stresses on the components as well as more losses to ambient. Conversely, efficiencies associated with Rankine cycles are lower than those associated with Brayton and Stirling engines due to a smaller temperature differential. Furthermore, various working fluids can be considered for the power cycle. If two cycles are involved, it is also necessary to incorporate more than one working fluid. Molten salts have been considered for high-temperature

## CHAPTER 1. INTRODUCTION

---

solar applications (such as central receiver technology) due to their high thermal capacity and boiling point.

To date the most mature, and widely used, solar technology for electricity generation is the parabolic trough with single-axis tracking. Parabolic trough technology often utilises either thermal oil or water as the working fluid. If thermal oil is used, two cycles have to be incorporated: a primary thermal cycle (circulating the oil) as well as a secondary power cycle (circulating steam). On the other hand, if water is used as the working fluid, only one cycle is incorporated and the solar-heated steam powers a turbine to produce work output. This is often referred to as direct steam generation (DSG). Such a scenario is advantageous since the system will not be subject to additional energy losses which are associated with the heat exchanger linking the two cycles. Furthermore, using water as a working fluid is beneficial in that it does not require additional expenses associated with the costly oil. However, optimal locations for solar power plants are usually in areas where the water is scarce (i.e. desert areas). This can become problematic since water is used for numerous processes in such a solar thermal power plant (cooling, replenishing of working fluid etc.) (Forsberg *et al.*, 2007; Mills, 2004; Viebahn *et al.*, 2011).

This study focuses on the second law analysis and optimisation of a parabolic trough solar receiver that is assumed to operate in a simple thermal Rankine power cycle with water as the working fluid. Water is heated and evaporated by means of focused solar radiation in the receiver tube. The steam is used to power a turbine, which will produce mechanical work. Major exergy (available energy) losses take place at both the condenser component as well as the receiver. The exergy destruction in the condenser, is however, of a low quality and is not the main focus of this text thus the emphasis will be on the parabolic trough collector (Singh *et al.*, 2000; Koroneos *et al.*, 2003).

### 1.2 PROBLEM STATEMENT

A simple Rankine cycle, used for DSG, consists of four basic components, namely a pump, a heater (or a boiler in a conventional Rankine cycle), a steam turbine and a condenser. For this solar power cycle, a parabolic trough receiver tube will function as the boiler. Solar incidence is focused on the absorber tube by means of a reflective trough. The water inside the tube is heated to steam and the steam, in turn, is passed through a turbine to produce mechanical work which can, in turn, generate electrical energy. As mentioned in the previous section, high quality exergy losses are associated with the collector. This is due to temperature differences between the tube and the ambient as well as, to a lesser extent, the pressure losses due to fluid friction. The condenser is also associated with a large amount of exergy losses since heat is simply rejected to the surroundings. The rejected heat, however, is not able to power the turbine further (and hence not able to generate electricity), and consequently, it is considered a low quality exergy. This study focuses on the minimisation of losses and generated entropy in the parabolic trough assembly due to the fact that this exergy is of a high quality.

The minimisation of the entropy generation due to finite temperature differences is often in

## CHAPTER 1. INTRODUCTION

---

conflict with the minimisation of the entropy generation due to fluid friction. For example, increasing the diameter of the receiver tube decreases the fluid friction but increases the heat losses to the surroundings. Therefore, it is not always apparent what the best design choices are for such a parabolic receiver tube.

### 1.3 PURPOSE OF STUDY

The purpose of the study is to thermodynamically analyse and optimise the parabolic trough receiver tube that operates in a Rankine steam power cycle. Different operating pressures (and hence saturation temperatures) are investigated to see the effect this has on the different entropy generation components (i.e. entropy generation due to fluid friction and due to temperature differences). Furthermore, the effect of the diameter and mass flow rates is also investigated. From the results and optimisation, general recommendations can be made for good design practices and general considerations pertaining to the trough receiver tube.

### 1.4 OUTLINE OF DISSERTATION

#### 1.4.1 CHAPTER 2: Literature Review

This chapter gives a short background to focusing solar technology. Parabolic trough technology and focusing are discussed in more depth and schematics of various configurations are shown. Equations pertaining to parabolic focusing are stated and discussed. Furthermore the governing equations pertaining to the thermal analysis of the receiver tube are stated and discussed. These equations are the basis of the first law analysis. Since direct steam generation takes place in the receiver tube, two-phase flow theory is also discussed. The final sections in this chapter deal with the second law analysis and lists equations that can be used to determine the entropy generation (or exergy destruction) in the receiver tube.

#### 1.4.2 CHAPTER 3: Numerical Work

This chapter gives an overview of the numerical model. The single-phase regions of the receiver tube are solved slightly differently from the two-phase regions. Schematics of the iterative procedures are given and discussed. Base case parameters are chosen and validation graphs are plotted for the specific case to ensure the correct working of the numerical model and to give insight to the section by section changes perceived into such a receiver tube.

#### 1.4.3 CHAPTER 4: Results

This chapter shows the results as obtained by the numerical code for the various cases. Firstly, an overview of the various region lengths for different cases are given. Graphs depict the changes in

## CHAPTER 1. INTRODUCTION

---

entropy generation for various conditions. The results are plotted for various operating pressures as well as different diameters. Furthermore, high and low mass flow rate cases are investigated.

### 1.4.4 CHAPTER 5: Optimisation

This chapter deals with the optimisation of the receiver tube. Initially, the concentration ratio and diameter are taken as the design variables, and contour plots of these variables are shown. As a second initiative, a simulated annealing optimisation algorithm is implemented. Finally, a Pareto-type plot is generated to evaluate the ranges where minimum entropy generation is achieved for maximum work output.

### 1.4.5 CHAPTER 6: Conclusion

This chapter provides the conclusions that were made during the course of this study. Recommendations for future work as well as recommendations for improvements of the numerical model are also provided.

---

---

# CHAPTER 2

---

## LITERATURE REVIEW

### 2.1 INTRODUCTION

This chapter focuses on the available literature and governing equations pertaining to the receiver tube. Brief overviews of solar collectors and sun tracking are given as background to the study. Furthermore, since the receiver tube will be operating in a power cycle, an overview of the Carnot and Rankine cycles is also given. The final sections deal exclusively with a parabolic trough collector. The receiver thermal analysis section deals with the first law governing equations of the receiver. Firstly, a simplified case of a bare receiver tube is considered and the internal and external heat transfer coefficients are discussed. The following subsection deals with a glass-covered receiver tube. This will be the case under investigation since bare tubes will not be feasible for the temperature range under investigation. The two-phase flow governing equations are discussed separately from the single-phase equations, and correlations and procedures to obtain the pressure drop and heat transfer coefficients are discussed. The final section discusses the second law equations pertaining to the receiver. Losses will be due to the temperature difference between the hot receiver tube and the surroundings as well as fluid friction.

### 2.2 SOLAR COLLECTORS

Solar collectors can be divided into two broad categories, focusing collectors and non-focusing (or stationary) collectors (Barlev *et al.*, 2011). Non-focussing-type collectors are collectors such as flat-plate collectors (shown in Figure 2.1) for indoor water heating. An advantage of flat-plate collectors is that heating is not only achieved by direct solar radiation, but also by diffuse radiation. The downside is that temperatures reached by non-focusing collectors are far lower than those of the focusing type and consequently, this technology cannot be used in electricity generation in a thermal power plant. Focusing collectors, on the other hand, require mainly

CHAPTER 2. LITERATURE REVIEW

direct solar radiation to perform properly and hence additional measurements must be made for proper sun-tracking.

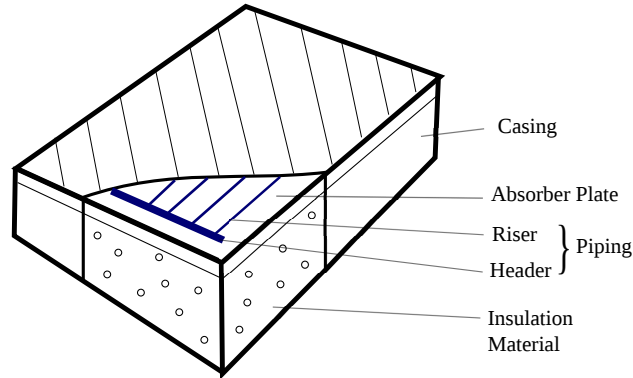


Figure 2.1: Schematic of a flat-plate collector.

Line focusing can be achieved by parabolic trough collectors while point focusing can be achieved by parabolic dish collectors (see Figure 2.2). In general, point collectors such as the parabolic dish and solar power towers can reach higher concentration ratios than a collector that only implements line focusing. The drawback is that accurate two-axis sun-tracking must be implemented, which may prove to be more expensive and harder to achieve. Sun-tracking is discussed in the following section.

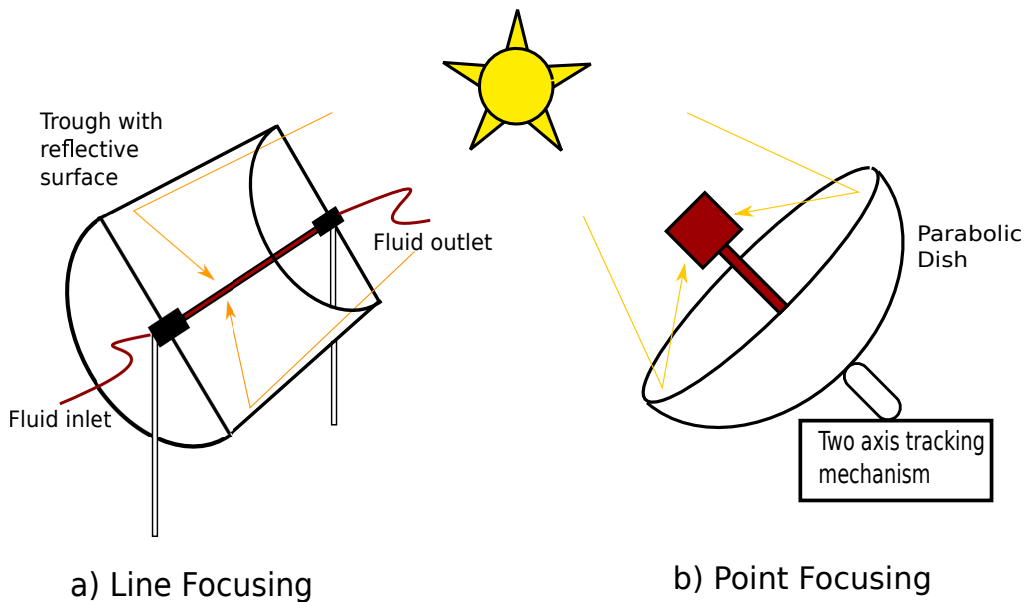


Figure 2.2: A parabolic trough and parabolic dish collector illustrating the difference between line focusing and point focusing.

## 2.3 SUN-TRACKING

Focusing collectors require tracking mechanisms to track the sun. Full tracking involves two-axis tracking, and consequently, tracking mechanisms can become quite expensive, especially if large reflector surfaces are to track the sun. A parabolic dish collector, for example, requires two-axis tracking. A parabolic trough collector, however, only requires one-axis tracking. This ensures a more economical initial investment. Full tracking yields larger concentration ratios, provided that the tracking mechanism is accurate, and the angle of incidence remains zero ( $\theta = 0$ ) as shown in Figure 2.3.

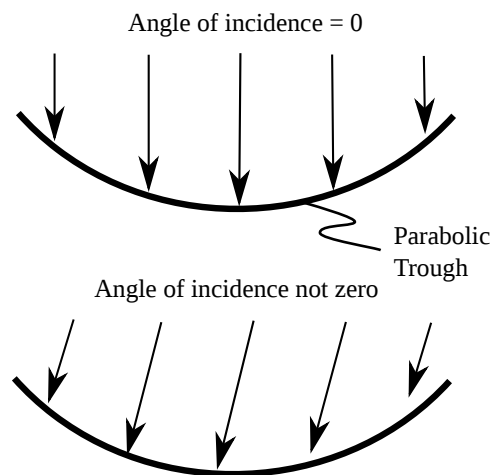


Figure 2.3: Illustration of a zero and non-zero incident angle.

For one-axis tracking, the amount of solar flux delivered to the receiver depends on the mode of tracking. The various modes of single-axis tracking are the following:

- east-west (E-W) polar tracking
- north-south (N-S) horizontal tracking
- east-west (E-W) horizontal tracking

The earth's rotational axis (called the polar axis) is not completely perpendicular to its elliptical axis but rather inclined at an angle of  $23.5^\circ$ . For E-W polar tracking, the collector axis is placed in the polar north-south direction and the angle of incidence will vary from a minimum of  $\theta = 0$  at equinoxes to  $\theta = 23.5^\circ$  at solstices. For E-W horizontal tracking, the collector axis is placed in a north-south direction and the calculation of the incidence angle becomes more involved. For N-S tracking, the collector axis is orientated in an east-west direction. Each of these three methods performs differently. Table 2.1 shows the percentage of solar energy that can be collected with respect to full tracking. Evidently, full tracking yields the maximum amount of collected solar energy at 100%. Similar performances can be achieved by E-W polar tracking. However, a disadvantage is that shadowing effects are encountered when multiple rows of collector surfaces

CHAPTER 2. LITERATURE REVIEW

---

are implemented. Also note that the amount of solar energy collected remains at a maximum for the equinoxes due to the fact that the angle of incidence can be zero for well-designed troughs at equinoxes. Furthermore, reasonable fluxes can be achieved during the summer solstice and equinoxes by N-S horizontal tracking. However, performance during winter solstice is quite poor. E-W horizontal tracking is associated with the worst performance and is therefore not frequently recommended. However, shadowing effects are considered minimal (Kalogirou, 2004, 2009).

Table 2.1: Tracking method comparisons shown in percentage of full tracking (adapted from Kalogirou (2009))

Tracking Method	Equinoxes	Summer Solstice	Winter Solstice
Full Tracking	100	100	100
E-W Polar	100	91.7	91.7
N-S horizontal	89.1	97.7	60.9
E-W horizontal	73.8	74	86.2

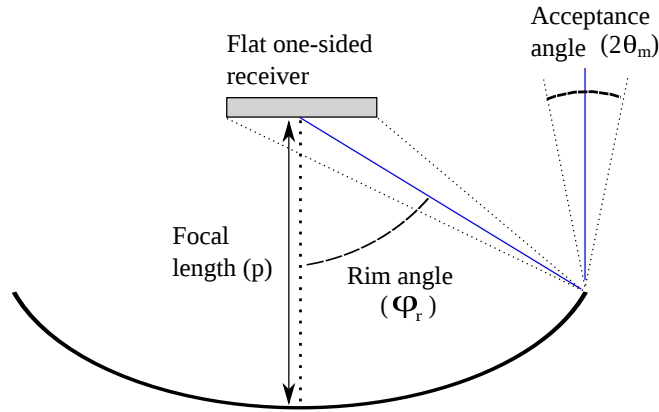


Figure 2.4: Schematic depicting the acceptance angle and rim angle.

Figure 2.4 depicts the acceptance angle ( $2\theta_m$ ) as well as the rim angle ( $\phi_r$ ). Note, firstly, that the receiver is depicted as a disc since the sun's reflected image will be a disc. Secondly, the receiver is exaggerated to illustrate the acceptance angle. The concentration ratio of a focusing collector can be defined as the ratio of the aperture to the absorber area. The theoretical maximum concentration that can be achieved by a 2D and 3D collector is given respectively by Lunde (1980) as:

$$C_{R,ideal,2dim} = \frac{1}{\sin(\theta_m)} \tag{2.1}$$

$$C_{R,ideal,3dim} = \frac{1}{\sin^2(\theta_m)} \tag{2.2}$$

The acceptance half-angle ( $\theta_m$ ) describes the angular range at which radiation can be collected by the collector while stationary. For extremely well-designed tracking mechanisms, the acceptance

## CHAPTER 2. LITERATURE REVIEW

---

angle (and hence the acceptance half-angle) is very small and hence the incoming radiation very focused yielding a high concentration ratio. The theoretical minimum of the acceptance angle is governed by the distance between the sun and the earth as well as the sun's diameter. For a theoretical minimum of  $\theta_m = 0.53^\circ$ , the theoretical maximum for the concentration ratio can be calculated as:

$$C_{R,ideal,2dim} = \frac{1}{\sin(\theta_m)} \approx 216 \quad (2.3)$$

$$C_{R,ideal,3dim} = \frac{1}{\sin^2(\theta_m)} \approx 47000 \quad (2.4)$$

These concentration ratios are extremely high and actual concentration ratios achieved by constructed collectors will be considerably lower due to various losses such as geometrical losses, optical losses, tracking losses and shading losses (Rabl *et al.*, 1982).

## 2.4 ENERGY CYCLES

Thermodynamic cycles such as the Brayton cycle, the Stirling cycle and the Rankine cycle can be used to convert thermal energy to mechanical energy. The focus of this study is on a simple Rankine cycle that uses water as a working fluid. To determine whether the Rankine cycle is efficient and reaches its full potential, it is often compared with the Carnot cycle. Figure 2.5 shows the T-s diagram of an ideal Carnot cycle. The Carnot cycle is a theoretically ideal cycle, which has been shown to have the maximum work output for a given thermal input.

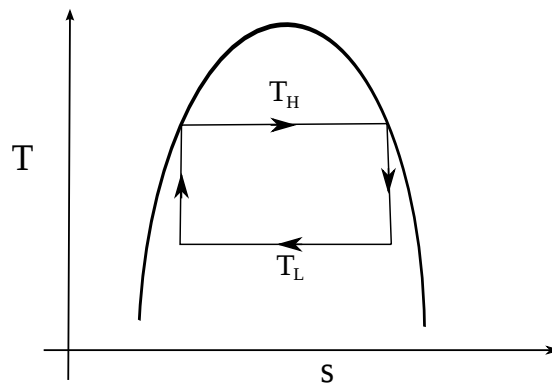


Figure 2.5: Temperature-Entropy (T-s) diagram of a Carnot cycle, where  $T_H$  is the high temperature and  $T_L$  is the low temperature.

Carnot efficiency is given by Equation 2.5:

$$\eta_{carnot} = 1 - \frac{T_L}{T_H} \quad (2.5)$$

CHAPTER 2. LITERATURE REVIEW

---

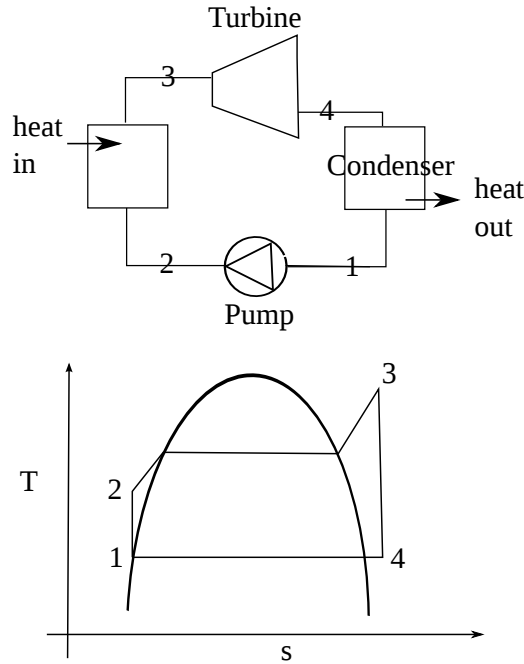


Figure 2.6: Temperature-Entropy (T-s) diagram of a simple Rankine cycle.

Figure 2.6 shows the ideal T-s diagram of a simple Rankine cycle as well as the associated components. A working fluid (such as water in the case of this text) is pumped to a higher operating pressure. Subsequently, the working fluid is heated, in a constant pressure process. As the fluid is heated it undergoes a phase change and eventually reaches superheated status. The heat needed to reach saturation temperature is given by:

$$Q = \dot{m}(h_{ent,3} - h_{ent,2}) \quad (2.6)$$

The latent heat needed for evaporation is given by:

$$\dot{Q} = \dot{m}h_{fg} \quad (2.7)$$

The superheated fluid is then driven through a turbine to produce work after which the fluid reaches close to ambient pressure. The fluid is now condensed and the cycle repeats. The turbine work and pump work are given respectively by:

$$W_{turbine} = \dot{m}(h_{ent,3} - h_{ent,4}) \quad (2.8)$$

$$W_{pump} = \dot{m}(h_{ent,2} - h_{ent,1}) \quad (2.9)$$

## 2.5 PARABOLIC TROUGH COLLECTORS

Some advantages of parabolic trough collectors are that they are low cost and well tested. Water can be used as a reasonably inexpensive working fluid. The downside to this is that a solar thermal power plant does require water in various processes such as cleaning of reflective surfaces, possible cooling during the condensing stage and replenishing of water in the cycle. Due to this, the location of the power plant must have water readily available. Parabolic trough technology is seen as medium temperature application and the heated working fluid (such as water) can reach temperatures as high as 400 °C. The availability of water offers an advantage when compared with thermal oil as a working fluid. The volatility of water, on the other hand, is seen as a disadvantage since this contributes to additional maintenance and precautionary costs. When deciding on a working fluid, the maintenance cost must be set against the initial investment to find a suitable selection.

The use of water also reduces operating costs as well as environmental risks. A challenge associated with direct steam generation (DSG) systems is the non-uniform temperature distribution in the receiver tube due to stratification of the liquid and vapour in the two-phase region. This non-uniform temperature distribution can cause bending of the receiver tube. A variation on the once-through system (shown in Figure 2.7) has been considered to counter this problem, namely the recirculation system. The once-through system simply heats the working fluid to the superheated stage. As the quality of the fluid increases and more fluid is evaporated, dryout can occur at the upper perimeter of the receiver tube.

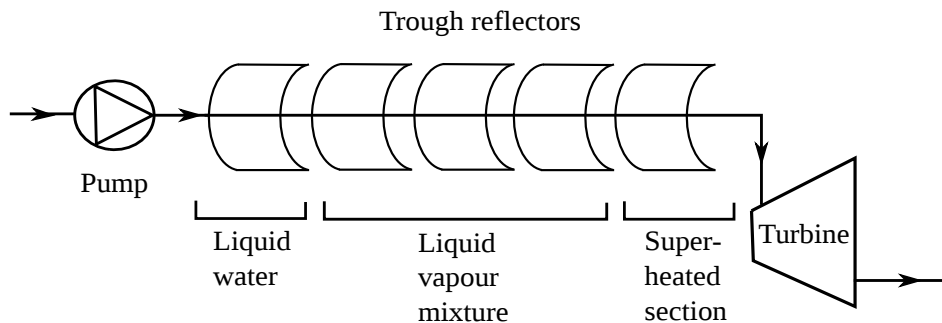


Figure 2.7: Once-through system.

The recirculation system (shown in Figure 2.8) attempts to counter the stratification and dryout effect by separating the liquid and vapour before a high quality is reached. More fluid is fed into the loop than can be evaporated in one cycle and the excess water is recirculated through the cycle, while the vapour can be heated further to a superheated state and passed through the turbine. The recirculation system is easier to control when compared with the once-through system but it does, however, involve an extra parasitic load due to the pump. Mixer components will also generate additional entropy (Barlev *et al.*, 2011; Eck *et al.*, 2003).

In Figure 2.9, a schematic of a longitudinal section of the receiver tube and cover is shown. The receiver tube is covered by a glass cover. The receiver is treated with a coating that allows for maximum solar radiation absorption. Similarly, the glass cover is treated with a coating that

CHAPTER 2. LITERATURE REVIEW

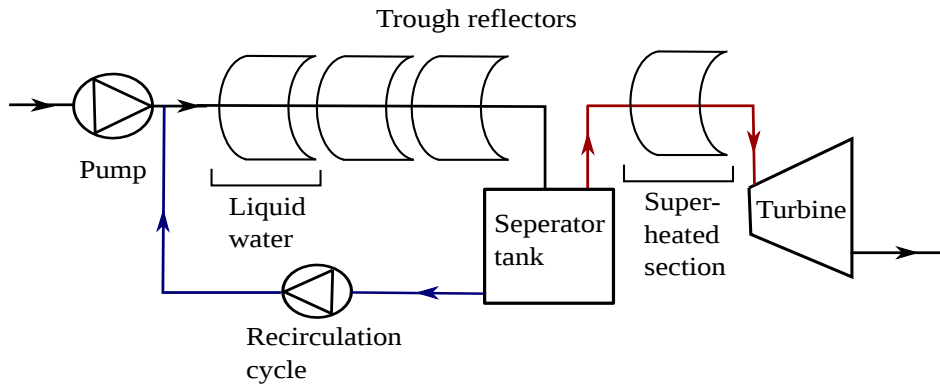


Figure 2.8: Recirculation system.

maximises transmittance of the radiation. The vacuum must be maintained at pressures smaller than 0.013 Pa. Furthermore, Figure 2.9 depicts the bellows as well as the exhaust nozzle. The bellows allow for expansion to counter breakages of the glass envelope. The getter (not shown) is located inside the vacuum. The getters act as chemical sponges to react with certain molecules that permeate through the receiver and glass walls due to the high temperature of operation and low-pressure conditions inside the space. The release of these molecules can increase the pressure in the evacuated space and as a consequence, reduce the efficiency of the receiver tube. Getters have a finite lifetime and can lose their effectiveness after years of operation. Each of these segments can be up to 4 m long (Price *et al.*, 2002; Roesle *et al.*, 2011).

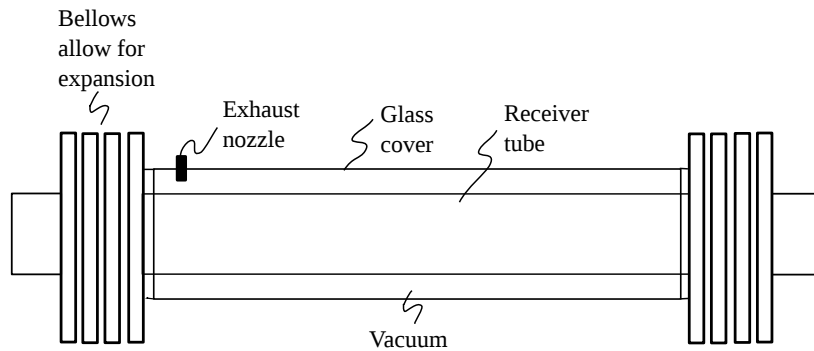


Figure 2.9: Longitudinal schematic view of a section of a receiver tube.

The equation describing the parabolic form is given by:

$$y = \frac{1}{4p}x^2 \tag{2.10}$$

Note that the focal length is denoted by ( $p$ ). Figure 2.10 depicts the rim radius and aperture length of a parabolic trough. When the focal length ( $p$ ) as well as the rim angle ( $\phi_r$ ) is known, the aperture can be calculated by Equation 2.11.

CHAPTER 2. LITERATURE REVIEW

---

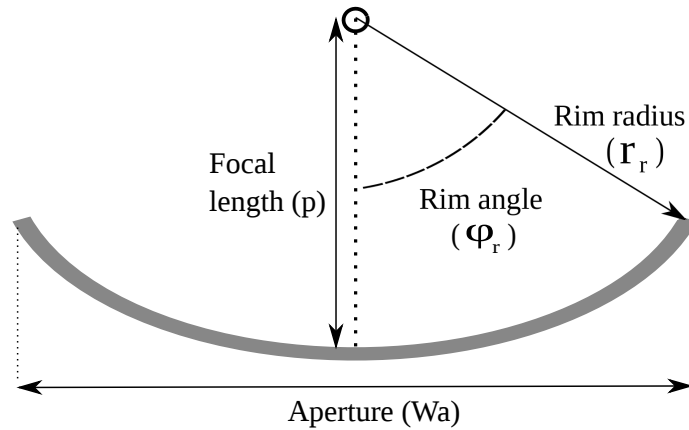


Figure 2.10: Schematic depicting the rim angle, rim radius and the aperture.

$$W_a = \frac{4 p \sin(\phi_r)}{1 + \cos(\phi_r)} \quad (2.11)$$

The length of the parabolic surface is given by Equation 2.12:

$$S_p = \frac{4p}{2} \left\{ \frac{\tan(\phi_r/2)}{\cos(\phi_r/2)} + \ln \left( \frac{1}{\cos(\phi_r/2)} + \tan(\phi_r/2) \right) \right\} \quad (2.12)$$

It can be shown that for a rim angle of  $90^\circ$  Equation 2.12 reduces to the following:

$$S_p = \frac{W_p}{2} \left\{ \sqrt{2} + \ln[\sqrt{2} + 1] \right\} \quad (2.13)$$

For a tubular receiver, the concentration ratio is given by:

$$C_R = \frac{W_a}{\pi D_o} \quad (2.14)$$

A variation on this equation has the following form:

$$C_R = \frac{W_a - D_o}{\pi D_o} \quad (2.15)$$

This equation is used by Garcia-Valladares and Velazquez (2009) and it recognises that the aperture area is slightly truncated due to the fact that the absorber tube blocks some of the incoming rays. This blockage, however, has a negligible effect on the concentration ratio since the total length of the aperture is much more than that of the tube diameter.

## 2.6 RECEIVER THERMAL ANALYSIS

In the following sections, the equations relating to the thermal analysis of the receiver tube are discussed in detail. As a simplistic introduction, the equations pertaining to a bare tube analysis are discussed prior to the section dealing with a covered receiver tube.

### 2.6.1 Bare Tube

More often than not the receiver tube is evacuated. If the receiver tube is not covered by a vacuum, the losses to ambient will be significant. The simplistic case of a bare tube is considered in this section. The modes of heat transfer and certain equations encountered in the analysis for a bare tube are the same as for the glass-covered tube. The losses from the receiver to ambient are mainly due to convection and radiation. This scenario is similar for a covered tube except that the glass cover temperature must be obtained first. Similarly, the internal heat transfer coefficients for both cases are calculated using the same equations.

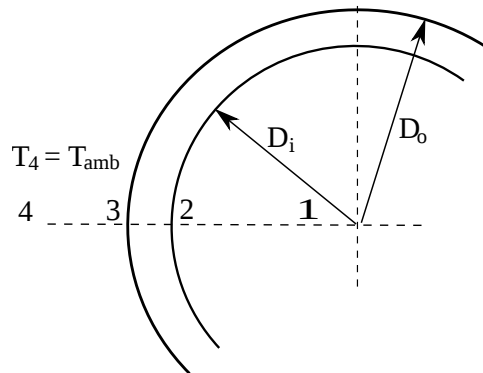


Figure 2.11: Partial cross-section of a receiver tube exposed to ambient.

Figure 2.11 depicts a partial cross-section of a bare absorber tube exposed to ambient conditions. The numbers (numbered 1 to 4) refer to the fluid, the inner wall, outer wall and ambient conditions, respectively. Calculating the heat losses to ambient for the bare tube requires the knowledge of the convection heat transfer coefficients. The internal forced convection coefficient for the water inside the absorber tube (single-phase flow) can be estimated by the Gnielinski correlation given by Equation 2.16 (Cengle, 2006; Gnielinsky, 1976):

$$Nu = \frac{(f/8)(Re - 1000)Pr}{1 + 12.7(f/8)^{0.5}(Pr^{2/3} - 1)} \quad (2.16)$$

in range:

$$0.5 < Pr < 2000$$

CHAPTER 2. LITERATURE REVIEW
 

---

$$3 \times 10^3 < Re < 5 \times 10^6$$

This correlation is considered quite accurate for these Reynolds number ranges and can be used for a constant heat flux as well as a constant surface temperature scenario. For the analysis of the receiver tube, it is recognised that a constant heat flux approach is a more realistic model. Note, however, that Equation 2.16 is only valid for single-phase regions. The friction coefficient ( $f$ ) can be obtained by Equation 2.17, which is known as the first Petukhov equation and can be used for smooth tubes (Cengle, 2006):

$$f = (0.79 \times (\ln(Re)) - 1.64)^{-2} \quad (2.17)$$

Which is valid for a Reynolds number range of:

$$10^4 < Re < 10^6$$

A variation of this equation, used by Forristall (2003) as well as Garcia-Valladares and Velazquez (2009), is given by:

$$f = (1.82 \times (\log(Re)) - 1.64)^{-2} \quad (2.18)$$

Furthermore, a variation of Equation 2.16 as used by Forristall (2003):

$$Nu = \frac{(f/8)(Re - 1000)Pr}{1 + 12.7(f/8)^{0.5}(Pr^{2/3} - 1)} \left( \frac{Pr_1}{Pr_2} \right) \quad (2.19)$$

with:

$$0.5 < Pr < 2000$$

$$2300 < Re < 5 \times 10^6$$

This equation also accounts for transitional flow and adjusts if there are large variations between the fluid temperature and the tube-wall temperature, hence the additional Prandtl number ( $Pr_2$ ), which should be evaluated at the wall temperature. If the Nusselt number is known, the heat transfer coefficient can be calculated by:

$$h = (k/D_i) \times Nu \quad (2.20)$$

CHAPTER 2. LITERATURE REVIEW
 

---

The conduction through the tube wall can be described by:

$$q_{cond,2-3} = \frac{2\pi k(T_2 - T_3)}{\ln(D_o/D_i)} \quad (2.21)$$

On the outer surface of the tube (3 in Figure 2.11), radiation and convection losses contribute significantly to the losses. External convection heat transfer either occurs due to natural convection or forced due to wind over the surface. If wind is present, the Nusselt number can be estimated by the Churchill and Bernstein correlation (Cengel, 2006; Churchill and Bernstein, 1977):

$$Nu = 0.3 + \frac{0.62Re^{1/2}Pr^{1/3}}{[1 + (0.4/Pr)^{2/3}]^{1/4}} \left[ 1 + \left( \frac{Re}{28200} \right)^{5/8} \right]^{4/5} \quad (2.22)$$

This equation is valid for  $RePr > 0.2$  and the properties of the fluid (air in this case) are evaluated at the film temperature:

$$T_f = \frac{1}{2}(T_\infty - T_s) \quad (2.23)$$

For natural convection, a correlation developed by Churchill and Chu can be used to obtain the Nusselt number (Cengel, 2006; Churchill and Chu, 1975; Forristall, 2003):

$$Nu = \left[ 0.60 + \frac{0.387Ra^{1/6}}{[1 + (0.559/Pr)^{9/16}]^{8/27}} \right]^2 \quad (2.24)$$

The Rayleigh number and thermal expansion coefficient are given by:

$$Ra = \frac{g\beta(T_3 - T_4)D_o^3}{\alpha\nu} = \frac{g\beta(T_3 - T_4)D_o^3}{\nu^2} Pr \quad (2.25)$$

$$\beta = \frac{1}{T_f} \quad (2.26)$$

As mentioned previously, if the Nusselt number is known, the external heat transfer coefficient can be determined and, in turn, the heat loss to ambient due to convection can be estimated:

$$Q_{conv,3-4} = h\pi D_o L(T_3 - T_{amb}) \quad (2.27)$$

Also of importance is the radiation from the absorber tube to the sky:

---

CHAPTER 2. LITERATURE REVIEW

---

$$Q_{rad,3-4} = \sigma D_o \pi L \varepsilon (T_3^4 - T_{sky}^4) \tag{2.28}$$

Note that  $T_{sky}$  is the effective sky temperature. This temperature can be estimated at 8 °C below the ambient temperature (Forristall, 2003). Alternatively, an equation can be used to estimate the effective sky temperature (Garcia-Valladares and Velazquez, 2009):

$$T_{sky} = 0.0552 (T_{amb})^{1.5} \tag{2.29}$$

From these equations, it is evident that the temperature of the exposed surface (the receiver tube  $T_3$  in this section) plays an important role in estimating the losses.

**2.6.2 Glass-covered Tube**

The view factor ( $F$ ) plays an important role in radiation heat transfer. It can be defined as the percentage of radiation leaving one surface and striking a second surface. For the absorber tube of the parabolic trough, it is assumed that the end effects are negligible since the pipe longitudinal length is much larger than the length of the diameter. Thus  $F_{12}$  is assumed to be equal to unity for the configuration shown in Figure 2.12.

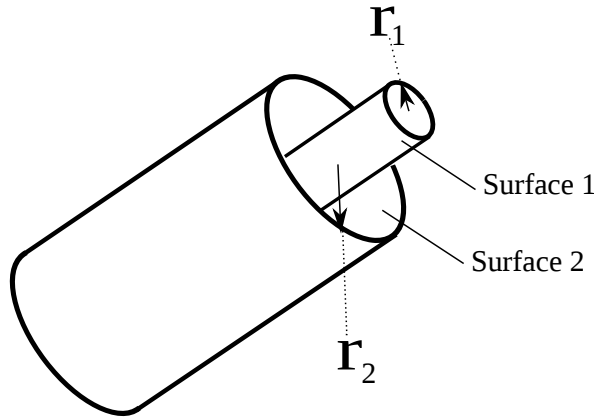


Figure 2.12: Receiver tube and glass cover showing the respective surfaces.

For two infinitely long cylinders, the heat transfer from surface 1 to surface 2 is given by (Cengle, 2006):

$$Q_{12} = \frac{A_1 \sigma (T_1^4 - T_2^4)}{\frac{1}{\varepsilon_1} + \frac{1-\varepsilon_2}{\varepsilon_2} \left(\frac{r_1}{r_2}\right)} \tag{2.30}$$

Also note that:

CHAPTER 2. LITERATURE REVIEW

$$\frac{A_1}{A_2} = \frac{r_1}{r_2} \quad (2.31)$$

and

$$F_{12} = 1 \quad (2.32)$$

Figure 2.13 depicts a partial cross-section of an evacuated tube covered by glass. From surface 3 to 4, radiation heat transfer has a significant effect on the losses. Free molecular convection or natural convection (if the vacuum is not properly maintained) also contributes to the heat transfer from the surfaces but this is assumed to be negligible for a perfectly vacuum-insulated absorber tube.

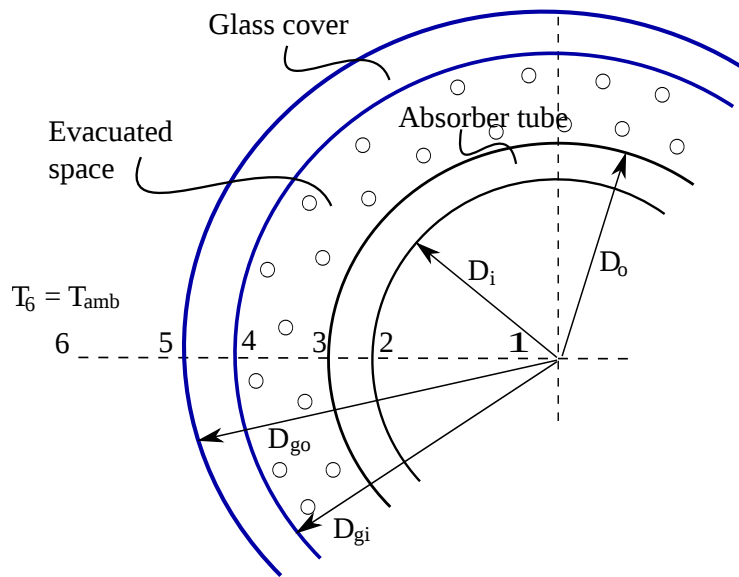


Figure 2.13: Partial cross-section of an evacuated absorber tube.

The radiation heat transfer from surface 3 to 4 is given by:

$$Q_{rad,3-4} = \frac{D_o \pi L \sigma (T_3^4 - T_4^4)}{\frac{1}{\epsilon_3} + \frac{1 - \epsilon_4}{\epsilon_4} \left( \frac{D_o}{D_{gi}} \right)} \quad (2.33)$$

Furthermore, the radiation heat transfer (from surface 5) to the atmosphere is given by:

$$Q_{rad,5-sky} = \sigma \epsilon D_{go} \pi L (T_5^4 - T_{sky}^4) \quad (2.34)$$

Similar to the previous section, the convection heat transfer coefficient is given by:

$$Q_{conv,5-6} = h_{conv,5-6} D_{go} \pi L (T_5 - T_6) \quad (2.35)$$

## CHAPTER 2. LITERATURE REVIEW

---

Recognising that the radiation from the receiver to the cover must equal the total heat lost, if it is assumed that no heat is absorbed by the cover, an energy balance over the cover can be performed:

$$Q_{rad,3-4} = Q_{conv,5-6} + Q_{rad,5-sky} \quad (2.36)$$

The conduction heat transfer through the glass cover is given by:

$$q_{cond,4-5} = \frac{2\pi k(T_4 - T_5)}{\ln(D_{go}/D_{gi})} \quad (2.37)$$

This temperature is important since the surface is exposed to ambient conditions and hence governs how much heat is lost to the atmosphere and ambient. Similar equations to the ones stated in this section are used by Forristall (2003), Garcia-Valladares and Velazquez (2009) and Odeh *et al.* (1998). Reddy *et al.* (2008) numerically investigated the effects of a heat transfer enhancement on receiver efficiency.

## 2.7 TWO-PHASE FLOW

### 2.7.1 Two-Phase Heat Transfer

The analysis for calculating the internal heat transfer coefficient, presented in the previous section, deals exclusively with the single-phase regions (liquid and superheated). However, in the two-phase region, the heat transfer coefficient is highly dependent on the type of flow encountered in the region. For example, at very low mass flow rates (or mass velocities), gravity is a significant factor and the flow mainly remains stratified with liquid wetting only the lower perimeter but not the upper. At higher mass velocities and moderate qualities, the flow might be annular and the whole perimeter will be wetted. However, at higher qualities, dryout tends to occur. During intermittent and wavy flow, waves of liquid may intermittently wash over the upper unwetted parts. During wavy flow, there is also concern for dryout in the upper regions of the tube circumference (Thome, 2004; Kattan *et al.*, 1998). Figure 2.14 depicts the different flow regimes as classified by Collier and Thome (1994):

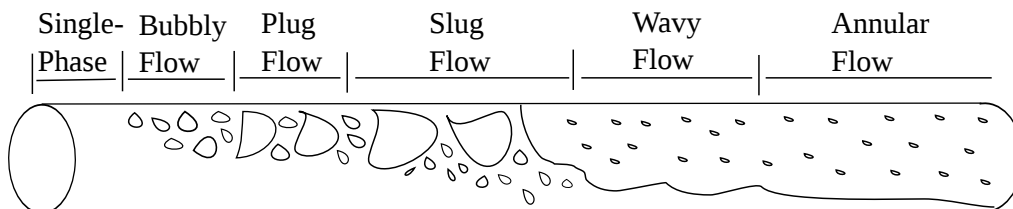


Figure 2.14: Flow regimes for two-phase boiling in a horizontal tube.

CHAPTER 2. LITERATURE REVIEW
 

---

In this section, the flow boiling pattern map of Wojtan *et al.* (2005a,b) are discussed. This heat transfer model and flow pattern map builds on the work done by Kattan *et al.* (1998). The method in predicting the heat transfer coefficient discussed by Kattan *et al.* (1998) recognises that the heat transfer coefficient is highly dependent on the two-phase flow regime. The work of Zurcher *et al.* (2002) builds on the work of Kattan *et al.* (1998) and their flow pattern procedures are used by Garcia-Valladares and Velazquez (2009).

The two-phase flow heat transfer coefficient can be determined by separating the wet and dry heat transfer coefficients:

$$h_{tp} = \frac{\theta_{dry} h_{vapour} + (2\pi - \theta_{dry}) h_{wet}}{2\pi} \quad (2.38)$$

The wet heat transfer coefficient is determined by combining the nucleate boiling coefficient as well as the convective boiling coefficient:

$$h_{wet} = (h_{nb}^3 + h_{cb}^3)^{1/3} \quad (2.39)$$

The nucleate boiling coefficient and convective boiling coefficient are given respectively by:

$$h_{nb} = 55 P_r^{0.12} (-\log P_r)^{-0.55} M^{-0.5} q^{0.67} \quad (2.40)$$

$$h_{cb} = 0.0133 \left[ \frac{4G(1-x)\delta}{(1-\varepsilon_{void})\mu_L} \right]^{0.69} (Pr_L)^{0.4} \frac{k_L}{\delta} \quad (2.41)$$

Where  $\varepsilon_{void}$  is the void fraction (Rouhani and Axelsson, 1970):

$$\varepsilon_{void} = \frac{x}{\rho_G} \left( [1 + 0.12(1-x)] \left[ \frac{x}{\rho_G} + \frac{1-x}{\rho_L} \right] + \left( \frac{1.18}{G} \right) \left[ \frac{g\sigma_{surr}(\rho_L - \rho_G)}{\rho_L^2} \right]^{1/4} (1-x) \right)^{-1} \quad (2.42)$$

In two-phase flow analysis, the mass velocity is often used instead of mass flow rate. The mass velocity is given by Equation 2.43:

$$G = \frac{\dot{m}}{A_i} \quad (2.43)$$

The vapour heat transfer coefficient is given by:

CHAPTER 2. LITERATURE REVIEW
 

---

$$h_{vapour} = 0.023 \left[ \frac{GxD_i}{\varepsilon_{void}\mu_G} \right]^{0.8} (Pr_G)^{0.4} \frac{k_G}{D_i} \quad (2.44)$$

The internal area occupied by the liquid is given by:

$$A_L = A_i(1 - \varepsilon_{void}) \quad (2.45)$$

Kattan *et al.* (1998) used the following implicit equation to solve the stratified angle ( $\theta_{strat}$ ):

$$A_L = 0.5 \left( \frac{D_i}{2} \right)^2 [(2\pi - \theta_{strat}) - \sin(2\pi - \theta_{strat})] \quad (2.46)$$

To avoid the iteration involved in the solving of the implicit equation, Biberg (cited by Wojtan *et al.*, 2005a) proposed the following equation for  $\theta_{strat}$ :

$$\begin{aligned} \theta_{strat} = 2\pi - 2 \left( \pi(1 - \varepsilon_{void}) + \left( \frac{3\pi}{2} \right)^{1/3} \left[ 1 - 2(1 - \varepsilon_{void}) + (1 - \varepsilon_{void})^{1/3} - \varepsilon_{void}^{1/3} \right] \right. \\ \left. - \left( \frac{1}{200} \right) (1 - \varepsilon_{void})\varepsilon_{void}[1 - 2(1 - \varepsilon_{void})][1 + 4((1 - \varepsilon_{void})^2) + \varepsilon_{void}^2] \right) \end{aligned} \quad (2.47)$$

The stratified angle is used to obtain the dry angle. Figure 2.15 shows an arbitrary flow pattern map for water at a saturation temperature of  $250.35^\circ C$ . The figure shows the various two-phase flow zones:

- Intermittent (I)
- Annular (A)
- Slug (Slug)
- Slug and stratified wavy (Slug and SW)
- Stratified (S)
- Stratified-wavy (SW)
- Dryout (D)
- Misty (M)

CHAPTER 2. LITERATURE REVIEW

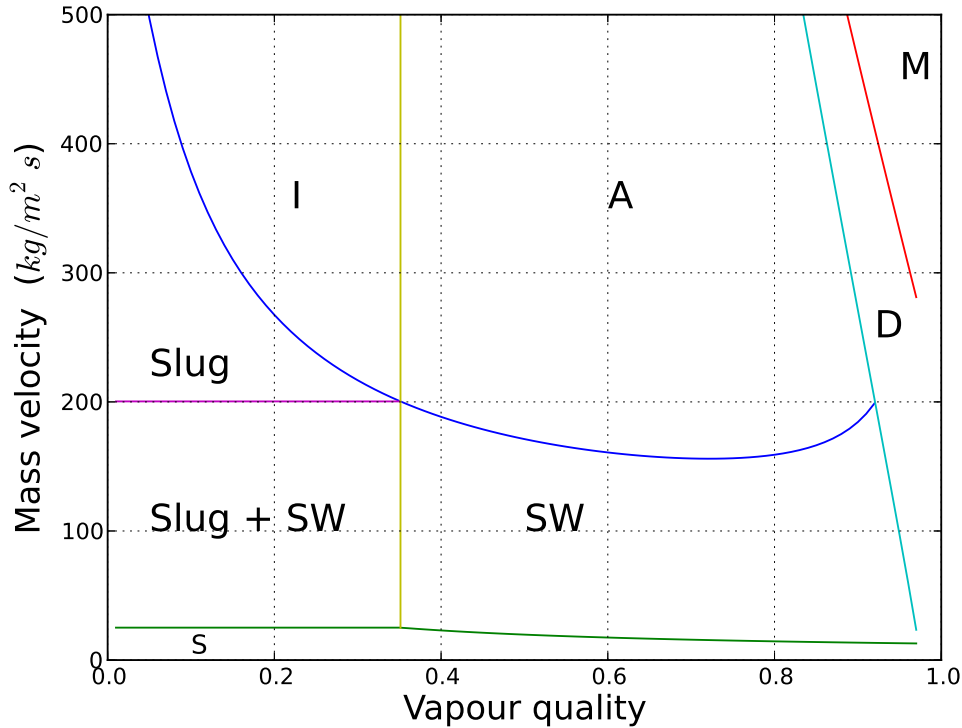


Figure 2.15: Example of a flow pattern map for water at  $250.35\text{ }^{\circ}\text{C}$ ,  $G = 305\text{ kg/m}^2\text{s}$ ,  $q = 101.8\text{ kW/m}^2$  and  $D_i = 0.025\text{ m}$ .

By determining in which zone the flow is located, the heat transfer coefficient can be solved.

Equation 2.49 ( $G_{strat}$ ) separates the stratified zone from the slug+SW zones as well as the SW zone (indicated in green in Figure 2.15). Note, however, that  $G_{strat}$  is taken as a horizontal line between the vapour quality of  $x = 0$  and  $x = x_{IA}$ . The quality  $x_{IA}$  (indicated in yellow) separates the intermittent and annular zone as well as the SW and slug+SW zone and can be calculated by the following:

$$x_{IA} = \left( \left[ 0.34^{1/0.875} \left( \frac{\rho_G}{\rho_L} \right)^{-1/1.75} \left( \frac{\mu_L}{\mu_G} \right)^{-1/7} \right] + 1 \right)^{-1} \quad (2.48)$$

For qualities larger than  $x = x_{IA}$  the stratified line is given by the following:

$$G_{strat} = \left[ \frac{226.3^2 A_{LD} A_{GD} \rho_G (\rho_L - \rho_G) \mu_L g}{x^2 (1-x) \pi^3} \right]^{1/3} \quad (2.49)$$

CHAPTER 2. LITERATURE REVIEW
 

---

Note that  $A_{LD}$  and  $A_{GD}$  are given in the nomenclature.  $G_{wavy}$  separates the intermittent and slug regime as well as the annular and stratified-wavy regime.  $G_{wavy}$  is given by Equation 2.50:

$$G_{wavy} = \left[ \frac{16A_{GD}^3 g D_i \rho_L \rho_G}{x^2 \pi^2 (1 - (2h_{LD} - 1)^2)^{0.5}} \left( \frac{\pi^2}{25h_{LD}^2} \left( \frac{We_L}{Fr_L} \right)^{-1} + 1 \right) \right]^{0.5} + 50 \quad (2.50)$$

Where  $h_{LD}$  is given by:

$$h_{LD} = 0.5 \left( 1 - \cos \left( \frac{2\pi - \theta_{strat}}{2} \right) \right) \quad (2.51)$$

As mentioned previously, the stratified angle ( $\theta_{strat}$ ) is used to determine the dry angle ( $\theta_{dry}$ ). The calculation of the dry angle will depend on the two-phase flow regime. For slug and intermittent flow, the dry angle is taken as zero ( $\theta_{dry} = 0$ ). When the flow is located in the SW zone, Equation 2.52 (an interpolation equation) is used to determine  $\theta_{dry}$ :

$$\theta_{dry} = \left[ \frac{G_{wavy} - G}{G_{wavy} - G_{strat}} \right]^{0.61} \theta_{strat} \quad (2.52)$$

Furthermore, for the slug+SW zone, the dry angle ( $\theta_{dry}$ ) is calculated by Equation 2.53

$$\theta_{dry} = \frac{x}{x_{IA}} \left[ \frac{G_{wavy} - G}{G_{wavy} - G_{strat}} \right]^{0.61} \theta_{strat} \quad (2.53)$$

Dryout tends to occur at higher qualities when the flow transitions from the SW or annular zone to the dryout zone. During dryout, a rapid fall in heat transfer coefficient can be observed. Dryout starts at the top of the tube perimeter and progresses to the bottom. Wojtan *et al.* (2005a) give two equations to predict the quality at which dryout starts ( $x_{di}$ ) and ends ( $x_{de}$ ):

$$x_{di} = 0.58e^{[0.52 - 0.235We_G^{0.17} Fr_G^{0.37} (\rho_G/\rho_L)^{0.25} (q/q_{crit})^{0.7}]} \quad (2.54)$$

$$x_{de} = 0.61e^{[0.57 - 0.0058We_G^{0.38} Fr_G^{0.15} (\rho_G/\rho_L)^{-0.09} (q/q_{crit})^{0.27}]} \quad (2.55)$$

Where  $q_{crit}$ :

$$q_{crit} = 0.131\rho_G^{0.5} h_{fg} [g(\rho_L - \rho_G)\sigma_{surr}]^{0.25} \quad (2.56)$$

CHAPTER 2. LITERATURE REVIEW
 

---

The vapour Froude number must be determined by the equation used by Mori et al. (cited by Wojtan *et al.*, 2005a):

$$Fr_G = \frac{G^2}{\rho_G g D_i (\rho_L - \rho_G)} \quad (2.57)$$

The dryout line can be determined by Equation 2.58:

$$G_{dryout} = \left[ \frac{1}{0.235} \left[ \ln \left( \frac{0.58}{x} \right) + 0.52 \right] \left( \frac{D}{\rho_G \sigma_{sur}} \right)^{-0.17} \right. \\ \left. \left( \frac{1}{g D_i \rho_G (\rho_L - \rho_G)} \right)^{-0.37} \left( \frac{\rho_G}{\rho_L} \right)^{-0.25} \left( \frac{q}{q_{crit}} \right)^{-0.7} \right]^{0.926} \quad (2.58)$$

The heat transfer coefficient in the dryout zone is determined by linear interpolation:

$$h_{dryout} = h_{tp}(x_{di}) - \left( \frac{x - x_{di}}{x_{de} - x_{di}} \right) (h_{tp}(x_{di}) - h_{mist}(x_{de})) \quad (2.59)$$

The misty flow line can be determined by:

$$G_{misty} = \left[ \frac{1}{0.0058} \left[ \ln \left( \frac{0.61}{x} \right) + 0.57 \right] \left( \frac{D}{\rho_G \sigma_{sur}} \right)^{-0.38} \right. \\ \left. \left( \frac{1}{g D_i \rho_G (\rho_L - \rho_G)} \right)^{-0.15} \left( \frac{\rho_G}{\rho_L} \right)^{0.09} \left( \frac{q}{q_{crit}} \right)^{-0.27} \right]^{0.943} \quad (2.60)$$

The heat transfer coefficient in the misty zone can be determined by:

$$h_{misty} = 0.0177 Re_H^{0.79} Pr_G^{1.06} Y^{-1.83} \frac{k_G}{D_i} \quad (2.61)$$

Where  $Y$  is given by:

$$Y = 1 - 0.1 \left[ \left( \frac{\rho_L}{\rho_G} - 1 \right) (1 - x) \right]^{0.4} \quad (2.62)$$

And  $Re_H$  is given by:

$$Re_H = \frac{G D_i}{\mu_G} \left( x + \frac{\rho_G}{\rho_L} (1 - x) \right) \quad (2.63)$$

---

 CHAPTER 2. LITERATURE REVIEW
 

---

### 2.7.2 Two-Phase Pressure Drop

The total pressure drop in the receiver tube is dependent on momentum losses, pressure head losses as well as friction losses:

$$\Delta P_{total} = \Delta P_{fric} + \Delta P_{mom} + \Delta P_{static} \quad (2.64)$$

If the height and momentum changes are not accounted for, Equation 2.64 will reduce to:

$$\Delta P_{total} = \Delta P_{fric} \quad (2.65)$$

Equation 2.65 is valid for both the single-phase region as well as the two-phase region. The Friedel correlation is a convenient correlation to calculate the two-phase flow pressure drop since it utilizes a two-phase multiplier along with the pressure drop equation for the liquid flow (Thome, 2004):

$$\Delta P_{two-phase} = \Delta P_L \Phi^2 \quad (2.66)$$

where:

$$\Delta P_L = 4 f_L \left( \frac{L}{D_i} \right) \left( \frac{\dot{m}}{A_i} \right)^2 \frac{1}{2\rho_L} \quad (2.67)$$

Note that this correlation is valid for viscosity ratios of  $\frac{\mu_L}{\mu_G} < 1000$ . The liquid friction coefficient ( $f_L$ ) can be calculated as follows:

$$f_L = \frac{0.079}{Re^{0.25}} \quad (2.68)$$

The liquid Reynolds number ( $Re_L$ ) can be calculated from:

$$Re_L = \left( \frac{\dot{m}}{A} \right) \frac{D_i}{\mu_L} \quad (2.69)$$

Note that  $\mu_L$  is the liquid dynamic viscosity. The two-phase multiplier can be calculated from:

$$\Phi^2 = E_{friedel} + \frac{3.24 \times F_{friedel} \times H_{friedel}}{Fr_{H,friedel}^{0.045} \times We_{L,friedel}^{0.035}} \quad (2.70)$$

CHAPTER 2. LITERATURE REVIEW
 

---

where the dimensionless factors  $Fr_{H,riedel}$ ,  $E_{riedel}$ ,  $F_{riedel}$ ,  $H_{riedel}$  and  $We_{L,riedel}$  are given by:

$$Fr_{H,riedel} = \left(\frac{\dot{m}}{A}\right)^2 \frac{1}{g \times D_i \times \rho_H^2} \quad (2.71)$$

$$E_{riedel} = (1 - x)^2 + x^2 \left(\frac{\rho_L f_G}{\rho_G f_L}\right) \quad (2.72)$$

$$F_{riedel} = x^{0.78} (1 - x)^{0.224} \quad (2.73)$$

$$H_{riedel} = \left(\frac{\rho_L}{\rho_G}\right)^{0.91} \left(\frac{\mu_G}{\mu_L}\right)^{0.19} \left(1 - \frac{\mu_G}{\mu_L}\right)^{0.7} \quad (2.74)$$

$$We_{L,riedel} = \left(\frac{\dot{m}}{A}\right)^2 \frac{D_i}{\sigma_{surr} \times \rho_H} \quad (2.75)$$

Note that  $\sigma_{surr}$  refers to the surface tension. Furthermore, note that the homogeneous density ( $\rho_H$ ) can be calculated as follows:

$$\rho_H = \left(\frac{x}{\rho_G} + \frac{1 - x}{\rho_L}\right)^{-1} \quad (2.76)$$

The homogeneous density equation assumes that the liquid and the vapour are travelling at the same velocities. An alternative way to calculate the two-phase density is, firstly, by obtaining the void fraction. The void fraction describes the fraction of the circumferential area that is occupied by vapour.

$$\rho_{tp} = \rho_L(1 - \varepsilon_{void}) + \rho_G \varepsilon_{void} \quad (2.77)$$

Various methods for calculating the void fraction exist. These methods are not discussed in this text. Calculation of the density by means of Equation 2.76 yields similar results to the density obtained by Equation 2.77. For this dissertation, the two-phase density will be obtained by using Equation 2.76 (Thome, 2004).

## 2.8 SECOND LAW ANALYSIS

Entropy generation in the receiver is the reason for exergy destruction. Minimising the entropy generation in the receiver, in turn, maximises the thermal energy delivered to the turbine. In other words, minimising the entropy generation has the effect of maximising the exergy and finally the power output of the plant. Entropy generation takes place, firstly, due to finite temperature differences between the receiver temperature and the surroundings. Heat is constantly lost to ambient. Secondly, fluid friction on the receiver tube wall cause, pressure losses, which are also a source of entropy generation (Bejan, 1995).

### 2.8.1 Finite Temperature Differences

In this section, a simplified scenario is investigated to illustrate the concept of entropy generation by finite temperature differences.

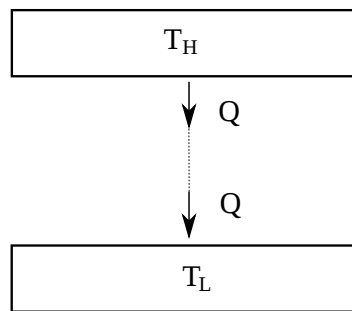


Figure 2.16: Heat transfer across a finite temperature difference.

Applying the second law of thermodynamics to the temperature gap shown in Figure 2.16 will yield an expression for the entropy generation:

$$S_{gen,dT} = \frac{Q}{T_L} - \frac{Q}{T_H} \quad (2.78)$$

The available work lost due to this phenomenon is proportional to the entropy generated:

$$W_{lost} = Q \left( 1 - \frac{T_L}{T_H} \right) = T_L S_{gen} \quad (2.79)$$

### 2.8.2 Fluid Friction

Considering a simple adiabatic pipe with a mass flow ( $\dot{m}$ ), inlet conditions ( $h_{in}, P_{in}, s_{in}$ ) and outlet conditions ( $h_{out}, P_{out}, s_{out}$ ), it can be shown that the entropy generation rate for incompressible flow is given by Bejan (1995, 1982):

CHAPTER 2. LITERATURE REVIEW
 

---

$$S_{gen,dP} = \dot{m}C_p \ln \left( \frac{T_{out}}{T_{in}} \right) \approx \dot{m} \frac{\Delta P}{\rho T_{in}} \quad (2.80)$$

Also note that from first law application, the following is valid:

$$h_{ent,in} = h_{ent,out} \quad (2.81)$$

$$S_{gen} = \dot{m}(s_{out} - s_{in}) \quad (2.82)$$

The pressure difference:

$$\Delta P = P_{in} - P_{out} \quad (2.83)$$

The pressure drop (for the single-phase regions) can also be calculated by:

$$\Delta P = f \left( \frac{L}{D_i} \right) \frac{\rho V^2}{2} \quad (2.84)$$

Similar results can be obtained by manipulating the equation for entropy generation in turbulent flow in a pipe with constant wall temperature. The total entropy generation is given by Sahin (2000):

$$S_{gen} = \dot{m}(s_{out} - s_{in}) - \frac{\delta Q}{T} = \dot{m}ds - \frac{\delta Q}{T} \quad (2.85)$$

But for incompressible flow, the following holds:

$$ds = \frac{C_p \delta T}{T} - \frac{dP}{\rho T} \quad (2.86)$$

Substituting Equation 2.86 into Equation 2.85, we can obtain:

$$S_{gen} = \dot{m} \left( \frac{C_p \delta T}{T} - \frac{dP}{\rho T} \right) - \frac{\delta Q}{T} \quad (2.87)$$

The  $\frac{\delta Q}{T}$  term as well as the  $\frac{C_p \delta T}{T}$  term is associated with the entropy generation due to heat differences, whereas the  $\frac{dP}{\rho T}$  term is associated with the entropy generation due to the fluid

## CHAPTER 2. LITERATURE REVIEW

---

friction and corresponds to Equation 2.80. For two-phase flow, the local entropy generation is given by Revellin *et al.* (2009):

$$S_{gen,dP} = \left( \frac{\dot{m}\bar{v}}{T_{in}} \right) \Delta P \quad (2.88)$$

$\bar{v}$  is the local specific volume. Equation 2.88 corresponds to the entropy generation for incompressible flow in an adiabatic pipe stated previously. Therefore, it can be seen that Equation 2.80 is valid for two-phase flow as well. However, it must be recognized that the specific volume (density) will change by a considerable amount throughout the two-phase section. Furthermore, since it is accepted that the vapour, for the range of investigation, cannot be considered an ideal gas and that the superheated section will remain in the turbulent region, Equation 2.88 is used for the final superheated section.

### 2.8.3 Exergy Destruction in Collectors

Figure 2.17 shows the exergy flow diagram of the receiver.

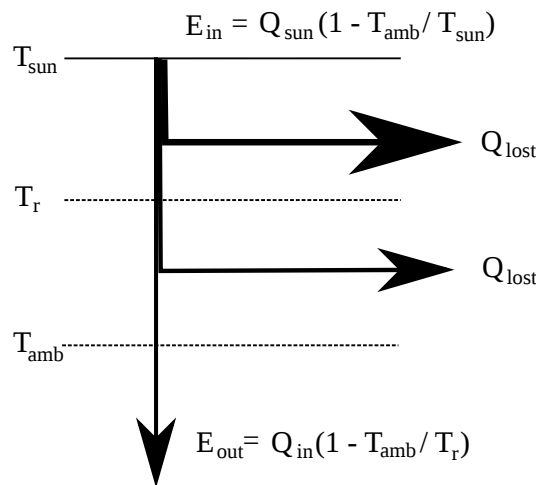


Figure 2.17: Exergy flow diagram of the receiver.

The high-temperature reservoir is the apparent sun temperature that can be calculated by Equation 2.89 (Kalogirou, 2009):

$$T_{sun} = \frac{3}{4} T_{sun,blackbody} \quad (2.89)$$

$T_{sun,blackbody}$  is the apparent blackbody temperature of the sun and estimated at 5 770 K. Thus the apparent sun temperature can be obtained as  $T_{sun} = 4\,330\text{ K}$ . The exergy into the receiver is given by:

CHAPTER 2. LITERATURE REVIEW
 

---

$$E_{in} = Q_{sun} \left( 1 - \frac{T_{amb}}{T_{sun}} \right) \quad (2.90)$$

Since  $T_{sun}$  is extremely large, the exergy into the system will approximately be equal to  $Q_{sun}$ , which is the heat supplied by the sun.  $Q_{sun}$  depends on the optical efficiency as well as the concentration ratio of the trough collector. Garcia-Valladares and Velazquez (2009) used the following equation to determine the solar radiation absorbed by the receiver:

$$S_r = I_b \rho_0 \tau \alpha_{abs} \gamma F_a \quad (2.91)$$

The properties  $\rho_0$ ,  $\tau$ ,  $\alpha_{abs}$ ,  $\gamma$  and  $F_a$  are the surface reflectivity, cover transmissivity, absorptance, shape factor and incident angle modifier, respectively. These properties contribute to the optical efficiency and Equation 2.91 can be rewritten as:

$$S_r = I_b \eta_{opt} \quad (2.92)$$

The solar beam radiation  $I_b$  can be estimated as the average beam radiation for a square area for a specific location. This value is often estimated as approximately  $1000 \text{ W/m}^2$ . Furthermore,  $Q_{sun}$  can be estimated as:

$$Q_{sun} = C_R S_r A_o \quad (2.93)$$

The exergy out of the control volume (the exergy that is transferred to the working fluid) can be calculated by:

$$E_{out} = Q_{fluid} \left( 1 - \frac{T_{amb}}{T_r} \right) \quad (2.94)$$

The destroyed exergy can be calculated by:

$$E_{des} = E_{in} - E_{out} \quad (2.95)$$

The destroyed exergy is also given by:

$$E_{des} = S_{gen} T_{amb} \quad (2.96)$$

CHAPTER 2. LITERATURE REVIEW

---

**2.8.4 Entropy Generation in Isothermal Collectors**

Figure 2.18 depicts a schematic of the heat flow from the apparent sun temperature ( $T_{sun}$ ) to the collector or more specifically, the receiver ( $T_r$ ) and ambient temperature ( $T_{amb}$ ). This schematic is similar to Figure 2.16, shown in the finite temperature difference section, but for this scenario it is recognised that the working fluid must absorb a part of the heat to power the turbine. As mentioned in a previous section, the heat loss to ambient is due to radiation as well as natural convection (if no wind is present) or forced convection (if wind is present).

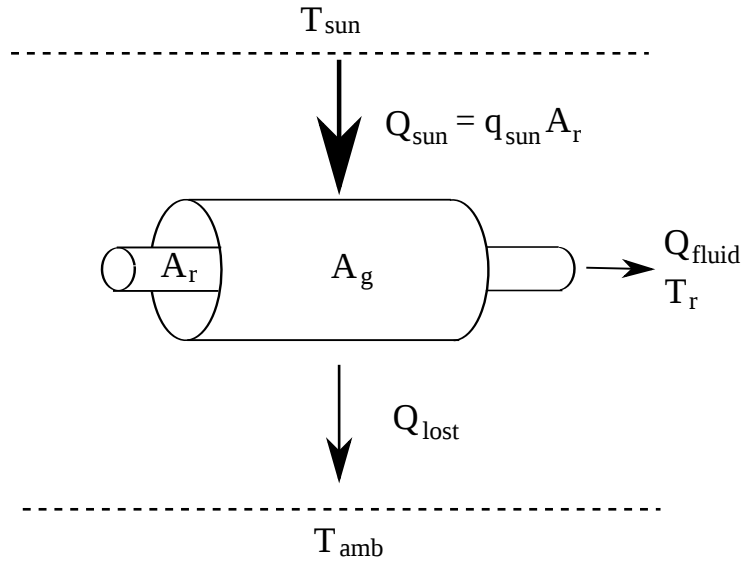


Figure 2.18: Diagram showing the heat flow to the working fluid and ambient.

By examining Figure 2.18, it can be seen that the following equations hold:

$$Q_{lost} = Q_{sun} - Q_{fluid} \tag{2.97}$$

$$Q_{amb} = U_r A_r (T_r - T_{amb}) \tag{2.98}$$

The overall heat transfer coefficient ( $U_r$ ) is based on the receiver area. Note that a long receiver pipe utilised in parabolic trough technology is not isothermal and that  $U_r$  as well as  $T_r$  will change along the pipe length. The entropy generation can be calculated as follows:

$$S_{gen} = \frac{Q_{lost}}{T_{amb}} + \frac{Q_{fluid}}{T_r} - \frac{Q_{sun}}{T_{sun}} \tag{2.99}$$

Equation 2.99 can be manipulated to show that it is equivalent to the expression for entropy generation in the previous section. Recognising that  $Q_{lost} = Q_{sun} - Q_{fluid}$ , Equation 2.99 can be rewritten as:

CHAPTER 2. LITERATURE REVIEW
 

---

$$S_{gen} = \frac{Q_{sun}}{T_{amb}} - \frac{Q_{fluid}}{T_{amb}} + \frac{Q_{fluid}}{T_r} - \frac{Q_{sun}}{T_{sun}} \quad (2.100)$$

Extracting  $\frac{1}{T_{amb}}$  and rearranging Equation 2.100:

$$S_{gen} = \frac{1}{T_{amb}} \left[ Q_{sun} \left( 1 - \frac{T_{amb}}{T_{sun}} \right) - Q_{fluid} \left( 1 - \frac{T_{amb}}{T_r} \right) \right] \quad (2.101)$$

Recognising the exergy terms, Equation 2.101 can be expressed as:

$$S_{gen} = \frac{1}{T_{amb}} [E_{in} - E_{out}] \quad (2.102)$$

This is similar to Equation 2.96.

### 2.8.5 Non-Isothermal Collectors

For non-isothermal collectors, the absorber tube and hence the receiver temperature vary length-wise if the water is in single phase. Recall that for isothermal collectors:

$$S_{gen} = \frac{Q_{lost}}{T_{amb}} + \frac{Q_{fluid}}{T_r} - \frac{Q_{sun}}{T_{sun}} \quad (2.103)$$

The solar insolation is fixed, in other words, the heat flux over the entire pipe length for the parabolic trough remains constant and hence the  $(Q_{sun}/T_{sun})$  term. Furthermore, for non-isothermal collectors, the total heat lost to ambient ( $Q_{lost}$ ) is a strong function of the receiver temperature and will progressively get larger as the absorber pipe and eventually, the glass cover gets hotter. If the absorber pipe is discretised into unit length sections, the analysis as presented in the previous section can be utilised since the temperature for a one-metre section will only vary slightly. In other words, the receiver is considered isothermal for unit sections.

### 2.8.6 Internal Flow Entropy Generation

Ratts and Raut (2004) investigated the entropy generation minimisation of fully developed internal flow with a constant heat flux. The investigation was extended for non-circular ducts. The entropy generation for a round duct per unit length is given by:

$$S_{gen} = \frac{q\pi D_i(T_w - T_b)}{T_b^2} + \frac{\dot{m}^3 f}{2\rho T D_i A_i^2} \quad (2.104)$$

## CHAPTER 2. LITERATURE REVIEW

---

A similar equation is given by Sahin (2000) for a smooth duct subject to a constant wall temperature:

$$dS_{gen} = \frac{\dot{m}C_p(T_w - T)dT}{TT_w} + \frac{dP}{\rho C_p T} \quad (2.105)$$

Sahin (2000) states that the viscosity changes due to temperature changes along the length of a pipe are the most significant when compared with other thermodynamic properties such as density. The investigation included an analysis of liquid water as well as glycerol.

Revellin *et al.* (2009) investigated the local entropy generation in two-phase flow. Two models were developed: a separated flow model and a mixture model. The local entropy generation for the separated flow model is given by:

$$dS_{gen} = \frac{q^2 \pi D_i}{hT_{sat}^2} + \frac{\dot{m}\bar{v}}{T_{sat}}(dP) \quad (2.106)$$

### 2.8.7 Bejan Number

The Bejan number is a convenient way to determine whether the entropy generation due to temperature differences ( $S_{gen,dT}$ ) or the entropy generation due to fluid friction ( $S_{gen,dP}$ ) contributes the most to the total entropy generation. The Bejan number is defined as:

$$Be = \frac{S_{gen,dT}}{S_{gen,dT} + S_{gen,dP}} = \frac{S_{gen,dT}}{S_{gen,total}} \quad (2.107)$$

Values close to unity indicate that the entropy generation is dominated by finite temperature differences, whereas values close to zero indicate that entropy generation due to fluid friction dominates.

## 2.9 CONCLUSION

In this chapter all the relevant equations pertaining to the first and second law analysis of a receiver tube were presented and discussed.

---

---

# CHAPTER 3

---

## NUMERICAL WORK

### 3.1 INTRODUCTION

Radiation from the sun is focused by means of a parabolic trough onto a receiver tube, which is placed at the focal point of the parabolic trough. Water as working fluid is pumped through the receiver tube and heated by the concentrated solar flux. The initial liquid water undergoes a change of state and eventually must reach a superheated state to power a turbine. The maximum heat flux on a receiver tube is governed by the concentration ratio as well as the optical efficiency of the trough collector. As the receiver temperature increases, the amount of heat delivered to the working fluid will decrease due to the losses to the surroundings. The amount of losses will progressively get larger as the receiver temperature increases. The process is seen as a constant pressure process even though the pressure drop through the receiver tube can be quite significant. Consequently, if a specific operating pressure is investigated, this pressure is assumed to be the average operating pressure, and furthermore, it is assumed that the pump power is adequate to overcome the fluid friction as well as maintain the operating pressure.

#### 3.1.1 Single-Phase Region

The equations as discussed in the previous chapter were used in the analysis of a receiver tube. These governing equations were programmed into Python (Python Software Foundation, 2011). Additional Numpy (Numpy Developers and Scipy Community, 2011) and SciPy (Scipy Community, 2011) packages were used in conjunction with Python. The internal as well as the external heat transfer coefficients are highly temperature dependent. As the air and water temperatures vary and increase along the receiver tube length, the air and water properties will also change. Due to the dependence of the governing equations on temperature, the receiver tube is divided into unit sections. Each unit section is solved by making use of a one-dimensional heat transfer energy balance. The temperature of the receiver tube will ultimately determine how

## CHAPTER 3. NUMERICAL WORK

---

much heat is reradiated to the cover and eventually lost from the cover to the surroundings. The heat lost to the surroundings will progressively get more as the receiver and cover temperatures rise. Furthermore, since the pressure drop is also slightly temperature dependent, the pressure drop is obtained for each unit section individually and eventually added to obtain the total pressure drop.

### 3.1.2 Two-Phase Region

The two-phase region is solved slightly differently from the single-phase regions. The region is not divided into unit sections but a section (usually longer than a unit metre) is solved for a particular change in quality. Firstly, for a specific quality, the internal heat transfer coefficient is calculated. This heat transfer coefficient then governs the receiver temperature, and ultimately, the losses as is done for the single-phase region.

## 3.2 ASSUMPTIONS

The assumptions are the following:

- The numerical model assumes that the sun-tracking is perfect and that the maximum heat flux on the receiver remains constant for various diameters.
- Heat transfer is one-dimensional and the heat flux on the receiver is completely uniform regardless of the fact that the receiver tube is primarily heated from the trough side or that flow stratification might cause uneven temperature distributions.
- Pressure drops through the pipe can be extremely large, however, it is assumed that the pumping power will be able to overcome the pressures. Therefore, the operating pressures as described in this chapter are the average pressure for that process.
- Losses through the bellows and structure are not taken into account.
- The static and momentum pressure drops are not taken into account since this would require knowledge of the pipe layout, which may vary considerably depending on the solar field design.

## 3.3 OPERATING PRESSURES

Various pressures were investigated as possible operating pressures. Operating temperatures higher than 400°C become beyond the range achievable with parabolic trough technology. Furthermore, operating pressures below 1 *MPa* become unfeasible since the friction losses will

---

 CHAPTER 3. NUMERICAL WORK
 

---

Table 3.1: Operating pressures, saturation temperature, enthalpy of evaporation and turbine inlet temperature.

Operating Pressure ( <i>MPa</i> )	Saturation Temperature ( $^{\circ}\text{C}$ )	Turbine Inlet Temperature ( $^{\circ}\text{C}$ )	$h_{fg}$ ( <i>kJ/kg</i> )
1	179.91	215.89	2015.3
2	212.42	254.9	1890.74
3	233.9	280.68	1795.73
4	250.4	300.48	1714.09
5	263.99	316.79	1640.12
6	275.64	330.77	1571.00
7	285.88	343.06	1505.1
8	295.06	354.07	1441.33
9	303.34	364.01	1379.06
10	310.85	373.02	1317.43

occasionally exceed the operating pressure. A summary of the operating pressures, corresponding saturation temperatures, turbine inlet temperatures and enthalpy of evaporation ( $h_{fg}$ ) is given in Table 3.1. Frequently, a turbine inlet temperature is determined by the specific turbine being utilized. However, for this numerical simulation, no turbine is specified, thus the turbine inlet temperature is assumed to be 20% higher than the saturation temperature.

The table shows that for the largest operating pressure that is investigated (10 *MPa*), the turbine inlet is around 373 $^{\circ}\text{C}$ . However, temperatures up to 400 $^{\circ}\text{C}$  can be investigated. Furthermore, what can also be seen from the table is that the enthalpy of evaporation decreases for higher operating pressures. In general, this is advantageous in lowering the entropy generation in the two-phase region.

### 3.4 FLUID PROPERTIES

As the temperature of the working fluid changes, properties such as density, viscosity and surface tension are also affected. As mentioned, this is why the receiver tube is divided into sections and each section solved separately. Furthermore, the average air temperature will also change as the glass cover is heated. CoolProp (Bell, 2013) is implemented to completely automate the process of obtaining fluid properties (air and water). CoolProp is an open-source alternative to the more widely used REFPROP. CoolProp estimates the properties of fluids to an extremely accurate degree by implementing equations of state, but the exact working of this is beyond the scope of this text.

### 3.5 INITIAL CONDITIONS

Table 3.2 summarises the values used in the base case (operating pressure of 4 MPa,  $D_i = 0.025$  m,  $\dot{m} = 0.2$  kg/s). The inner diameter as well as the clearance can be varied as geometric variables. Different mass flow rates can also be investigated. Furthermore, a sensitivity analysis can be conducted on parameters such as the effective sky temperature. The thermal conductivity of the receiver is given in Equation 3.1. The thermal conductivity of 304L and 316L steel varies with temperature (Forristall, 2003):

$$k_r = 0.013T_r + 15.2 \quad (3.1)$$

Table 3.2: Summary of fixed values as used by the base case analysis.

	Value	Unit
Inner diameter ( $D_i$ )	0.025	m
Thickness ( $t$ )	0.002	m
Outer diameter ( $D_o$ )	0.029	m
Clearance	0.01	m
Glass emissivity ( $\varepsilon_g$ )	0.87	-
Receiver emissivity ( $\varepsilon_r$ )	0.92	-
Glass thermal conductivity ( $k_{glass}$ )	1.05	W/(m K)
Ambient temperature ( $T_{amb}$ )	20	(°C)
Mass flow rate ( $\dot{m}$ )	0.2	kg/s
Effective sky temperature ( $T_{sky}$ )	12	(°C)
Wind velocity ( $V_{wind}$ )	2	m/s
Stefan-Boltzmann constant ( $\sigma$ )	$5.67 \times 10^{-8}$	W/m <sup>2</sup> K <sup>4</sup>
Solar energy per unit length ( $\dot{Q}_{sun}$ )	2 000	W
Solar irradiance ( $I_b$ )	1 000	W/m <sup>2</sup>
Optical efficiency ( $\eta_{opt}$ )	0.72	-

For a case where there is no preheating, the initial temperature of the water at the pump is taken as 20°C (ambient conditions). To determine an approximate initial receiver inlet temperature, a pump isentropic efficiency of 80% is assumed. The ideal pump work can be determined by the following:

$$W_{pump} = v(P_2 - P_1) = h_{ent,2s} - h_{ent,1} \quad (3.2)$$

The pump isentropic efficiency will govern the actual value of the enthalpy at the receiver inlet state. The efficiency is given by:

$$\eta_s = \frac{h_{ent,s2} - h_{ent,1}}{h_{ent,2} - h_{ent,1}} \quad (3.3)$$

---

 CHAPTER 3. NUMERICAL WORK
 

---

Rearranging and substituting Equation 3.2 into Equation 3.3 yield the following:

$$h_{ent,2} = h_{ent,1} + \frac{h_{ent,s2} - h_{ent,1}}{\eta_s} = h_{ent,1} + \frac{W_{pump}}{\eta_s} \quad (3.4)$$

If the enthalpy at this state is known, the temperature can easily be obtained by making use of CoolProp. The initial pressure is taken as 100 kPa or 1 Bar.

### 3.6 OPTICAL EFFICIENCY AND CONCENTRATION RATIO

$q_{sun}$  is the absorbed solar radiation concentrated on the receiver pipe per unit area. The optical efficiency is given by Equation 3.5.

$$\eta_{opt} = \frac{S_r}{I_b} \quad (3.5)$$

Where  $S_r$  is the reflected solar energy per unit area and given by Equation 3.6.

$$S_r = I_b \rho_0 \tau \alpha_{abs} \gamma F_a \quad (3.6)$$

An optical efficiency of 72% is assumed. In other words, the inefficiencies due to the absorptance ( $\alpha_{abs}$ ), cover transmittance ( $\tau$ ), surface reflectivity ( $\rho_0$ ), angle modifier ( $F_a$ ) as well as the shape factor ( $\gamma$ ) equate to 72%. If  $I_b$  is estimated at 1 000  $W/m^2$ , the reflected solar energy per unit area ( $S_r$ ) can be calculated at 720  $W/m^2$ . The solar radiation absorbed by the working fluid can be obtained by making use of Equation 3.7:

$$q_{sun} = C_R S_r \quad (3.7)$$

If it is assumed that  $q_{sun}$  is constant, the concentration ratio ( $C_R$ ) will be constant regardless of the receiver diameter. In such a case, the trough would be large for larger diameters but small for smaller diameters. For larger troughs, larger amounts of sun energy can be harvested. Therefore, it was decided to rather keep  $Q_{sun}$  constant in order to compare the performance of various diameters at a constant heat flux. In other words it is assumed that 2 000  $W/m^2$  falls on each unit section regardless of diameter. This will mean that different diameters will have different concentration ratios but the heat supplied to the working fluid will remain constant. Equation 3.8 describes how  $Q_{sun}$  relates to  $q_{sun}$ :

$$Q_{sun} = q_{sun} A_s \quad (3.8)$$

---

 CHAPTER 3. NUMERICAL WORK
 

---

Where  $A_s$  is the exposed heat transfer area and given by:

$$A_s = D_o \pi L \quad (3.9)$$

For a unit section, this simply becomes:

$$A_s = D_o \pi \quad (3.10)$$

Table 3.3 shows the various concentration ratios for the various diameters ranging from 15 mm to 50 mm. The larger diameters have small concentration ratios and vice versa. This is an advantage as far as the manufacturing and cost of the trough assembly is concerned because larger concentration ratios are often more difficult to achieve. Concentration ratios for parabolic trough concentrators are typically between 15 and 45 (Barlev *et al.*, 2011).

Table 3.3: Concentration ratios for various diameters for  $\dot{Q}_{sun} = 2\,000\text{ W}$  and  $S_r = 720\text{ W/m}^2$ .

$D_i$ <i>m</i>	$D_o$ <i>m</i>	$A_s$ $\text{m}^2$	$\dot{q}_{sun}$ $\text{kW/m}^2$	$C_R = \dot{q}_{sun}/S_r$ -
0.015	0.019	0.05969	33.5	47
0.02	0.024	0.0754	26.53	37
0.025	0.029	0.0911	21.95	30
0.03	0.034	0.10681	18.72	26
0.05	0.054	0.16965	11.78	16

## 3.7 LIQUID REGION

### 3.7.1 Solution Process

For the liquid section, the liquid temperature as well as the receiver surface temperatures will continually increase. For the liquid section (and superheated vapour section), the receiver pipe is discretised into unit lengths. The fluid outlet temperature and hence the wall temperatures are solved for each section. As soon as the wall temperatures are known, the heat losses and hence the entropy generated by finite temperature difference can be obtained. As mentioned, these unit lengths are seen as isothermal unit sections when calculating the entropy generation due to temperature differences. Furthermore, the pressure drop for each unit section is estimated by the equation presented in the previous chapter for single-phase flow (Equation 2.84). To obtain the total pressure drop, the pressure drop for each unit section is added. A flow diagram of the iterative process is shown in Figure 3.1.

The first estimate of the heat into the working fluid is taken as the total heat from the sun. From this, the bulk mean fluid temperature as well as the internal heat transfer coefficient can

CHAPTER 3. NUMERICAL WORK

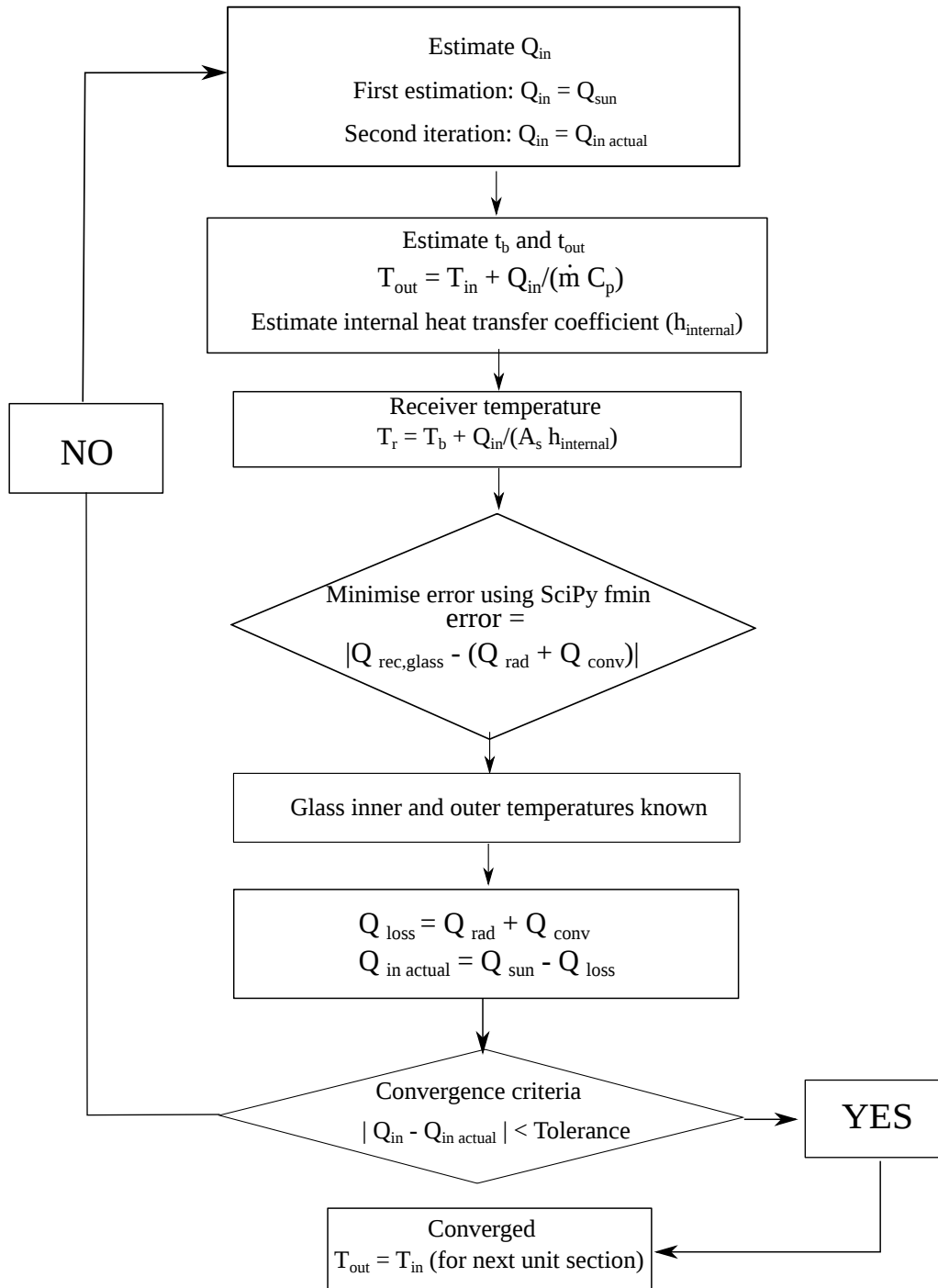


Figure 3.1: Iterative process for the solving of a unit section for the liquid and vapour single-phase regions.

be calculated. As soon as an estimation of the internal heat transfer coefficient is determined the receiver temperature can be calculated. Subsequently, the glass cover temperature can be

CHAPTER 3. NUMERICAL WORK

---

estimated by implementing an energy balance over the cover. The glass cover temperature is determined iteratively with an optimisation algorithm (fmin) in SciPy that minimises the error, using the Nelder-Mead simplex method. The error is given by Equation 3.11:

$$error = Q_{rad,rec-glass} - (Q_{conv,glass-amb} + Q_{rad,glass-sky}) \tag{3.11}$$

As soon as the glass cover temperature is known, the radiation and convection losses to ambient and the atmosphere can be obtained. Since these losses will lessen the initial assumed maximum value of the focused heat from the sun, the whole process must be repeated.  $Q_{sun} = Q_{in} = 2\ 000\ W$  for the unit section is an overestimation and the whole process must repeat until  $Q_{in}$  is sufficiently approximated. The outlet temperature of the section will be utilised as the inlet temperature for the subsequent section. For each unit section, these values are solved by the numerical code. Temperatures and losses for unit sections are solved until saturation temperature is reached for the liquid region.

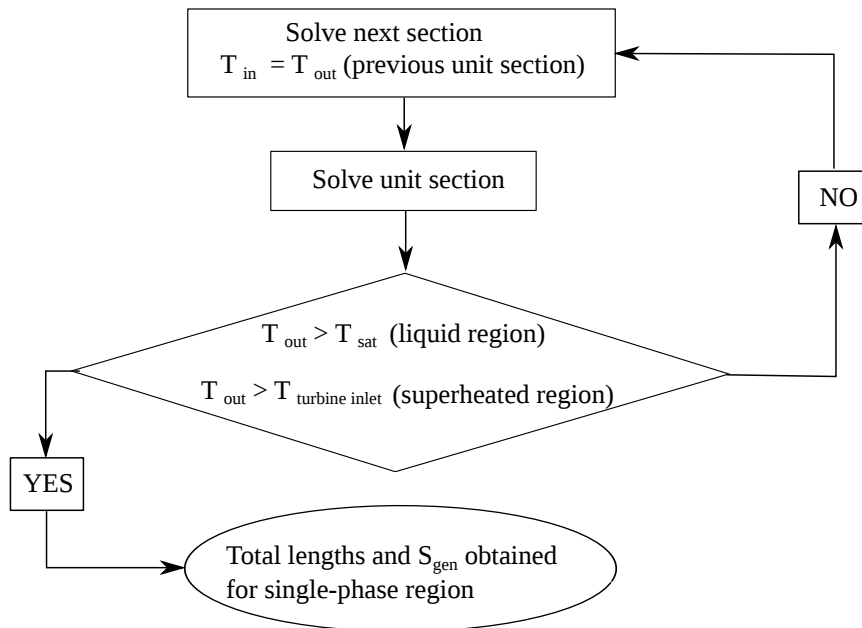


Figure 3.2: Process for obtaining the total entropy generation for an entire single-phase region.

This process is further depicted in Figure 3.2. For the superheated region, the losses are solved for each unit section until the turbine inlet temperature is reached. The entropy generation for these regions can be obtained by summation of entropy generation for each unit section.

### 3.7.2 Validation

This section serves as a validation of the correctness of the numerical code. Figure 3.3 shows how the temperature of the working fluid and receiver varies throughout the liquid region. The fluid

CHAPTER 3. NUMERICAL WORK

is heated from close to ambient conditions to saturation temperature. The receiver temperature remains slightly higher than the working fluid temperature.

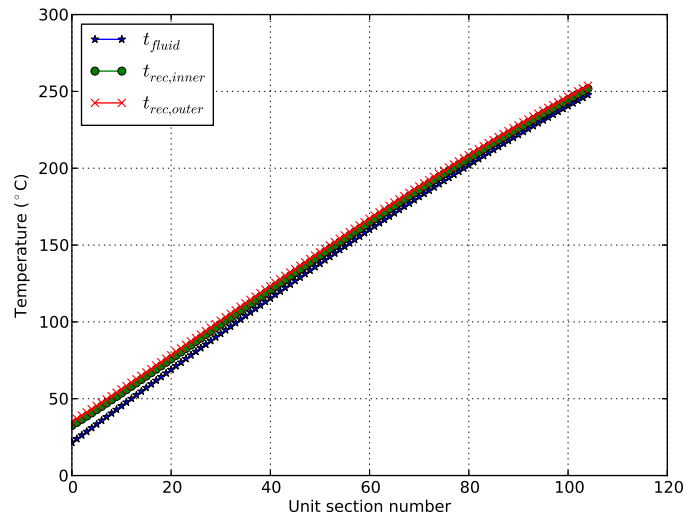


Figure 3.3: Fluid and receiver temperature changes throughout liquid region for  $D_i = 0.025\text{ m}$ ,  $\dot{m} = 0.2\text{ kg/s}$ ,  $T_{sat} = 250.4\text{ °C}$  and an operating pressure of  $4\text{ MPa}$ .

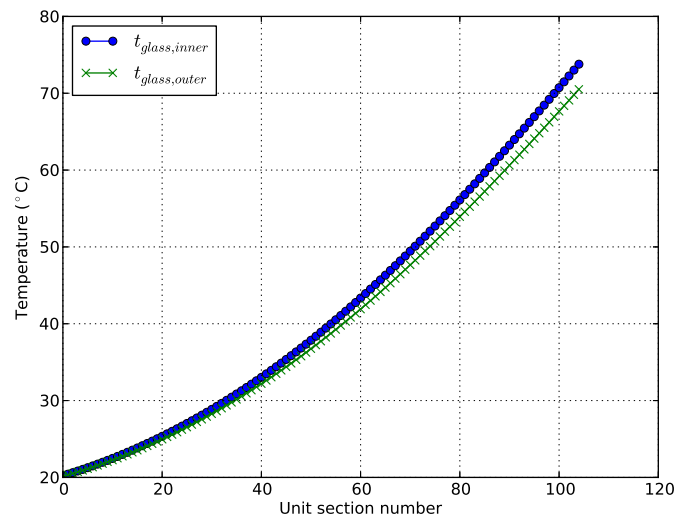


Figure 3.4: Glass cover temperature changes throughout liquid region for  $D_i = 0.025\text{ m}$ ,  $\dot{m} = 0.2\text{ kg/s}$ ,  $T_{sat} = 250.4\text{ °C}$  and an operating pressure of  $4\text{ MPa}$ .

From Figure 3.4, it can be seen that the inner-glass temperature is slightly higher than the outer-glass temperature. This effect is exaggerated for higher temperatures. Comparing Figure 3.4 with 3.3, it can be seen that the glass cover temperature is significantly lower than the

CHAPTER 3. NUMERICAL WORK

---

receiver temperature, which also shows that the glass cover improves the capability of the receiver to retain heat considerably. The glass temperature is raised from 20°C to approximately 73°C whereas the receiver temperature reaches a temperature slightly higher than saturation (250.4°C). If the receiver was exposed to the surroundings without the glass cover insulation, the heat losses would be much higher.

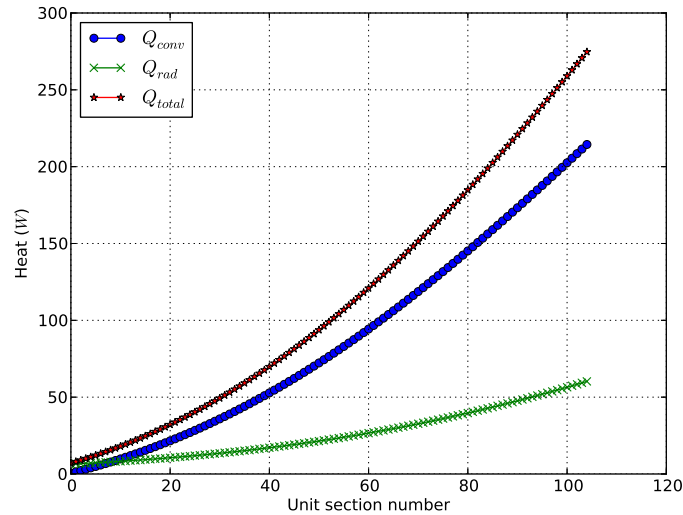


Figure 3.5: Heat losses throughout liquid region for  $D_i = 0.025\text{ m}$ ,  $\dot{m} = 0.2\text{ kg/s}$ ,  $T_{sat} = 250.4\text{ °C}$  and an operating pressure of  $4\text{ MPa}$ .

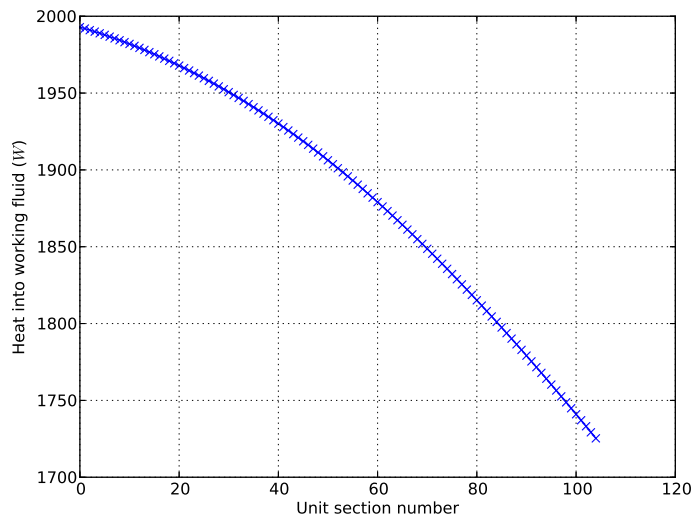


Figure 3.6: Heat into the working fluid for each liquid unit section where  $D_i = 0.025\text{ m}$ ,  $\dot{m} = 0.2\text{ kg/s}$ ,  $T_{sat} = 250.4\text{ °C}$  and an operating pressure of  $4\text{ MPa}$ .

CHAPTER 3. NUMERICAL WORK

---

Figure 3.5 shows the heat losses throughout the liquid region. It can be seen that the convection component contributes more to the losses. The convection losses are negligible for the first eight unit sections and only become significant as soon as the glass temperature rises above the ambient temperature. Even though the convection component is negligible at the start, it increases more steeply than the radiation component.

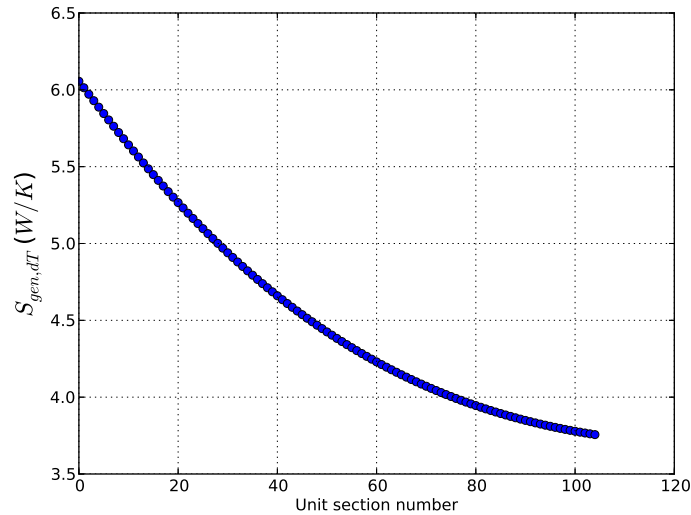


Figure 3.7: Entropy generation due to finite temperature differences for each liquid unit section where  $D_i = 0.025$  m,  $\dot{m} = 0.2$  kg/s,  $T_{sat} = 250.4$  °C and an operating pressure of 4 MPa.

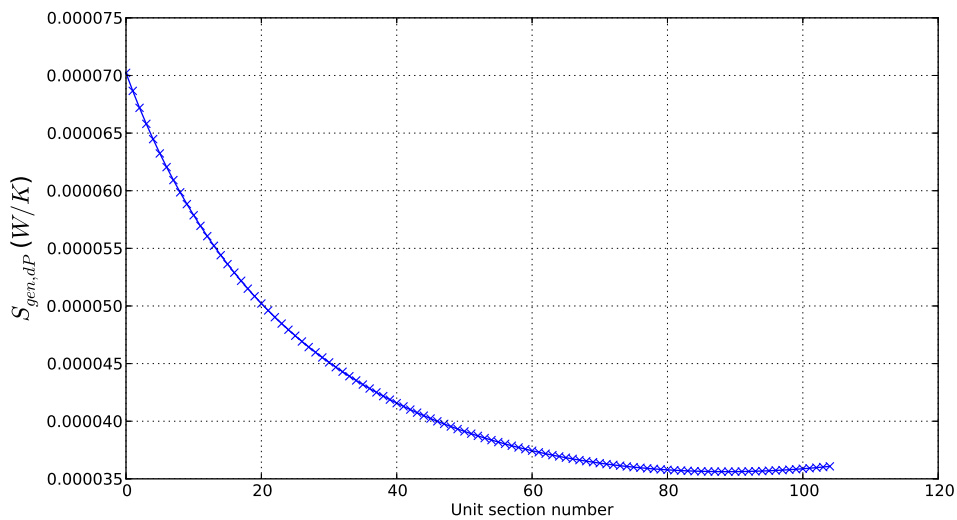


Figure 3.8: Entropy generation due to fluid friction for each liquid unit section where  $D_i = 0.025$  m,  $\dot{m} = 0.2$  kg/s,  $T_{sat} = 250.4$  °C and an operating pressure of 4 MPa.

## CHAPTER 3. NUMERICAL WORK

---

From Figure 3.6, it can be seen that the heat into the working fluid gets progressively lower as the receiver and glass temperatures are raised. The heat into the working fluid for each section drops from approximately  $2\,000\text{ W/m}^2$  when the receiver is at ambient conditions to  $1\,725\text{ W/m}^2$  when the receiver reaches saturation temperature.

Figure 3.7 and Figure 3.8 show how the entropy generation changes throughout the length of the liquid region. The entropy generation due to the finite temperature differences ( $S_{gen,dT}$ ) gets progressively smaller as the receiver heats up and  $S_{gen,dT}$  drops from approximately  $6\text{ W/K}$  to  $3.75\text{ W/K}$ . The entropy generation gets smaller as the receiver approaches an optimum temperature. For temperatures beyond the optimal,  $S_{gen,dT}$  starts to increase once more.

The entropy generation due to fluid friction ( $S_{gen,dP}$ ) drops from approximately  $7 \times 10^{-5}$  to  $3.5 \times 10^{-5}\text{ W/K}$  and reaches a minimum between the 80th and 100th section. When comparing the magnitude of  $S_{gen,dP}$  with that of  $S_{gen,dT}$ , it can be seen that  $S_{gen,dP}$  is minuscule.

## 3.8 TWO-PHASE REGION

### 3.8.1 Solution Process

#### Temperature

The internal heat transfer coefficient is a function of the quality and changes depending on the flow regime inside the tube. The internal heat transfer coefficient is solved for a quality range from 1% up to nearly 100% in increments of 2%. The length for each 2% quality change varies throughout the receiver tube. The summation of these lengths yields the total length. The procedure as described by Wojtan *et al.* (2005a,b) is used to solve the internal heat transfer coefficient. The numerical code, pertaining to the determination of the two-phase heat transfer coefficient, was compared with data obtained from Wojtan *et al.* (2005b) for refrigerant R22 and is shown in Appendix A. The numerical values obtained by the code show good agreement with the data from Wojtan *et al.* (2005b). As soon as the internal heat transfer coefficient is obtained, the receiver-wall temperature can be estimated. Accordingly, the glass cover temperature as well as the losses can be obtained with the procedure discussed in the previous section. The heat into the first section of the two-phase region is estimated at the heat into the last section of the liquid region. Furthermore, the first estimate for the glass temperature is taken as the temperature for the last section of the liquid region. Figure 3.9 depicts the iterative procedure that is followed for the two-phase region. The process remains very similar to the solving of the single-phase regions but instead of unit sections, the region is solved for each section that undergoes a 2% quality change. Note that Figure 3.9 only refers to the solving of the temperatures.

#### Pressure Drop

The pressure drop for the two-phase region was estimated by utilising the Friedel two-phase flow multiplier. The two-phase flow multiplier is estimated for each 2% quality change as is done

CHAPTER 3. NUMERICAL WORK

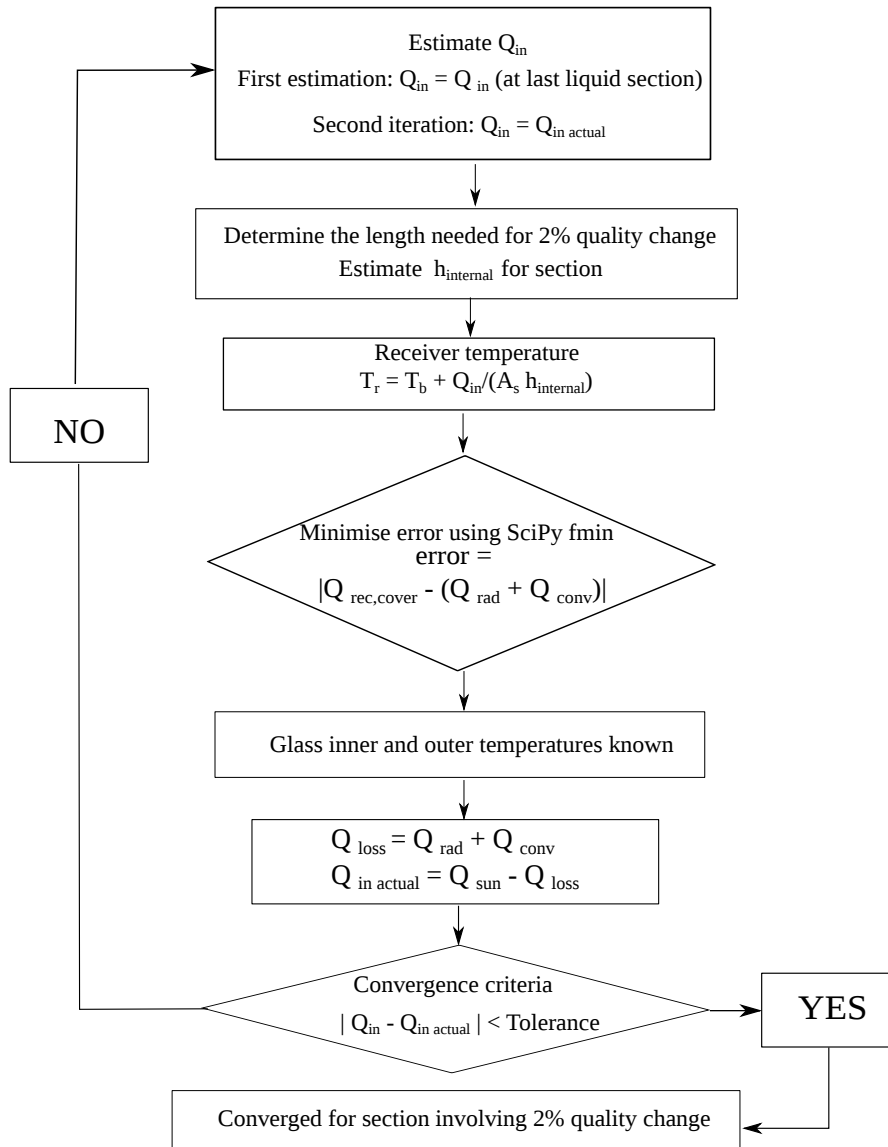


Figure 3.9: Iterative process for the solving of a section for the two-phase regions.

for the determination of  $S_{gen,dT}$ . Figure 3.10 shows how the two-phase multiplier varies for the quality range. The liquid pressure drop ( $\Delta P_L$ ) remains more or less constant for a specific operating pressure and mass flow rate, however, the length of each section in the two-phase region is not necessarily constant. This is due to the fact that the receiver temperature (and hence the losses) also vary slightly throughout the region. Note, however, that the receiver temperature remains close to the water saturation temperature (but not exact) if the heat transfer coefficient is very high. Also note that the multiplier will change if operating conditions change. Changhong *et al.* (2005) showed that an increase in operating pressure results in a decrease of the overall value of the two-phase flow multiplier. To determine the two-phase pressure drop for each section, the liquid pressure drop is multiplied with the Friedel two-

## CHAPTER 3. NUMERICAL WORK

---

phase multiplier. The pressure drop for the entire region can be determined by summing the pressure drops for each section. Furthermore, the entropy generation is also determined for each individual section since the density of the liquid mixture changes dramatically throughout the region.

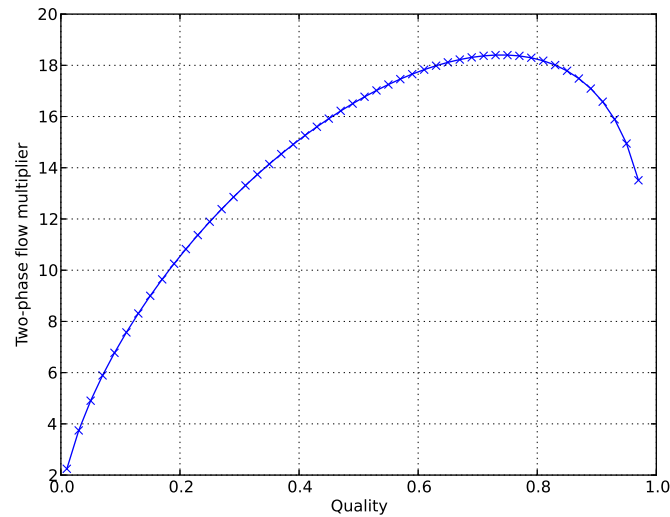


Figure 3.10: Two-phase multiplier for the quality range where  $D_i = 0.025\text{ m}$ ,  $\dot{m} = 0.2\text{ kg/s}$ ,  $T_{sat} = 250.4\text{ }^\circ\text{C}$  and an operating pressure of  $4\text{ MPa}$ .

### 3.8.2 Validation

Figure 3.11 shows the changes in heat transfer coefficient for the quality range. At  $x = 0.93$  dryout occurs and the heat transfer coefficient rapidly drops to lower values. As can be seen, the heat transfer coefficient for the two-phase flow region is quite large before dryout is reached.

Figure 3.12 shows the fluid temperature as well as the receiver inner and outer temperature. The receiver inner and outer temperatures are highly dependent on the heat transfer coefficient and as soon as the tube experiences dryout, temperature spikes are perceived in the receiver temperature. The same effect is seen in the glass cover temperatures shown in Figure 3.13.

When inspecting Figure 3.14, it can be seen that the heat into the fluid also drops as soon as the tube undergoes the temperature spike. This has the effect of increasing  $S_{gen,dT}$  as well and can be validated with Figure 3.15.

The entropy due to fluid friction for the quality range is shown in Figure 3.16.  $S_{gen,dP}$  rises and reaches a peak at a quality value of approximately  $x = 0.87$ . The form of this graph is different when compared to the previous graphs in this section. This is due to the fact that the major influences on  $S_{gen,dP}$  is the two-phase multiplier and the specific volume of the fluid and not the heat transfer coefficient.

CHAPTER 3. NUMERICAL WORK

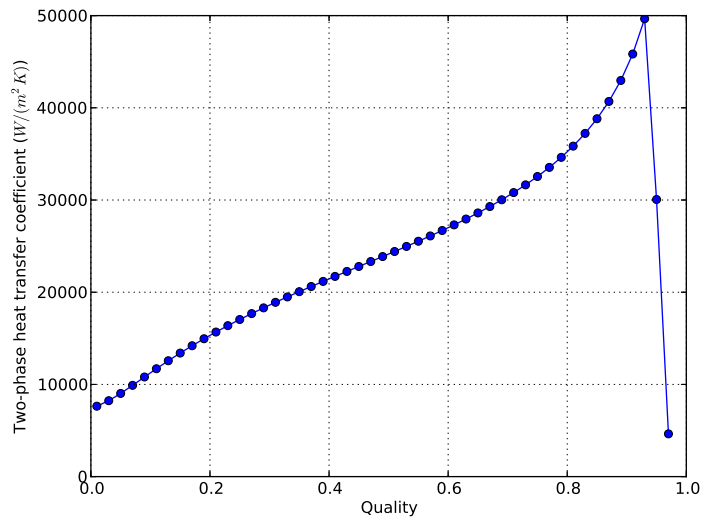


Figure 3.11: Change in heat transfer coefficient for the quality range where  $D_i = 0.025\text{ m}$ ,  $\dot{m} = 0.2\text{ kg/s}$ ,  $T_{sat} = 250.4\text{ °C}$  and an operating pressure of  $4\text{ MPa}$ .

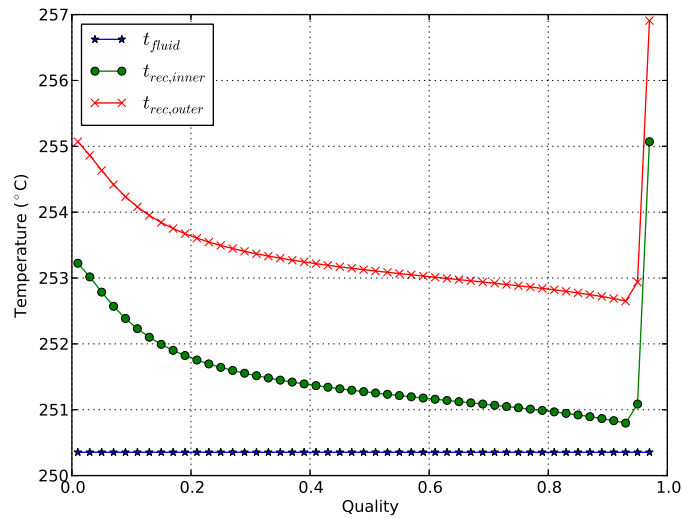


Figure 3.12: Change in receiver temperatures for the quality range where  $D_i = 0.025\text{ m}$ ,  $\dot{m} = 0.2\text{ kg/s}$ ,  $T_{sat} = 250.4\text{ °C}$  and an operating pressure of  $4\text{ MPa}$ .

### 3.9 VAPOUR REGION

#### 3.9.1 Solution Process

The vapour region is handled in the same manner as the liquid region. The working fluid is now heated from saturated vapour to the turbine inlet temperature. The turbine inlet temperature

CHAPTER 3. NUMERICAL WORK

---

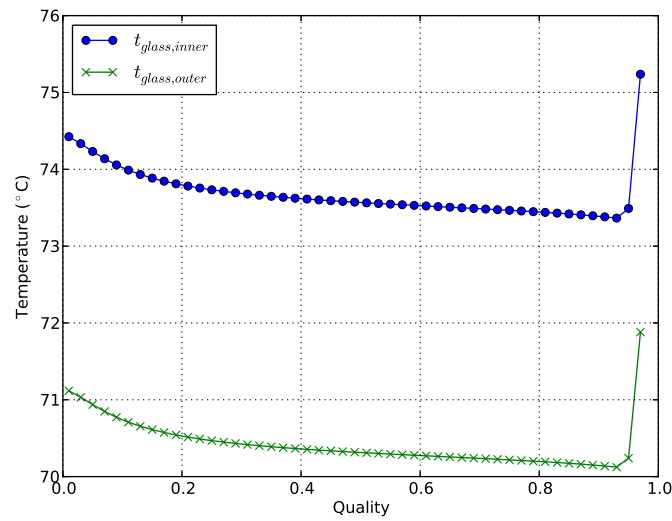


Figure 3.13: Change in glass temperatures for the quality range where  $D_i = 0.025\ m$ ,  $\dot{m} = 0.2\ kg/s$ ,  $T_{sat} = 250.4\ ^\circ C$  and an operating pressure of  $4\ MPa$ .

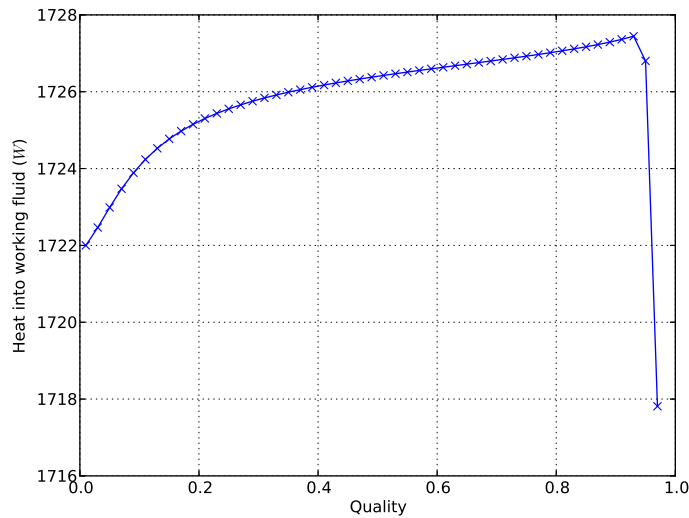


Figure 3.14: Heat into the working fluid for the quality range where  $D_i = 0.025\ m$ ,  $\dot{m} = 0.2\ kg/s$ ,  $T_{sat} = 250.4\ ^\circ C$  and an operating pressure of  $4\ MPa$ .

often depends on the specific turbine being used but for this numerical model, no turbine is specified thus an assumption is made that the turbine inlet temperature is 20% higher than the saturation temperature. It is recognised that for higher saturation temperatures and hence higher turbine inlet temperatures, more work can be extracted from the working fluid. Furthermore, the mass flow rate also has an influence on the amount of work available. The heat transfer

CHAPTER 3. NUMERICAL WORK

---

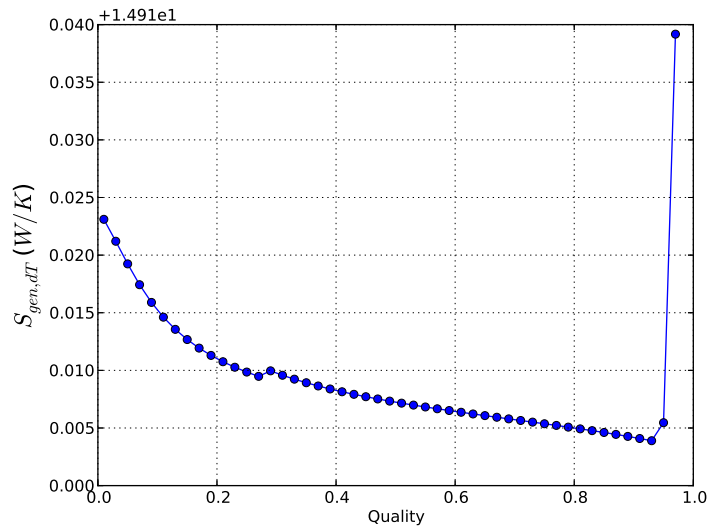


Figure 3.15: Entropy generation due to finite temperature differences for the quality range where  $D_i = 0.025\text{ m}$ ,  $\dot{m} = 0.2\text{ kg/s}$ ,  $T_{sat} = 250.4\text{ °C}$  and an operating pressure of  $4\text{ MPa}$ .

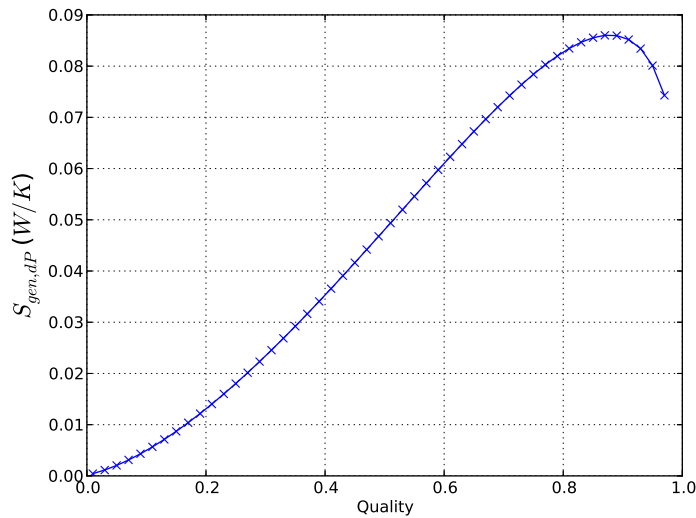


Figure 3.16: Entropy generation due to fluid friction differences for the quality range where  $D_i = 0.025\text{ m}$ ,  $\dot{m} = 0.2\text{ kg/s}$ ,  $T_{sat} = 250.4\text{ °C}$  and an operating pressure of  $4\text{ MPa}$ .

coefficient is determined with the Gnielinsky correlation as was done for the liquid region. The superheated region is often shorter than the other regions but high fluid velocities in this region can result in significant friction losses. Furthermore, due to the fact that the temperatures are higher, the entropy generation due to temperature differences can also be quite high.

## CHAPTER 3. NUMERICAL WORK

### 3.9.2 Validation

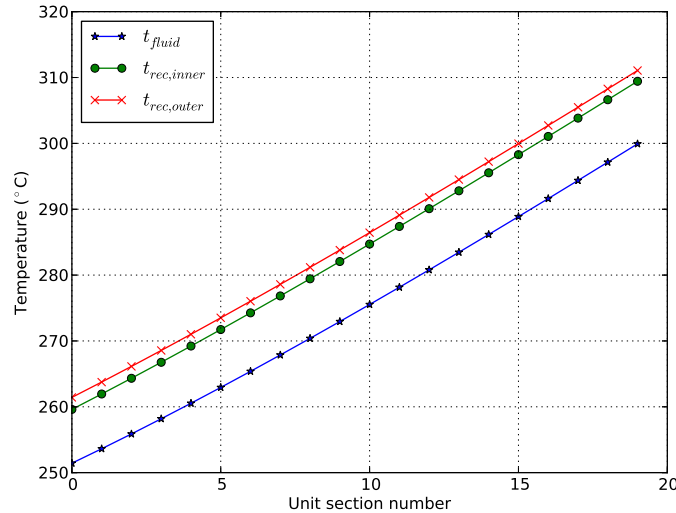


Figure 3.17: Fluid and receiver temperature changes throughout the superheated vapour region where  $D_i = 0.025 \text{ m}$ ,  $\dot{m} = 0.2 \text{ kg/s}$ ,  $T_{sat} = 250.4 \text{ }^\circ\text{C}$  and an operating pressure of  $4 \text{ MPa}$ .

From Figure 3.17, it can be seen that the fluid temperature rises systematically while the receiver inner and outer temperatures remains slightly higher than the fluid temperature. The same tendency can be seen in Figure 3.18 with the exception of lower inner- and outer-cover temperatures. The glass cover temperature in turn has an effect on the heat losses and a systematic increase in heat losses can be seen in Figure 3.19. It can also be observed that the vapour region length is much shorter than the length of the liquid and two-phase region (cf. Table 4.1 and Table 4.2).

The heat into the working fluid drops from approximately  $Q_{in} = 1 \text{ 710 W}$  to about  $1 \text{ 580 W}$ . This is due to the rise in temperature of the glass cover. As the heat into the working fluid diminishes, longer receiver lengths are needed to reach the required temperature.

Figure 3.21 and Figure 3.22 depict the progression of  $S_{gen,dT}$  and  $S_{gen,dP}$ , respectively.  $S_{gen,dT}$  drops and reaches a minimum between sections 15 and 16. Increases in  $S_{gen,dT}$  can be observed beyond this point as the receiver heats up to temperatures higher than optimal.  $S_{gen,dP}$  rises as the fluid velocity increases and the density decreases.

## 3.10 CONCLUSION

This chapter dealt with the validation of the numerical code. A base case with an operating pressure of  $4 \text{ MPa}$ , mass flow rate of  $0.2 \text{ kg/s}$  and a tube diameter of  $0.025 \text{ m}$  was investigated. The optical efficiency of the trough was assumed to be  $72\%$  and a constant heat flux of

CHAPTER 3. NUMERICAL WORK

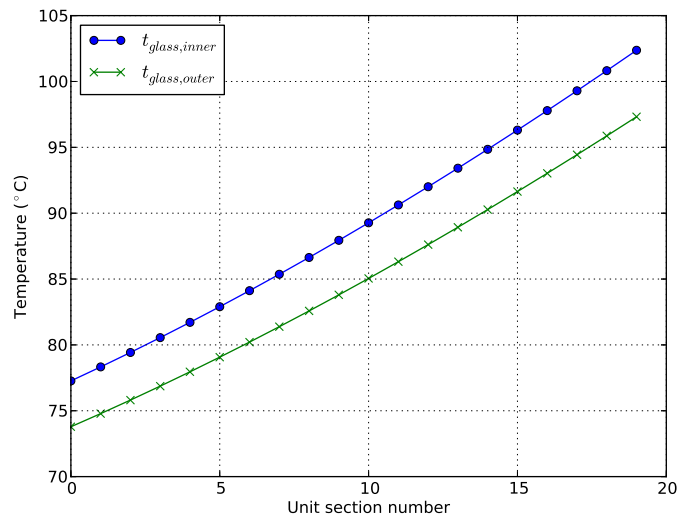


Figure 3.18: Glass cover temperature changes throughout the superheated vapour region where  $D_i = 0.025\text{ m}$ ,  $\dot{m} = 0.2\text{ kg/s}$ ,  $T_{sat} = 250.4\text{ °C}$  and an operating pressure of  $4\text{ MPa}$ .

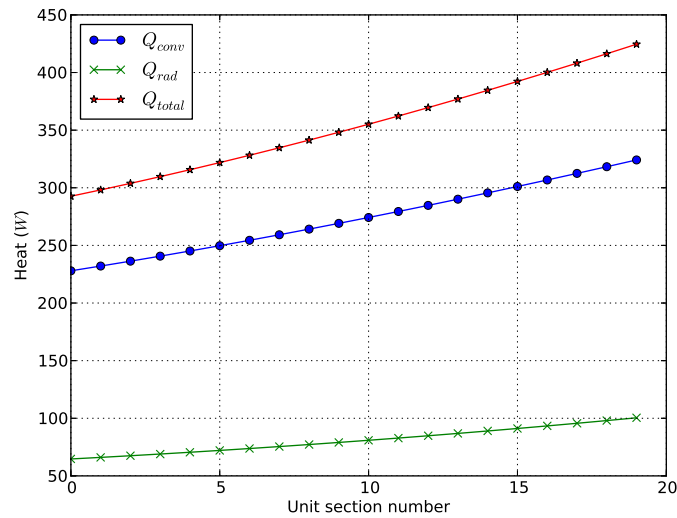


Figure 3.19: Heat losses for each superheated vapour unit section where  $D_i = 0.025\text{ m}$ ,  $\dot{m} = 0.2\text{ kg/s}$ ,  $T_{sat} = 250.4\text{ °C}$  and an operating pressure of  $4\text{ MPa}$ .

$2\ 000\text{ W/m}^2$  is assumed for all tube diameters. This, however, means that different diameters need different concentration ratios, for example, larger diameters will require smaller concentration ratios to reach the same amount of focused heat than smaller diameters. This can be viewed as an additional advantage when considering larger diameters, since large concentration ratios are harder to achieve.

CHAPTER 3. NUMERICAL WORK

---

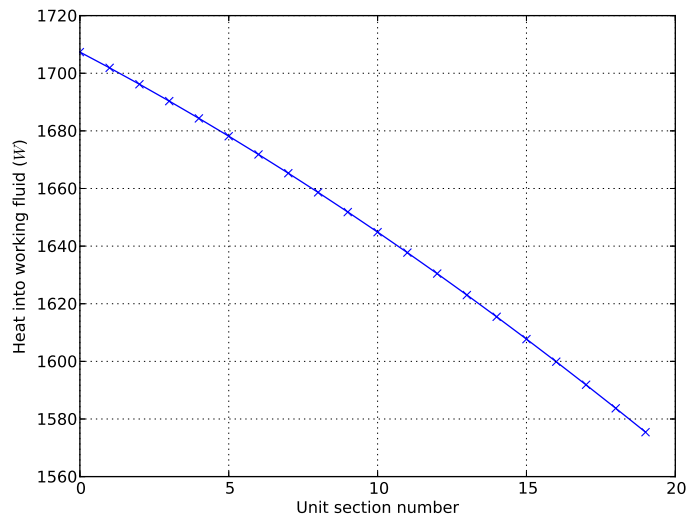


Figure 3.20: Heat into the working fluid for each superheated vapour unit section where  $D_i = 0.025\text{ m}$ ,  $\dot{m} = 0.2\text{ kg/s}$ ,  $T_{sat} = 250.4\text{ }^\circ\text{C}$  and an operating pressure of  $4\text{ MPa}$ .

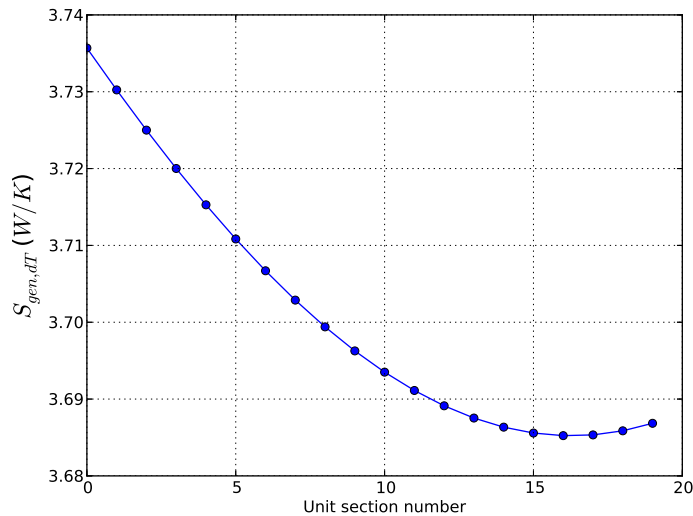


Figure 3.21: Entropy generation due to finite temperature differences for each liquid unit section where  $D_i = 0.025\text{ m}$ ,  $\dot{m} = 0.2\text{ kg/s}$ ,  $T_{sat} = 250.4\text{ }^\circ\text{C}$  and an operating pressure of  $4\text{ MPa}$ .

The iterative procedures are discussed and shown schematically for the single-phase region as well as the two-phase region. The solving of each region (i.e. liquid, two-phase and superheated) is discussed and it can be seen that the heat into the working fluid diminishes as higher temperatures are reached. This, in turn, influences the entropy generation. The liquid and superheated (or vapour) regions involve the solving of unit sections while the two-phase region involves the

CHAPTER 3. NUMERICAL WORK

---

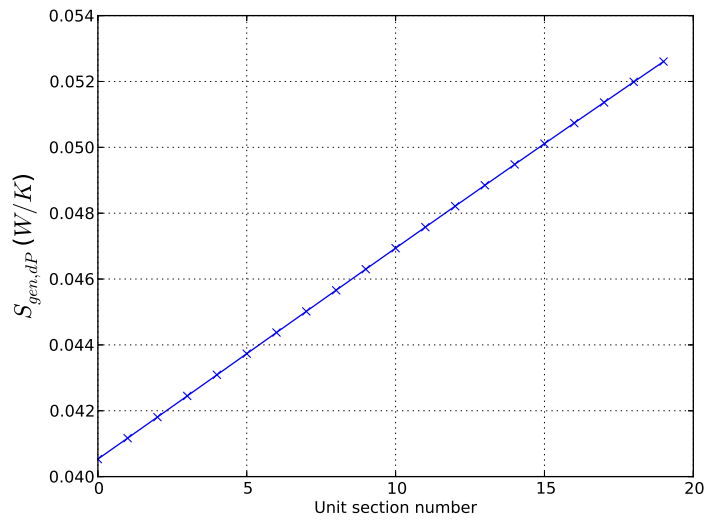


Figure 3.22: Entropy generation due to fluid friction for each superheated unit section where  $D_i = 0.025\text{ m}$ ,  $\dot{m} = 0.2\text{ kg/s}$ ,  $T_{sat} = 250.4\text{ }^\circ\text{C}$  and an operating pressure of  $4\text{ MPa}$ .

solving of each section that undergoes a 2% quality change. The sections in the two-phase region are often longer than 1 metre but the temperature variation along the length is not as prominent as for the single-phase regions.

---

---

# CHAPTER 4

---

## RESULTS

### 4.1 INTRODUCTION

This chapter discusses the results that were obtained with the numerical analysis. In this chapter, various operating pressures are investigated as well as the influence of the mass flow rate and receiver tube diameter. Operating pressures 1 *MPa* to 9 *MPa* are investigated. The first section shows the effect that the operating pressure has on the various region lengths (liquid, two-phase and vapour). Next, the entropy generation is investigated. Results are shown for  $S_{gen,dT}$  and  $S_{gen,dP}$  as well as the total entropy generation. In the final section, sensitivity analysis is conducted on the effective sky temperature ( $T_{sky}$ ), wind velocity, glass cover clearance and the maximum focused heat per unit section ( $Q_{sun}$ ).

### 4.2 REGION LENGTHS

Table 4.1 shows the various lengths for the respective regions for a high and a low mass flow rate. It can be seen that the two-phase length actually decreases as the operating pressure increases. The liquid and vapour regions tend to increase for higher operating pressures since higher saturation temperatures and turbine inlet temperatures can be expected to increase the required heat. When considering the total length needed, shorter two-phase region lengths tend to offset higher single-phase region lengths, and the total length does not increase exceptionally when considering two consecutive operating pressures. For example, for an operating pressure of 8 *MPa* and low mass flow rate, the total length needed is 241 *m* while for 9 *MPa* it is 243 *m*.

It can also be noticed that the vapour region tends to be much shorter than the other regions. Liquid regions can become long for high operating pressures and especially for high mass flow

## CHAPTER 4. RESULTS

 Table 4.1: Region-length comparison for a high and low mass flow rate and inner-tube diameter of  $D_i = 15 \text{ mm}$ .

Operating pressure (MPa)	$\dot{m} = 0.15 \text{ kg/s}$				$\dot{m} = 0.4 \text{ kg/s}$			
	Liquid (m)	Two-phase (m)	Vapour (m)	Total (m)	Liquid (m)	Two-phase (m)	Vapour (m)	Total (m)
1	51	156	8	215	138	416	19	573
2	63	149	10	222	169	398	26	593
3	71	143	12	226	190	384	32	606
4	77	139	14	230	207	371	37	615
5	83	134	16	233	222	360	42	624
6	88	130	18	236	235	348	48	631
7	92	126	20	238	247	337	53	637
8	97	122	22	241	258	326	59	643
9	100	118	25	243	268	315	64	647

rates. For example, the liquid length of the high mass flow case for the highest operating pressure is 268 m.

The same tendencies can be seen in the regions for a receiver tube of larger diameter shown in Table 4.2. Generally, the lengths tend to be longer for the larger diameter case. This is due to the fact that there are more losses but also due to the fact that the two-phase flow regimes remain in stratified-wavy (SW) zone as well as slug+SW zone for a large diameter of 50 mm. This is not necessarily the case for smaller diameters since smaller diameters result in higher mass velocities, which ultimately results in more wetting of the tube perimeter. Note that the results for a high mass flow rate are not shown in Table 4.2 since they are repetitive to the results shown.

 Table 4.2: Region-length comparison for low mass flow rate of  $\dot{m} = 0.15 \text{ kg/s}$  and inner-tube diameter of  $D_i = 50 \text{ mm}$ .

Operating pressure (MPa)	$\dot{m} = 0.15 \text{ kg/s}$			
	Liquid (m)	Two-phase (m)	Vapour (m)	Total (m)
1	54	170	9	233
2	67	168	12	247
3	76	167	15	258
4	84	166	19	269
5	90	164	22	276
6	97	163	25	285
7	102	161	29	292
8	108	159	33	300
9	113	157	37	307

## 4.3 ENTROPY GENERATION

### 4.3.1 Entropy Generation due to Finite Temperature Differences

Shown in Figure 4.1 is  $S_{gen,dT}$  for lower operating pressures (1 MPa to 5 MPa). Figure 4.1 (a) is plotted for a low mass flow rate of 0.15 kg/s and Figure 4.1 (b) is plotted for a high mass flow rate of 0.4 kg/s.  $S_{gen,dT}$  increases more or less linearly as the inner-tube diameter increases. This is due to an increase in the area exposed to the surroundings. An increase in exposed area will ultimately result in the increase of heat losses to the surroundings.

When  $S_{gen,dT}$  for the low mass flow is compared with that of the high mass flow, it can be seen that the numerical values of the high mass flow are approximately 2.667 times greater due to the mass flow being 2.667 times greater. Therefore, it can be seen that increasing the mass flow has a linear effect on  $S_{gen,dT}$ .

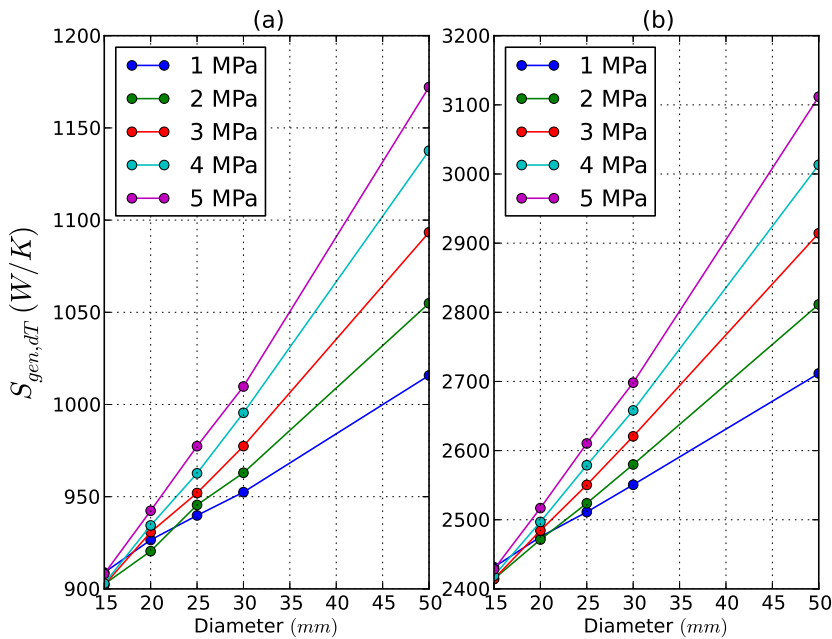


Figure 4.1: Entropy generation due to finite temperature differences for low operating pressures 1 MPa to 5 MPa. (a)  $\dot{m} = 0.15$  kg/s, (b)  $\dot{m} = 0.4$  kg/s

From Figure 4.1, it can also be noted that for a low operating pressure (1 MPa) and smaller diameters (15 mm and 20 mm),  $S_{gen,dT}$  tends to be more than for higher operating pressure (and higher saturation temperature). This seems counter to what one would expect but this is due to the fact that the two-phase region is much longer for lower operating pressures, and furthermore when inspecting the heat transfer coefficient over the region (for 1 MPa), it can be seen that a larger part of the region is in the misty flow regime accounting for much higher receiver temperatures (and more losses) in that regime and for that operating pressure. This

CHAPTER 4. RESULTS

tendency is shown in Figure 4.2, where it can be seen that dryout is reached at a quality of just under 70%. The flow then moves into the misty regime for which the heat transfer coefficient is much lower.

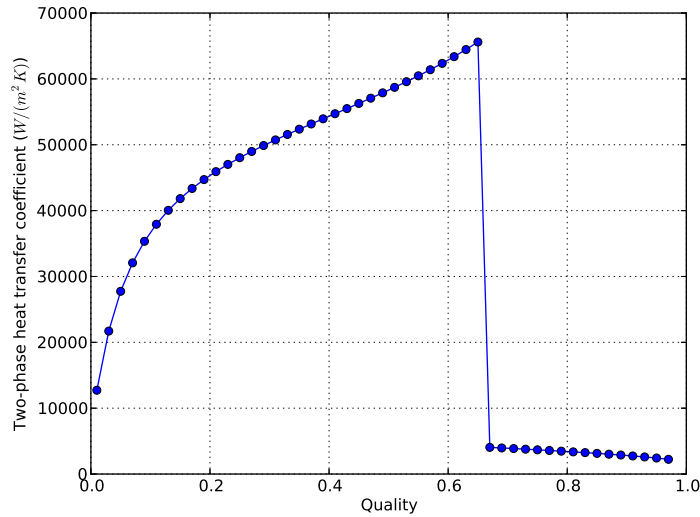


Figure 4.2: Heat transfer coefficient for 1 MPa,  $\dot{m} = 0.15 \text{ kg/s}$  and  $D_i = 15 \text{ mm}$ .

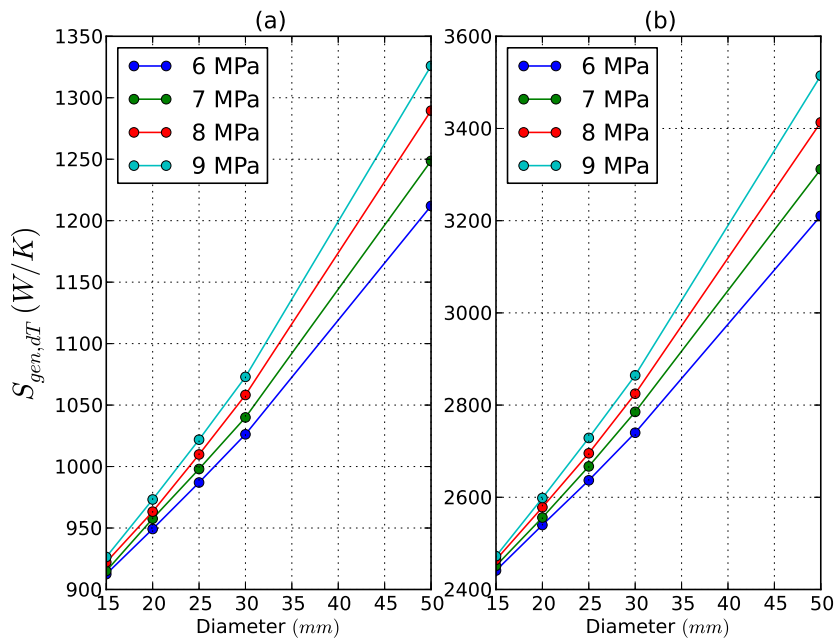


Figure 4.3: Entropy generation due to finite temperature differences for high operating pressures of 6 MPa to 9 MPa. (a)  $\dot{m} = 0.15 \text{ kg/s}$ , (b)  $\dot{m} = 0.4 \text{ kg/s}$

CHAPTER 4. RESULTS

Figure 4.3 shows  $S_{gen,dT}$  for higher operating pressures (6 MPa to 9 MPa). Once again, Figure 4.3 (a) shows the result for a low mass flow rate of 0.15 kg/s and (b) is for a mass flow rate of 0.4 kg/s. As can be expected for higher operating pressures, the entropy generation is more (due to higher saturation temperatures). Furthermore, for higher mass flow rates,  $S_{gen,dT}$  is higher. For larger diameters, the jump in  $S_{gen,dT}$  is larger than for smaller diameters when considering various operating pressures.

Furthermore, what is also perceived is that for larger diameters ( $D_i = 50\text{ mm}$ ) the main regimes encountered in the two-phase region are the stratified-wavy (SW) and SW+slug regimes. For these regimes, the heat transfer coefficient is lower than for the annular and intermittent zones thus adding to the losses from the receiver in this region.

4.3.2 Entropy Generation due to Fluid Friction

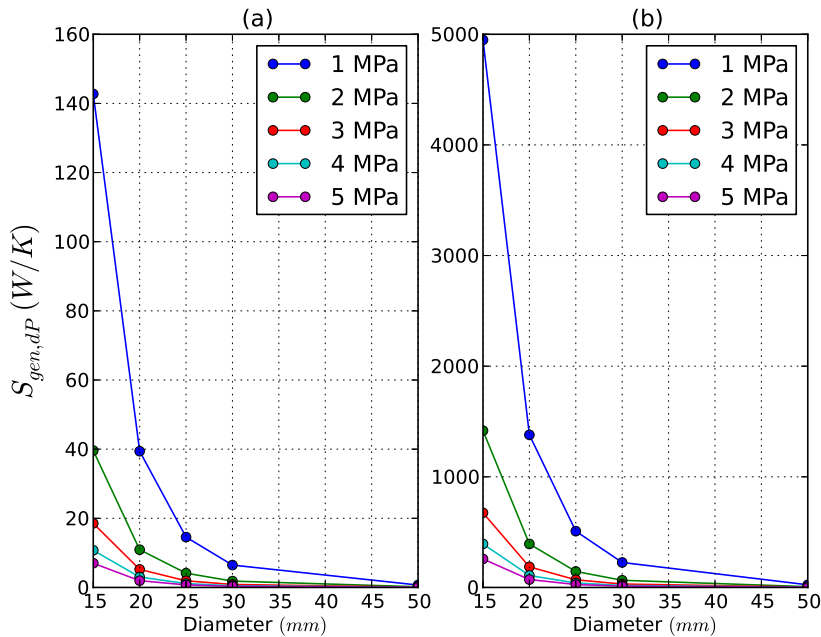


Figure 4.4: Entropy generation due to fluid friction for low operating pressures 1 MPa to 5 MPa. (a)  $\dot{m} = 0.15\text{ kg/s}$ , (b)  $\dot{m} = 0.4\text{ kg/s}$

Shown in Figure 4.4 is  $S_{gen,dP}$  for the lower operating pressures from 1 MPa to 5 MPa. Furthermore, Figure 4.4 (a) is plotted for a low mass flow rate of 0.15 kg/s and Figure 4.1 (b) is plotted for a high mass flow rate of 0.4 kg/s.

Unlike  $S_{gen,dT}$ , the entropy generation due to friction will increase for smaller tube diameters. This tendency is exaggerated for lower operating pressures. Higher operating pressures tend to increase the fluid density in the compressible regions and this can have the effect of lowering the pressure drop, and ultimately, the entropy generation due to friction.

CHAPTER 4. RESULTS

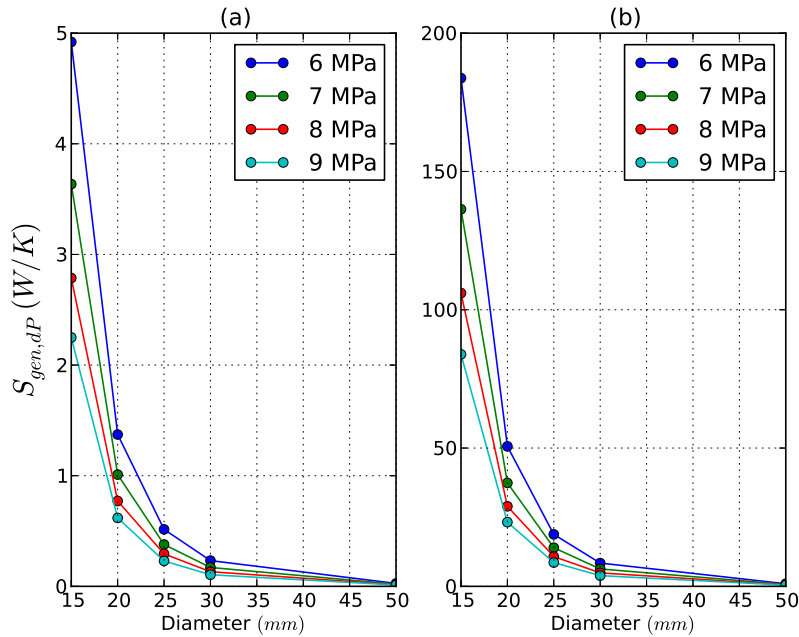


Figure 4.5: Entropy generation due to fluid friction for high operating pressures of 6 MPa to 9 MPa. (a)  $\dot{m} = 0.15 \text{ kg/s}$ , (b)  $\dot{m} = 0.4 \text{ kg/s}$

From Figure 4.4 (a) it can be seen that  $S_{gen,dP}$  tends to be very small and almost negligible for operating pressures higher than 2 MPa since  $S_{gen,dP}$  is below 20 W/K for 3 MPa, 4 MPa and 5 MPa. From Figure 4.4 (b) it can be seen that for high mass flow rates and low operating pressures  $S_{gen,dP}$  tends to be excessive (approximately 5000 W/K and exceeding the value for  $S_{gen,dT}$  at the highest operating pressure and largest diameter). For 3 MPa, 4 MPa and 5 MPa the entropy generation is below 1000 W/K.

Further reason for the high pressure drops at the lower operating pressures is the high two-phase multiplier for these conditions. The fact that  $S_{gen,dP}$  is smaller for higher operating pressures is partly due to the Friedel two-phase flow multiplier being less and thus decreasing the pressure drop in the two-phase region. This can be validated by inspecting Table 4.3. As discussed before, the two-phase region tends to be very long for lower operating pressures (cf. Table 4.1).

Figure 4.5 shows  $S_{gen,dP}$  for the higher operating pressures (6 MPa to 9 MPa). The same tendencies are observed as before. As before,  $S_{gen,dP}$  is lowered as the operating pressure and diameter increase. When investigating the numerical values for Figure 4.5 (a), at a small tube diameter, the entropy generation ranges between 2 W/K and 5 W/K indicating that it is negligible when compared with  $S_{gen,dT}$  for the same conditions, which range between 900 W/K and 950 W/K.

CHAPTER 4. RESULTS

Table 4.3: Average Friedel two-phase flow multiplier and corresponding pressure drop for two-phase flow region where  $\dot{m} = 0.2 \text{ kg/s}$  and an inner-tube diameter of  $D_i = 25 \text{ mm}$ .

Operating pressure (MPa)	Friedel multiplier( $\Phi^2$ ) (-)	Pressure drop (kPa)
1	43.81	684.5
2	25.49	384.1
3	18.23	268.98
4	14.2	206.2
5	11.58	166.02
6	9.78	137.7
7	8.34	116.5
8	7.25	99.86
9	6.36	86.4

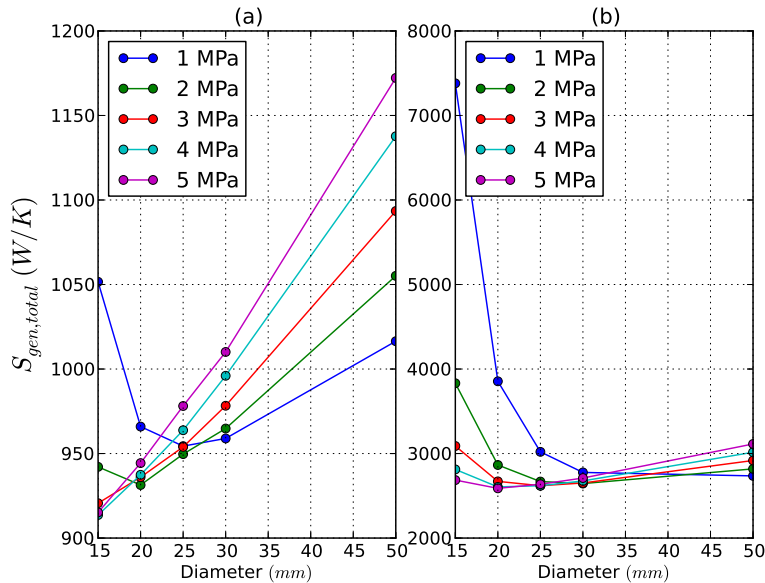


Figure 4.6: Total entropy generation for low operating pressures of 1 MPa to 5 MPa. (a)  $\dot{m} = 0.15 \text{ kg/s}$ , (b)  $\dot{m} = 0.4 \text{ kg/s}$

### 4.3.3 Total Entropy Generation

As was done in the previous sections, Figure 4.6 is plotted for lower operating pressures (1 MPa to 5 MPa) where (a) is for a low mass flow rate and (b) is for a high mass flow. From (a), it can be seen that only lower operating pressures (1 MPa to 3 MPa) are influenced by  $S_{gen,dP}$  at small diameters causing the entropy generation to spike for those conditions. Larger diameters are almost exclusively influenced by  $S_{gen,dT}$ .

When inspecting Figure 4.6 (b), it can be seen that higher mass flow rates also result in  $S_{gen,dP}$

CHAPTER 4. RESULTS

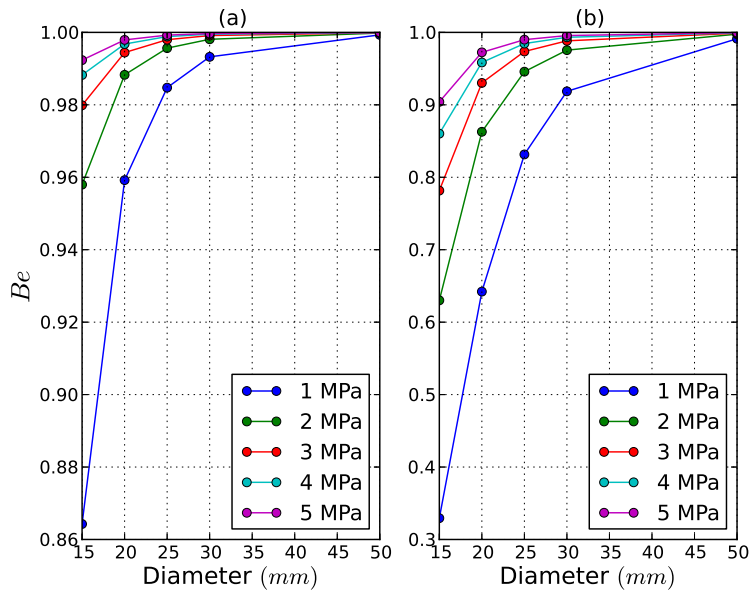


Figure 4.7: Bejan number for low operating pressures of 1 MPa to 5 MPa. (a)  $\dot{m} = 0.15 \text{ kg/s}$ , (b)  $\dot{m} = 0.4 \text{ kg/s}$

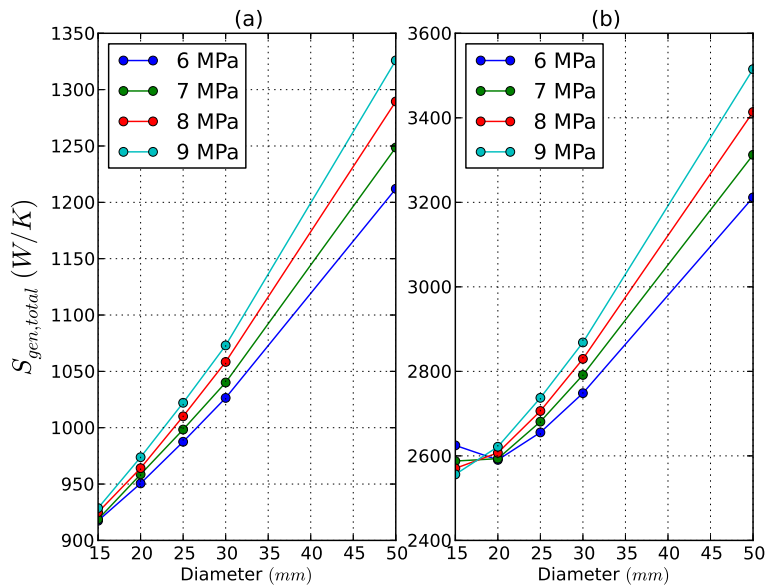


Figure 4.8: Total entropy generation for high operating pressures of 6 MPa to 9 MPa. (a)  $\dot{m} = 0.15 \text{ kg/s}$ , (b)  $\dot{m} = 0.4 \text{ kg/s}$

being more prevalent for all the operating pressures. This behaviour can be conveniently described by plotting the Bejan number.

CHAPTER 4. RESULTS

---

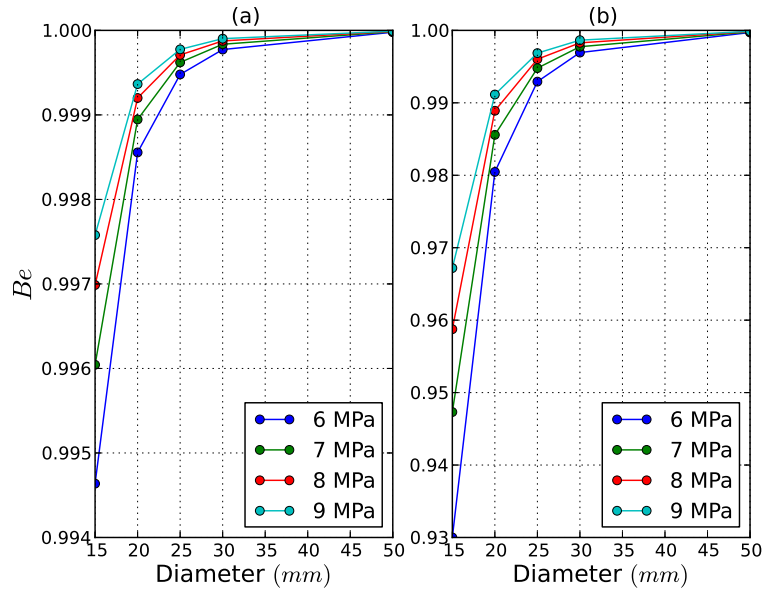


Figure 4.9: Bejan number for high operating pressures of 6 MPa to 9 MPa. (a)  $\dot{m} = 0.15 \text{ kg/s}$ , (b)  $\dot{m} = 0.4 \text{ kg/s}$

The Bejan number ( $Be$ ) is plotted in Figure 4.7. Values close to unity indicate that  $S_{gen,dT}$  is the main contributor to the total entropy generation. When inspecting Figure 4.7, (b)  $Be$  is not close to unity for smaller diameters and lower operating pressures.

Figure 4.8 and Figure 4.9 show the results for higher operating pressures (6 MPa to 9 MPa). From Figure 4.8 (a) and Figure 4.9 (a), it can be seen that  $S_{gen,dT}$  is the main contributor. From Figure 4.8 (b) and Figure 4.9 (b), it can be seen that operating pressure 6 MPa and 7 MPa are slightly influenced by  $S_{gen,dP}$  when the mass flow rate is high.

#### 4.4 SENSITIVITY ANALYSIS

The following sections deal with the sensitivity of the numerical code to some of the initial parameters. In literature two possible equations were found for the sky temperature. The effect of implementing the alternative equation is investigated. The wind velocity was chosen as 2 m/s for initial modelling. The effect of increasing the velocity is investigated.

Furthermore, the maximum focused heat energy was taken as 2 000 W/m. The effect of increasing this value to 3 000 W/m is investigated. For larger diameters, this is quite possible to achieve but conversely, for smaller diameters, the required concentration ratio might be too large and in practice one would not be able to achieve this amount of focused energy. But keep in mind that the sensitivity is used to see if optimal conditions remain optimal regardless of changes in parameters. In other words, numerical values for the entropy generation are of less

## CHAPTER 4. RESULTS

importance than maxima and minima. Finally, the effect of changing the glass cover clearance is investigated.

Note that the following sections only depict results for a mass flow rate of  $\dot{m} = 0.2 \text{ kg/s}$  and a diameter of  $D_i = 25 \text{ mm}$ . Additional graphs for other conditions can be viewed in Appendix A. These graphs show that the assessments made in the following sections are true for other operating conditions as well, such as different mass flow rates and diameters.

### 4.4.1 Sky Temperature

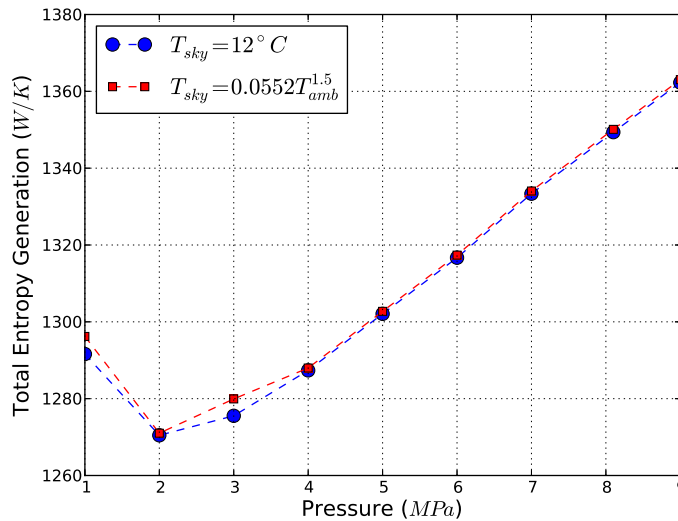


Figure 4.10: Effects of changing the effective sky temperature on the total entropy generation for different operating pressures, where  $D_i = 25 \text{ mm}$  and  $\dot{m} = 0.2 \text{ kg/s}$ .

From literature, two possible equations were found to determine the effective sky temperature. The first equation calculates the sky temperature as  $8^\circ C$  below the ambient temperature and the second equation is stated in Figure 4.10 and calculates the effective sky temperature as  $3.91^\circ C$  for an ambient temperature of  $20^\circ C$ .

From Figure 4.10, it can be seen that the change does not effect the total entropy generation significantly. Pressures  $1 \text{ MPa}$  and  $3 \text{ MPa}$  are slightly more affected than the other operating pressures. More importantly, the change does not affect the shape and therefore the optimal condition remains optimal.

### 4.4.2 Wind Velocity

From Figure 4.11, it can be seen that increasing the wind velocity to  $4 \text{ m/s}$  has the effect of increasing the entropy generation. This is due to the fact that more heat losses are prevalent

CHAPTER 4. RESULTS

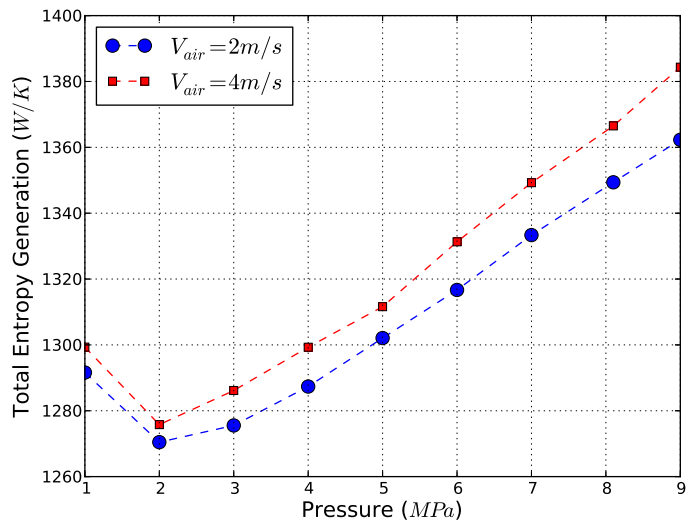


Figure 4.11: Effects of changing the wind velocity on the total entropy generation for different operating pressures, where  $D_i = 25 \text{ mm}$  and  $\dot{m} = 0.2 \text{ kg/s}$ .

throughout the receiver tube due to higher convection losses.

It can also be seen that for an operating pressure of  $2 \text{ MPa}$ , the total entropy generation remains at a minimum. It can be concluded that the wind velocity only contributes to the shifting of the graph and not change the actual shape and thus that the optimal operating conditions remain the optimal regardless of wind velocity.

### 4.4.3 Maximum Focused Heat

As mentioned before, the maximum amount of focused heat on the receiver was taken as  $2\,000 \text{ W/m}$ . The corresponding concentration ratio to achieve this was also given in Table 3.3. Increasing the amount of focused heat means that the concentration ratio must also increase. Table 4.4 gives the concentration ratios for the scenario where  $Q_{sun}$  is increased to  $3\,000 \text{ W/m}$ . For the small diameters ( $15 \text{ mm}$  and  $20 \text{ mm}$ ), one might not be able to achieve such a high concentration ratio but for larger diameters, the concentration ratio is quite achievable.

When investigating Figure 4.12, it can be seen that if the maximum heat is increased from  $2\,000 \text{ W/m}$  to  $3\,000 \text{ W/m}$ , the entropy generation is also decreased considerably. This is mainly due to the total length of the receiver being much shorter due to the fact that more heat is focused per unit length. However, it must be noted also that the optimum does shift as well. The  $Q_{sun} = 2\,000 \text{ W/m}$  condition achieves a minimum at  $2 \text{ MPa}$  whereas the  $Q_{sun} = 3\,000 \text{ W/m}$  condition achieves a minimum at  $3 \text{ MPa}$ .

CHAPTER 4. RESULTS

---

Table 4.4: Concentration ratios for the larger amount of focussed heat of  $Q_{sun} = 3000 W$  and  $S_r = 720W/m^2$ .

$D_i$ $m$	$D_o$ $m$	$A_s$ $m^2$	$q_{sun}$ $kW/m^2$	$C_R = q_{sun}/S_r$ -
0.015	0.019	0.05969	50.26	70
0.02	0.024	0.0754	39.79	55
0.025	0.029	0.0911	32.93	46
0.03	0.034	0.10681	28.09	39
0.05	0.054	0.16965	17.68	25

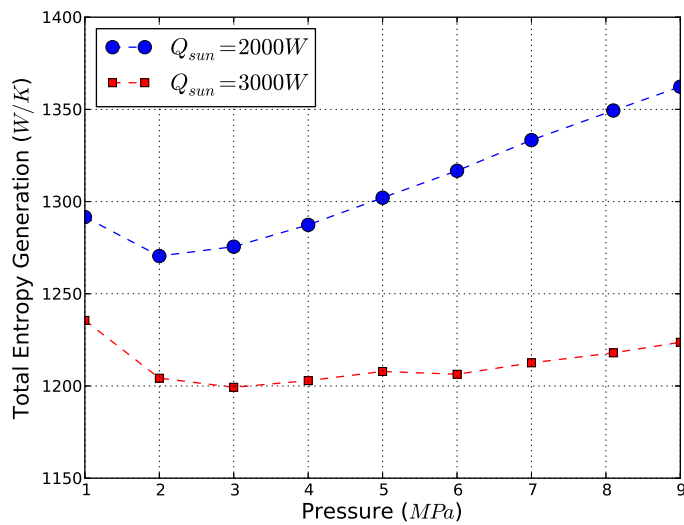


Figure 4.12: Effects of changing the maximum focused heat per unit section on the total entropy generation for different operating pressures, where  $D_i = 25 mm$  and  $\dot{m} = 0.2 kg/s$ .

#### 4.4.4 Glass Cover Clearance

Increasing the glass cover clearance increases the exposed outer heat transfer area and thus increases the losses and entropy generation. This is validated by Figure 4.13. It can be concluded that smaller glass cover clearances are more effective in lowering the entropy generation. However, it is also seen that as with the effective sky temperature as well as the wind velocity, the optimal point does not shift and therefore changes in glass cover clearance will not affect the optimal operating condition.

CHAPTER 4. RESULTS

---

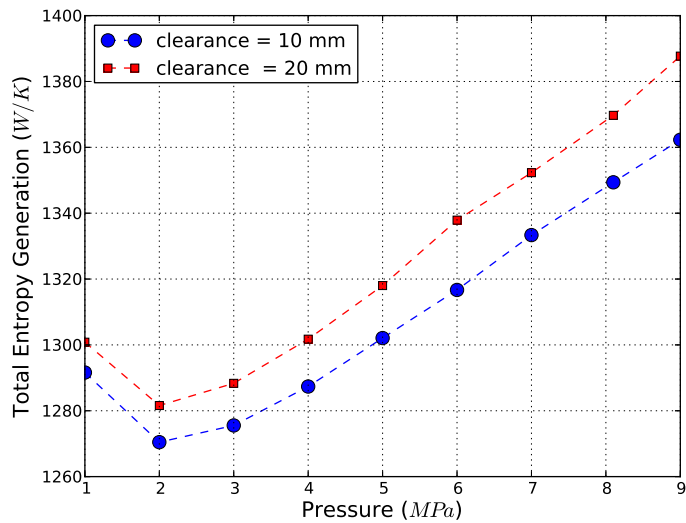


Figure 4.13: Effects of changing the glass cover clearance on the total entropy generation for different operating pressures, where  $D_i = 25 \text{ mm}$  and  $\dot{m} = 0.2 \text{ kg/s}$ .

## 4.5 CONCLUSION

In this section, various operating pressures were investigated. Mass flow rates as well as diameters were varied and the effect on the entropy generation was investigated. Generally, small diameters increased  $S_{gen,dP}$  while decreasing  $S_{gen,dT}$ . Furthermore, larger mass flow rates increased the  $S_{gen,dP}$  contribution to the total entropy generation considerably.

A sensitivity analysis showed that the numerical model was robust and rather insensitive to the effective sky temperature. Furthermore, changing the wind velocity and glass cover clearance did not affect the respective minima, indicating that an optimal model will remain optimal regardless of glass clearance and wind. However, it is recommended that the glass clearance remain small to limit the exposed heat transfer area. It was also seen, however, that  $Q_{sun}$  is not completely insensitive to the change in operating conditions. The effects of  $Q_{sun}$  are investigated further in the next chapter.

---

---

# CHAPTER 5

---

## OPTIMISATION

### 5.1 BACKGROUND

Mathematical optimisation deals with the minimisation of a cost function  $f(X)$  (also known as an objective function) by obtaining an optimum set of design variables ( $X = [x_1, x_2, \dots, x_n]^T$ ). It can be stated mathematically as follows:

Find

$$X = [x_1, x_2, \dots, x_n]^T \quad (5.1)$$

such that

$$f(X) \quad (5.2)$$

is at a minimum.

The above formulation applies to an unconstrained optimisation problem. Often in engineering the problem is not unconstrained but the solution is limited by constraints which account for physical impossibilities or bounds that are beyond the scope of investigation or limited by the design.

Inequality constraints are formulated as follows:

$$g_i(X) \leq 0 \quad \text{where } i = 1, 2, 3, \dots, m \quad (5.3)$$

Equality constraints are formulated as follows:

CHAPTER 5. OPTIMISATION

---

$$h_j(X) = 0 \quad \text{where } j = 1, 2, 3, \dots, p \tag{5.4}$$

The problem might not always contain both inequality and equality constraints. Furthermore, it should be recognised that a maximisation problem can easily be written as a minimisation problem since  $f(X_{opt})$  for a minimisation problem is the same as  $-f(X_{opt})$  for a maximisation problem. A simple case concerning this is depicted in Figure 5.1.

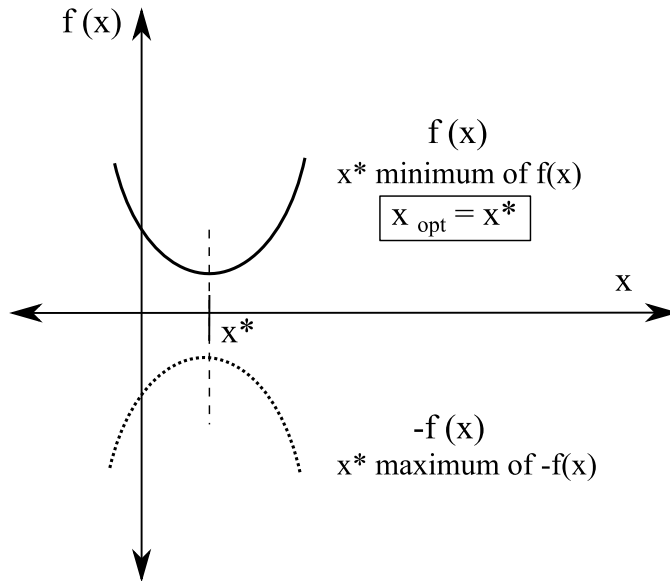


Figure 5.1: Similarity between a minimisation and maximisation problem.

Gradient-based methods can be very effective in finding solutions for optimisation problems provided they are used correctly. These methods evaluate the gradient of the function in order to estimate where possible extremities are located. Gradient-based approaches work best when the function is smooth and continuous and does not have multiple maxima and minima. When the analytical expression for the function derivative is not available or known, the definition can be used to estimate a value:

$$f'(a) = \lim_{h \rightarrow 0} \frac{f(a+h) - f(a)}{h} \tag{5.5}$$

Some modern optimisation techniques are based on biological behaviour and characteristics. These techniques often involve heaps of function evaluations to obtain an approximate or probable optimum. Brute-force-type optimisation algorithms only base their workings on the evaluation of the objective function and no information of the gradient is needed to perform these optimisations. These techniques are useful when multiple minima and maxima exist or when the objective function is discrete (Rao, 2009).

## 5.2 METHOD

It was seen in the previous chapter that the numerical model is sensitive to the available heat ( $Q_{sun}$ ) per unit metre. In this section, the maximum available heat ( $Q_{sun}$ ) is initially treated as a design variable. Furthermore, the diameter is also treated as a design variable. The total entropy generation is the cost function. A contour plot of the available heat and diameter gives insight into the behaviour of the system. Furthermore, a brute-force random optimisation algorithm, simulated annealing, is implemented due to the erratic nature of the cost function.

Increasing the mass flow rate inevitably increases the entropy generation, but it does not make sense to decrease the mass flow rate only to minimise the entropy generation, since this will also decrease the work that can be harnessed during expansion. Instead, one should conduct a multi-objective optimisation from which one can determine multiple optimal conditions depending on what the desired outcome is.

## 5.3 RESULTS

### 5.3.1 Contour Plot

Shown in Figure 5.2 is a contour plot for an operating pressure of 4 MPa and a mass flow of 0.2 kg/s. It can be seen that (without the constraints) the optimum region is located in the top left corner. This is where  $Q_{sun}$  is large and the receiver tube diameter is small, but not much smaller than  $D_i = 0.015$  m. When  $Q_{sun}$  is large, the total tube length is shorter, resulting in less entropy generation.

The black diagonal lines in Figure 5.2 signify the constraints pertaining to the concentration ratio ( $C_R$ ). The area below the lines is the feasible region. The constraint accounts for the maximum concentration ratio that can be achieved. For a concentration ratio of 50, this becomes:

$$C_R \leq 50 \quad (5.6a)$$

$$g(X) - 50 \leq 0 \quad (5.6b)$$

It can be seen that if  $C_R$  is increased,  $S_{gen,tot}$  can be lowered, and the diagonal line shifts closer to the optimal region. At lower diameters, it can be seen that  $S_{gen,dP}$  mostly contributes to the total entropy generation. Conversely, at larger diameters, only  $S_{gen,dT}$  is significantly contributing to  $S_{gen,tot}$ . From Figure 5.2, it can be seen that the optimum is located along  $g(X)$ . This is due to the fact that the maximum concentration ratio results in the maximum amount of focused heat. The contour lines at values larger than  $D_i = 0.015$  m have a smaller gradient, indicating that  $S_{gen,tot}$  becomes smaller as the diameter increases. This can be validated by Figure 5.3.

CHAPTER 5. OPTIMISATION

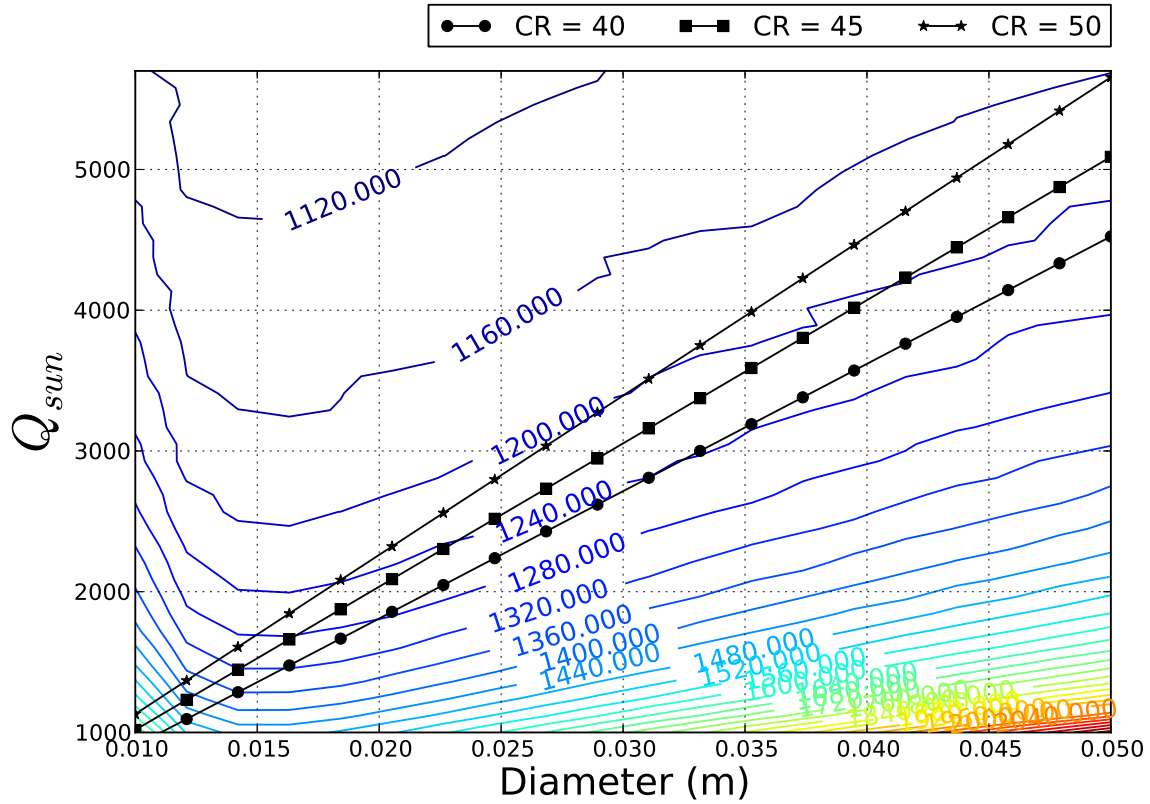


Figure 5.2: Contour plot for the base case parameters of 4 MPa and  $\dot{m} = 0.2 \text{ kg/s}$ .

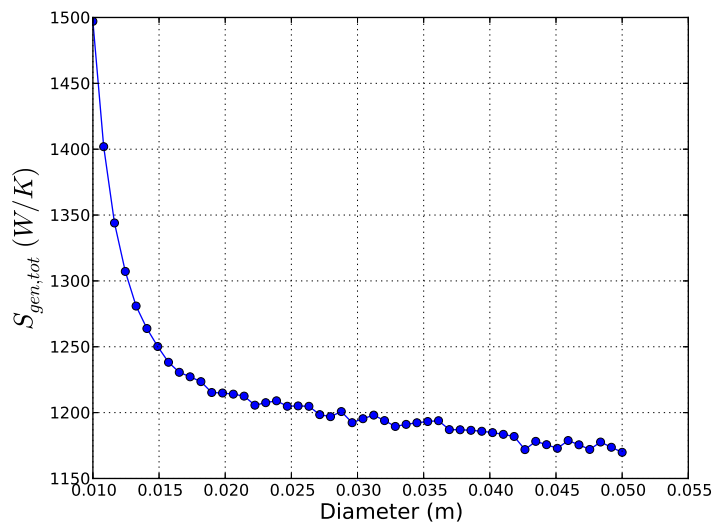


Figure 5.3: One dimensional plot of function values along the constraint  $g(X) = 45$ .

CHAPTER 5. OPTIMISATION

From Figure 5.3, it can also be seen that increasing the diameter from 30 mm to 50 mm only marginally affects the entropy generation ( $S_{gen,tot} = 1195 \text{ W/K}$  at  $D_i = 0.03 \text{ m}$ , and  $S_{gen,tot} = 1170 \text{ W/K}$  at  $D_i = 0.05 \text{ m}$ ). It is unfeasible to increase the diameter indefinitely only to minimise the entropy generation. It would be more advantageous to choose the smallest diameter for which the consecutive function value does not decrease significantly (say beyond 1%). Thus the smallest adequate diameter is chosen as the optimal.

The second question that arises is whether the gradient of the contour lines will ever be larger than the gradient of the constraint function ( $g(X)$ ). If this is indeed the case, a minimum can be achieved within the bounds. From the previous chapter, it was seen that the operating pressure indeed influences the rate at which  $S_{gen,tot}$  increases since a higher temperature means more losses due to  $S_{gen,dT}$ .

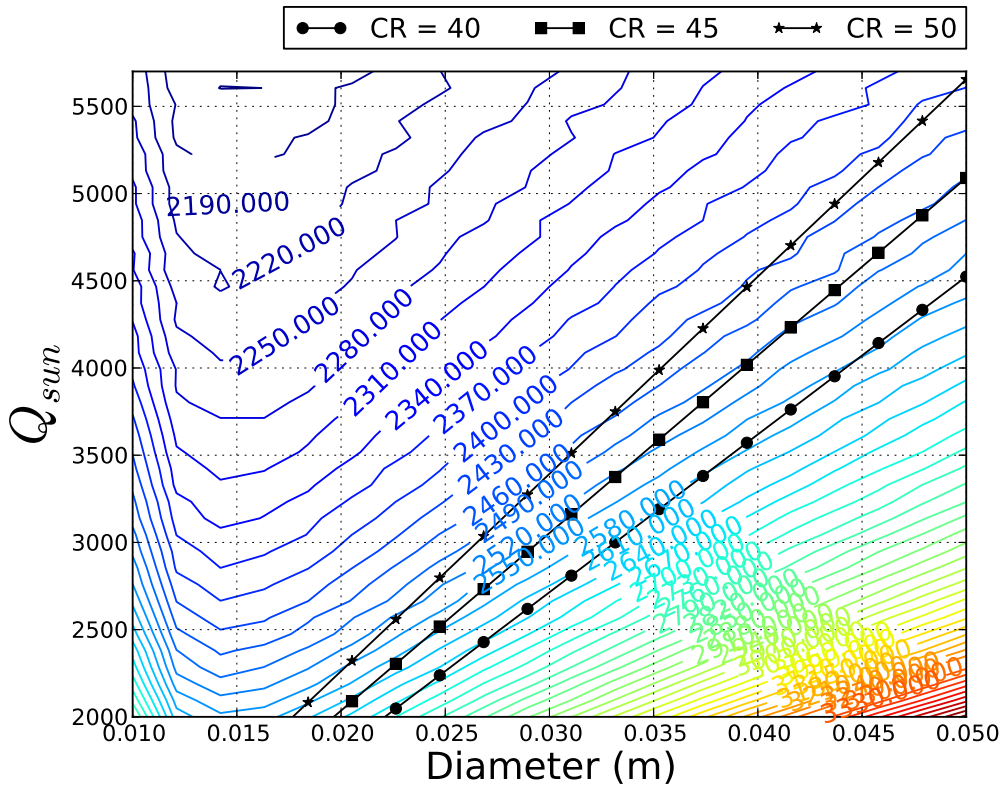


Figure 5.4: Contour plot for the high operating pressure and high mass flow rate (10 MPa and  $\dot{m} = 0.4 \text{ kg/s}$ ).

To see whether the contour gradient will ever surpass the constraint gradient, Figure 5.4 is shown for an operating pressure of 10 MPa. For this condition, the saturation temperature is at 310°C and the turbine inlet at 372°C. It can indeed be seen that the gradient of the contours beyond  $D_i = 0.015 \text{ m}$  is larger than that of Figure 5.2. However, it still does not surpass the gradient of the constraint functions shown.

### 5.3.2 Results for Simulated Annealing Optimisation

From the contour plots (Figure 5.2 and Figure 5.4) as well as Figure 5.3, it can be seen that the objective function is not entirely smooth. Due to the numerical nature of the function, values fluctuate around the general curves and surfaces. Due to this, a gradient-based method will be inadequate for the optimisation. By using Python and SciPy, a simulated annealing (SA) optimisation method can be implemented. This method is based on the process of annealing molten metal. In a molten state, atoms in the liquid metal can move freely. However, as the metal is cooled to reach a solid state, the movement of the atoms become more and more restricted. If the metal is cooled too quickly, the proper crystalline state cannot be achieved. The process of cooling a metal to a proper crystalline state that has a low internal energy is known as annealing. The cooling process is analogous to the process of attaining a minimum function value in simulated annealing. (Rao, 2009; Scipy Community, 2011)

The simulated annealing method uses no gradient information but only utilises function evaluations. The algorithm is also very effective in dealing with discrete functions. If  $f(X_i) > f(X_{i+1})$  then  $f(X_{i+1})$  is accepted since it has a better (smaller) function value. If  $f(X_{i+1}) > f(X_i)$  that means  $f(X_{i+1})$  is worse than for the initial design vector ( $X_i$ ). Conventionally, one would reject values that are worse but in simulated annealing the value has a probability of being accepted. This probability can be described by the Boltzmann probability distribution given in Equation 5.7.

$$P_{bz}(E_{bz}) = e^{-E_{bz}/k_{bz}T} \quad (5.7)$$

Where  $E_{bz}$  is the energy of the system, T is the temperature and  $k_{bz}$  is the Boltzmann constant that can be chosen as unity for simplicity. The energy at a state  $i$  is given by the function evaluation at  $i$ :

$$E_{bz,i} = f(X_i) \quad (5.8)$$

The rate of convergence can be controlled by controlling the temperature. At high temperatures, there are higher probabilities for accepting the larger function value, whereas at low temperatures, there are lower probabilities for accepting the larger (worse) function value. Three factors are of importance when considering to conduct a simulated annealing optimisation: the number of iterations before reducing the temperature (n), the initial temperature ( $T_0$ ) and the reduction factor (c). Choosing values for these parameters often involve some trial-and-error procedures. The initial temperature can be specified or calculated by the SciPy function itself as 1.2 times the largest function deviation over randomly selected points. The reduction factor (c) should be between zero and one with 0.5 a good initial value. Large values of c will require more computational time whereas too small values for c might result in inadequate exploration of the design space. The results as obtained with the simulated annealing function is shown in Table 5.1. The bounds were set as follows:

CHAPTER 5. OPTIMISATION
 

---

$$10 \text{ mm} \leq D_i \leq 50 \text{ mm}$$

$$0.15 \text{ kg/s} \leq \dot{m} \leq 0.4 \text{ kg/s}$$

$$1 \text{ MPa} \leq P \leq 10 \text{ MPa}$$

 Table 5.1: Global optimum for design vector  $X = (D_i, \dot{m}, P)$  ( $T_0 = 2\,000$ ,  $n = 200$ ,  $c = 0.6$ ,  $k = 2$ ).

Parameter	Optimal
$D_i$	44.6 mm
$\dot{m}$	0.1513 kg/s
Pressure	7.62 MPa
$S_{gen,tot}$	899.14 W/K

It can be seen that the approximate optimum is located near the upper bounds for the diameter (bound is located at  $D_i = 50 \text{ mm}$ ) as well as the lower bound for the mass flow rate (bound is located at  $\dot{m} = 0.15 \text{ kg/s}$ ). This is in agreement with the previous findings in that the lowest mass flow rate results in the smallest entropy generation and the largest diameter is associated with the least entropy generation. Note that simulated annealing is partly random and two implementations of the same initial conditions and setting might result in slightly different outcomes. It was also seen that  $S_{gen,tot}$  is in the range of 900 W/K as a minimum and sensitive to mass flow but not extremely sensitive to diameter changes. In other words, the SA algorithm might converge to a smaller diameter but usually remains close to the lower mass flow. The lowest cost function values are seen to be in the vicinity of 900 W/K. The settings were chosen to have a reasonable convergence time yet also explore the entire design space. As a second initiative, the mass flow and diameter are fixed to only optimise the operating pressure. The results are shown in Table 5.2. Note that the initial settings had to be adjusted for these runs as well.

 Table 5.2: Optimum pressure for various mass flow rates, where  $D_i = 20 \text{ mm}$ .

Mass flow (kg/s)	Optimal pressure (MPa)	$S_{gen,tot}$ (W/K)
0.15	3.597	903
0.2	3.815	1211
0.25	3.948	1523
0.3	4.68	1838
0.35	5.47	2156
0.4	6.715	2478

From Table 5.2, it can be seen that the optimum pressure increases as the mass flow rate increases. The entropy generation tends to increase more or less linearly while the optimum

---

CHAPTER 5. OPTIMISATION

---

pressure tends to be higher than expected for higher mass flow rates. In the next section, the effect of the operating pressure on the work is investigated.

### 5.3.3 Multi-Objective Optimisation

A good way to represent multiple optimal points is by implementation of a Pareto graph. Figure 5.5 shows an example of Pareto optimal solutions for two objective functions  $f_1$  and  $f_2$ . Note that for the graph shown in Figure 5.5, both functions must be minimised. If  $f_2$  is decreased,  $f_1$  increases, therefore the optimal solution consists of a range of solutions depending on what the ultimate goal is. If it is the desire to have a small value for  $f_1$  and  $f_2$  is of less importance, then conditions to achieve this can be located at the upper regions of the curve. The optimal parameters can be chosen as to have adequate values for  $f_1$  and  $f_2$ .

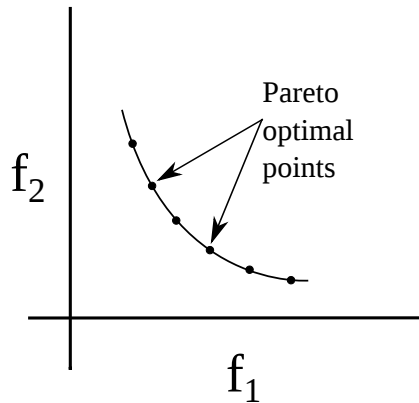


Figure 5.5: Example of a Pareto diagram for two objective functions.

The mass flow rate influences the entropy generation in two ways, firstly, the mass flow inevitably increases the entropy generation but what should be realised is that higher mass flow rates also increases the work output of the plant. Secondly, higher mass flow rates also tend to increase the  $S_{gen,dP}$  contribution. Care must be taken to not incorporate a high mass flow ( $\dot{m} = 0.4 \text{ kg/s}$ ) with a small diameter (smaller than 15 mm) since this will have the effect of excessive  $S_{gen,dP}$  contributions.

Figure 5.6 shows how the optimality is influenced by the mass flow rate as well as the operating pressure for a diameter of  $D_i = 20 \text{ mm}$  (note that a similar graph for a large diameter of  $D_i = 50 \text{ mm}$  is shown in Appendix A). The work output can now also be viewed as a cost function, in addition to the entropy generation cost function. Note that the work must be maximised and the entropy must be minimised, therefore the plot in Figure 5.6 has a different form than that shown in Figure 5.5. The various operating pressures are not indicated in Figure 5.6 but rather shown in a zoomed-in version of Figure 5.6 in Figure 5.7. Figure 5.7 is a zoomed-in figure for the highest mass flow rate to show that the maximum work will increase as the operating pressure increases. From Figure 5.7, it can be seen that operating pressures lower than 3 MPa tend to generate more entropy. Pressures higher than this have more or less the same performance when considering the entropy generation. However, it can clearly be seen

CHAPTER 5. OPTIMISATION

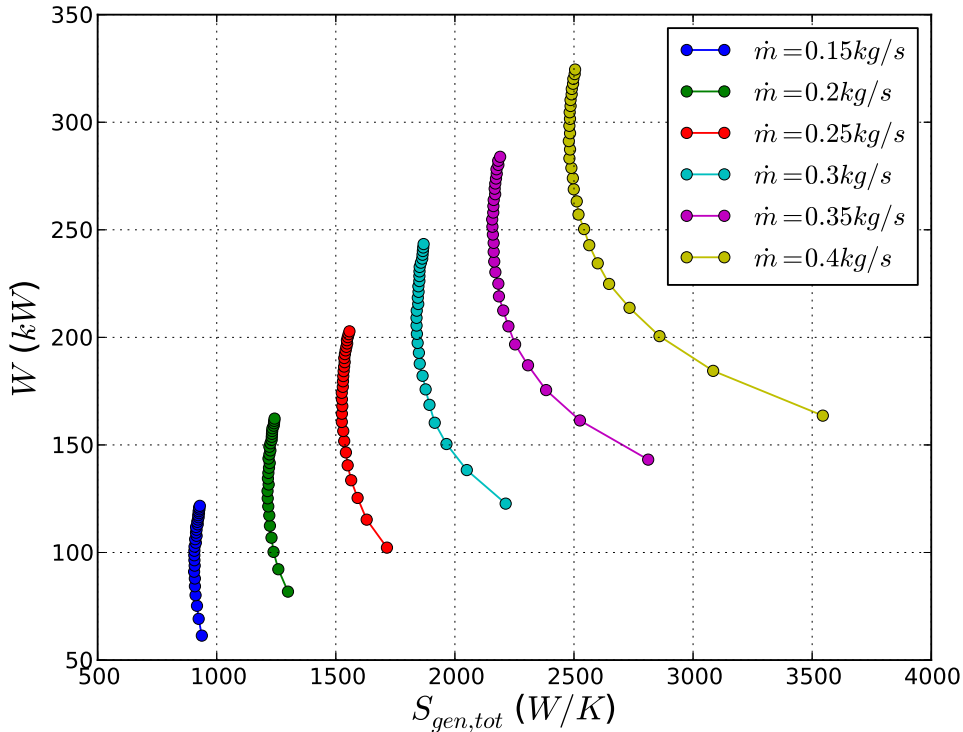


Figure 5.6: Maximum work output ( $kW$ ) vs total entropy generation ( $W/K$ ) for a fixed diameter of  $D_i = 20 \text{ mm}$  and various mass flow rates.

that higher pressures have a more advantageous effect on the maximum work output that can be achieved while having a small to negligible effect on the total entropy generation. It is therefore recommended that if the work output is of more importance, the higher operating pressures should be chosen to maximise this function.

## 5.4 CONCLUSION

In this chapter, it was seen that the concentration ratio will have a significant influence on the entropy generation. For a higher concentration ratio more optimality can be achieved. In further investigations, the concentration ratio was fixed. A simulated annealing (SA) optimisation algorithm (available in SciPy) was implemented and performed. This algorithm had more success in capturing the global minima since the function values had a tendency to fluctuate. As an initial step, the optimisation was performed for three design variables. From this analysis, it was seen that certain design variables only tended to the bounds. As a second step, these variables were fixed and the operating pressure was optimised for various mass flow rates. Optimal operating pressures tended to increase as the mass flow rate increased.

CHAPTER 5. OPTIMISATION

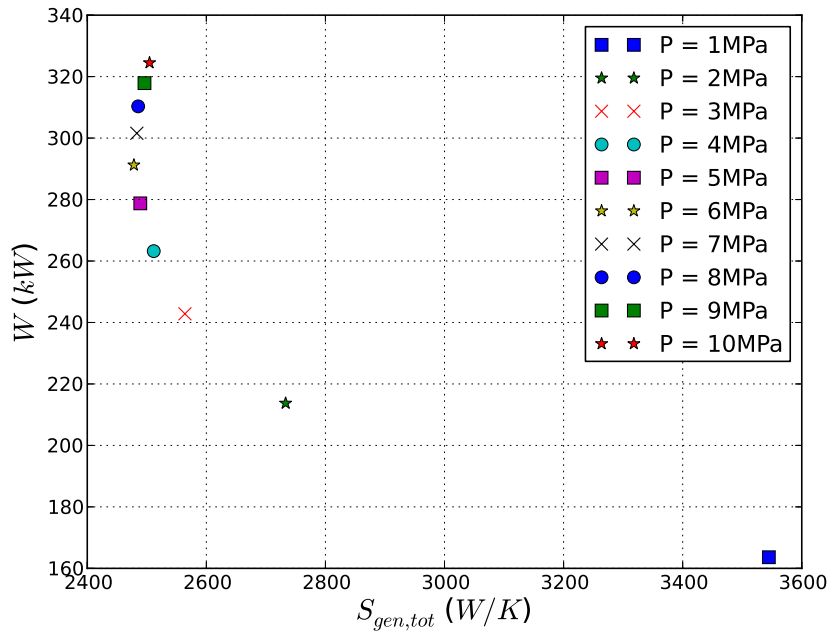


Figure 5.7: Maximum work output ( $kW$ ) vs total entropy generation ( $W/K$ ) for highest mass flow ( $\dot{m} = 0.4 \text{ kg/s}$ ).

In the final section in this chapter, the maximum work output is plotted against the entropy generation to locate multiple optimal conditions.

---

---

# CHAPTER 6

---

## CONCLUSION

### 6.1 DISCUSSION

In this dissertation the entropy generation in a parabolic trough receiver tube was investigated. Entropy generation in the receiver tube can mainly be attributed to the heat losses to the surroundings ( $S_{gen,dT}$ ) as well as the losses due to internal fluid friction ( $S_{gen,dP}$ ). The receiver can be divided into three regions: a liquid region, a two-phase region and a vapour region. From the validation and base case analysis, it was seen that the two-phase region is very long for lower operating pressures. For higher operating pressures, the liquid region becomes longer. Fluid friction in the two-phase region tends to be larger than for the liquid region. From the validation case, it was also seen that the losses due to convection (forced) are much larger than those for the radiation losses.

Low mass flow rates and large diameters can have stratified flow in the two-phase region as a consequence. stratified flow ultimately lowers the heat transfer coefficient, hence stratified flow in the two-phase region is an unwanted phenomenon. Furthermore, dryout and misty regimes in the two-phase region also result in lower heat transfer coefficients. For high mass velocities, the receiver tube temperature stays close to the saturation temperature due to high heat transfer coefficients. This is very advantageous in terms of entropy minimisation. Further observations that were made from the base case validation are that the glass temperature stays well below the receiver temperature indicating that the vacuum tends to retain the heat quite well.

From the results chapter, it was seen that in most cases (but not all),  $S_{gen,dT}$  contributes more to the total entropy generation. This tendency is more prevalent for lower mass flow rates since higher mass flow rates increase  $S_{gen,dP}$ . Diameters should be chosen small but large enough to counter the excessive influence of  $S_{gen,dP}$ . Beyond a certain diameter, only  $S_{gen,dT}$  contributes. Effects of  $S_{gen,dP}$  become negligible for most cases beyond  $D_i = 20 \text{ mm}$ . The  $S_{gen,dT}$  contribution can be decreased if the diameter is increased and concentration ratio ( $C_R$ )

## CHAPTER 6. CONCLUSION

---

is kept at a constant value. If a pre-specified amount of the focused heat is considered to fall on the receiver tube ( $Q_{sun}$ ), it is always more advantageous to consider smaller diameters, beyond the point where  $S_{gen,dP}$  has an influence. But if the concentration ratio is kept at a constant value, larger diameters tend to decrease the entropy generation with small amounts. It is unfeasible to increase the tube diameter simply to decrease the entropy generation by negligible amounts. Therefore it can be recommended that if the increasing of the tube diameter results in negligible  $S_{gen,tot}$  minimisation, the larger tube diameter can be incorporated. Furthermore, higher concentration ratios always decrease the entropy generation since more heat is focused on the receiver pipe.

Due to the fluctuating nature of the objective function, simulated annealing optimisation (available in Python) was implemented to conduct an optimisation routine. From the optimisation, it was seen that the optimal operating pressure increases if the mass flow rate is increased. Optimal operating pressures can be achieved when considering only the entropy generation but when the thermodynamic work is taken into consideration, different conclusions can be drawn. Higher operating pressures increase the entropy generation but it is more advantageous when maximising the work. Higher operating pressures are more advantageous because they have a significant effect on maximizing the work but small to negligible effect on increasing  $S_{gen,tot}$ . Operating pressures lower than 3 MPa are not recommended since the pressure drops for these operating pressures become too large.

## 6.2 FUTURE WORK

A good way to achieve higher heat transfer coefficients is by means of heat transfer enhancement. This can decrease  $S_{gen,dT}$  by two ways. Firstly, due to the higher heat transfer coefficient on the inner-tube, more heat is transferred to the working fluid which also affects the overall length of the receiver tube. However, this also has the effect of increasing  $S_{gen,dP}$ . The extent of this influence can be investigated.

In this text, the losses through the bellows and structure were not taken into account, since they largely depend on plant layout. For more accurate estimations of the entropy generation, these losses can be investigated.

In solar energy application, two additional challenges often arise: overall cost and financial feasibility as well as the implementation of an effective energy storage unit. Effectively dealing with these challenges can be an important contribution in future research.

---

## REFERENCES

- Barlev, D., Vidu, R. and Stroewe, P. (2011). Innovations in concentrated solar power, *Solar Energy Materials and Solar Cells* **95**(27): 3–25.
- Bejan, A. (1982). *Entropy generation through heat and fluid flow*, Wiley London.
- Bejan, A. (1995). *Entropy generation minimization: The method of thermodynamic optimization of finite size systems and finite time.*, CRC Press.
- Bell, I. (2013). Coolprop.
- Cengel, Y. (2006). *Heat and mass transfer: a practical approach.*, McGraw Hill.
- Changhong, P., Yun, G., Suizheng, Q., Dounan, J. and Changhua, N. (2005). Two phase boiling heat transfer in two vertical narrow annuli, *Nuclear Engineering and Design* **235**: 1737–1747.
- Churchill, S. and Bernstein, M. (1977). A correlating equation for forced convection from gases and liquids to a circular cylinder in crossflow, *Journal of Heat Transfer* **99**: 300–306.
- Churchill, S. and Chu, H. (1975). Correlating equations for laminar and turbulent free convection from a horizontal cylinder, *International Journal of Heat and Mass Transfer* **18**(9): 1049–1053.
- Collier, J. and Thome, J. (1994). *Convective boiling and condensation*, Oxford University Press Inc.
- Eck, M., Zarza, E., Eickhoff, M., Rheinlander, J. and Valenzuela, L. (2003). Applied research concerning the direct steam generation in parabolic troughs, *Solar Energy* **74**: 341–351.
- Fluri, T. (2009). The potential of concentrating solar power in South Africa, *Energy Policy* **37**: 5075–5080.
- Forristall, R. (2003). Heat transfer analysis and modelling of a parabolic trough solar receiver implemented in engineering equation solver, *Technical Report*, National Renewable Energy Laboratory.
- Forsberg, C., Peterson, P. and Zhao, H. (2007). High temperature liquid-fluoride-salt closed cycle solar power towers., *Journal of Solar Energy Engineering* **129**: 141–164.

REFERENCES

---

- Garcia-Valladares, O. and Velazquez, N. (2009). Numerical simulation of parabolic trough collector: Improvement using counter flow concentric circular heat exchangers, *International Journal of Heat and Mass Transfer* **52**: 597–609.
- Gnielinsky, V. (1976). New equation for heat and mass transfer in turbulent pipe and channel flow, *International Chemical Engineering* **1**(2): 359–367.
- Kalogirou, S. (2004). Solar thermal collectors and applications, *Progress in Energy and Combustion Science* **30**: 231–295.
- Kalogirou, S. (2009). *Solar energy engineering: processes and systems*, Elsevier Inc.
- Kattan, N., Thome, J. and Favrat, D. (1998). Flow boiling in horizontal tubes: Part 1 - development of a diabatic two-phase flow pattern map, *Journal of Heat Transfer* **120**: 140–147.
- Koroneos, C., Spachos, T. and Moussiopoulos, N. (2003). Exergetic analysis renewable energy sources, *Renewable Energy* **28**: 295–310.
- Lunde, P. (1980). *Solar thermal engineering: space heating and hot water systems*, John Wiley & Sons Inc.
- Mills, D. (2004). Advances in solar thermal electricity technology, *Solar Energy* **76**(1-3): 19–31.
- Numpy Developers and Scipy Community (2011). Numpy.
- Odeh, S., Morrison, G. and Behnia, M. (1998). Modelling of parabolic trough direct steam generation solar collectors, *Solar Energy* **62**: 395–406.
- Pegels, A. (2010). Renewable energy in South Africa: potentials, barriers and options for support., *Energy Policy* **38**: 4945–4954.
- Price, H., Lupfert, E., Kearney, D., Zarza, E., Cohen, G., Gee, R. and Mahoney, R. (2002). Advances in parabolic trough solar power technology., *Journal of Solar Engineering* **124**: 109–125.
- Python Software Foundation (2011). Python.
- Rabl, A., Bendt, P. and Gaul, H. (1982). Optimization of parabolic trough solar collectors, *Solar Energy* **29**(5): 407–417.
- Rao, S. (2009). *Engineering optimisation: theory and practice 4th Edition*, John Wiley & Sons Inc.
- Ratts, E. and Raut, A. (2004). Entropy generation minimization of fully developed internal flow with constant heat flux, *Journal of Heat Transfer* **126**: 656–659.
- Reddy, K., Ravikumar, K. and Satyanarayana, G. (2008). Numerical investigation of energy-efficient receiver for solar parabolic trough concentrator, *Heat Transfer Engineering* **29**: 961–972.

REFERENCES

---

- Revellin, R., Lips, S., Khandehar, S. and Bonjour, J. (2009). Local entropy generation for saturated two-phase flow, *Energy* **34**: 1113–1121.
- Roesle, M., Coskun, V. and Steinfeld, A. (2011). Numerical analysis of heat loss from a parabolic trough absorber tube with active vacuum system, *Journal of Solar Engineering* **133**: 1–5.
- Rouhani, S. and Axelsson, E. (1970). Calculation of void volume fraction in subcooled and quality boiling regions, *International Journal of Heat and Mass Transfer* **13**: 383–393.
- Sahin, A. (2000). Entropy generation in turbulent liquid flow through a smooth duct subjected to constant wall temperature, *International Journal of Heat and Mass Transfer* **43**: pp 1469–1478.
- Scipy Community (2011). Scipy.
- Singh, N., Kaushik, S. and Misra, R. (2000). Exergetic analysis of a solar thermal power system, *Renewable Energy* **19**: 135–143.
- Thome, J. (2004). *Wolverine Tube Heat Transfer Data Book III*, Wolverine Tube Inc.
- Viebahn, P., Lechon, Y. and Trieb, F. (2011). The potential role of concentrated solar power (CSP) in Africa and Europe: a dynamic assesment of technology development, cost development and life cycle inventories until 2050., *Energy Policy* **39**: 4420–4430.
- Wojtan, L., Ursenbacher, T. and Thome, J. (2005a). Investigation of flow boiling in horizontal tubes: Part 1 - a new diabatic two-phase flow pattern map, *International Journal of Heat and Mass Transfer* **48**: 2955–2969.
- Wojtan, L., Ursenbacher, T. and Thome, J. (2005b). Investigation of flow boiling in horizontal tubes: Part 2 - development of a new heat transfer model for stratified-wavy, dryout and mist flow regimes, *International Journal of Heat and Mass Transfer* **48**: 2970–2985.
- Zurcher, O., Favrat, D. and Thome, J. (2002). Evaporation of refrigerants in a horizontal tube: an improved flow pattern dependent heat transfer model compared to ammonia data, *International Journal of Heat and Mass Transfer* **45**: 303–317.

---



---

# APPENDIX A

---

## ADDITIONAL GRAPHS

### A.1 TWO-PHASE FLOW VALIDATION

The following graph serves as a validation of the accuracy of the numerical model. The numerical data is compared with data obtained from Wojtan *et al.* (2005b). The larger deviations between qualities 0 and 10% as well as 70% and 90% can be attributed to rounding errors and property deviations.

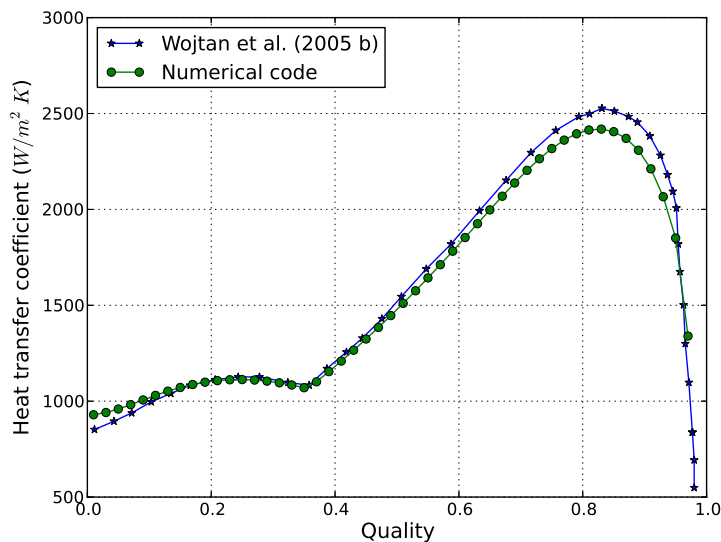


Figure A.1: Two-phase flow validation for R22,  $\dot{G} = 150 \text{ kg/m}^2\text{s}$ ,  $D_i = 13.84 \text{ mm}$ ,  $T_{sat} = 5^\circ\text{C}$  and  $q = 3.6 \text{ kW/m}^2$ .

APPENDIX A. ADDITIONAL GRAPHS

A.2 SENSITIVITY ANALYSIS

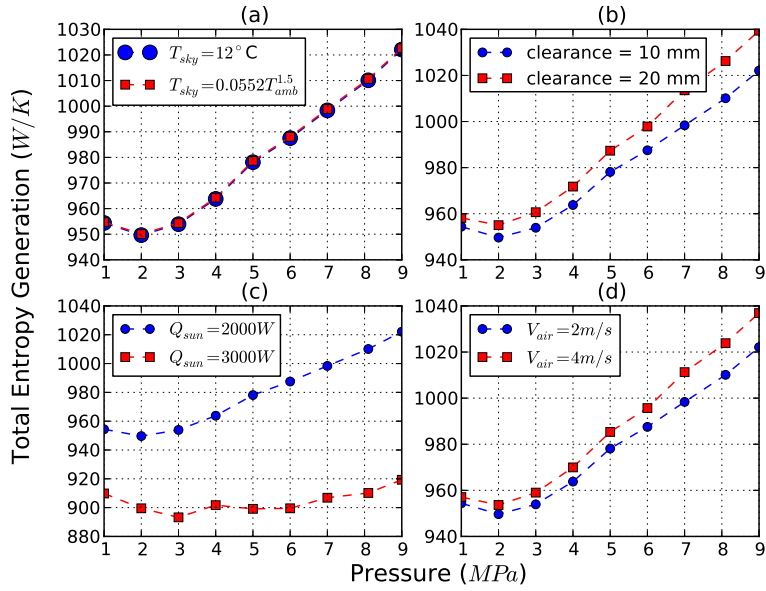


Figure A.2: Sensitivity analysis results at a low mass flow rate of  $\dot{m} = 0.15 \text{ kg/s}$  ( $D_i = 25 \text{ mm}$ ).

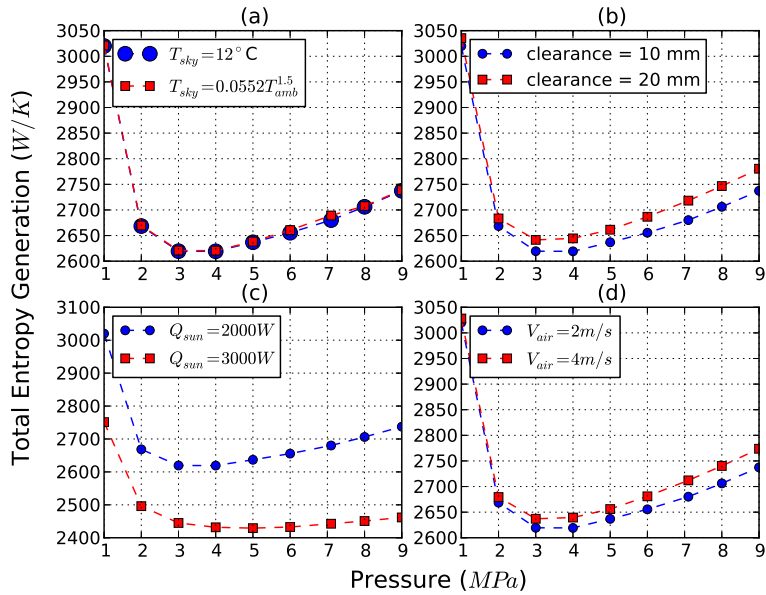


Figure A.3: Sensitivity analysis results at a high mass flow rate of  $\dot{m} = 0.4 \text{ kg/s}$  ( $D_i = 25 \text{ mm}$ ).

APPENDIX A. ADDITIONAL GRAPHS

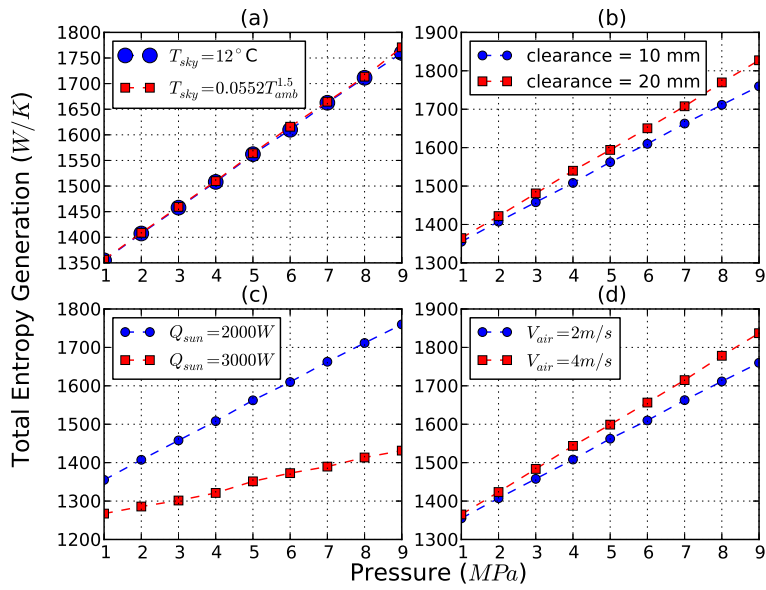


Figure A.4: Sensitivity analysis results at a large diameter of  $D_i = 50\text{mm}$  and moderate mass flow of  $\dot{m} = 0.2\text{ kg/s}$ .

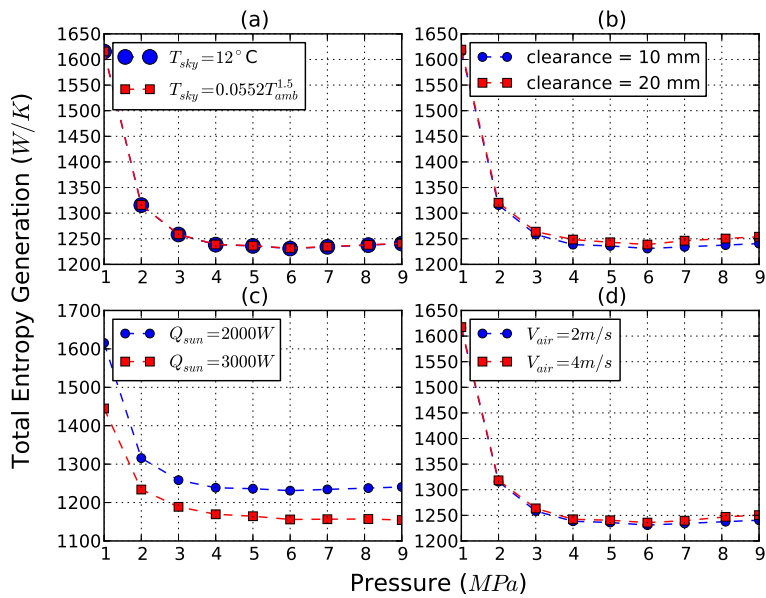


Figure A.5: Sensitivity analysis results at a small diameter of  $D_i = 15\text{mm}$  and moderate mass flow of  $\dot{m} = 0.2\text{ kg/s}$ .

APPENDIX A. ADDITIONAL GRAPHS

A.3 MULTI-OBJECTIVE OPTIMISATION

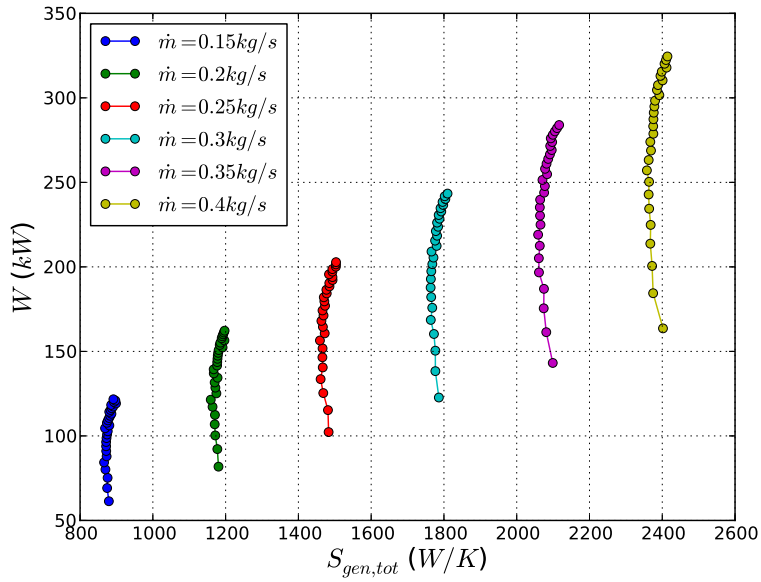


Figure A.6: Maximum work output ( $kW$ ) vs total entropy generation ( $W/K$ ) for a large diameter of  $D_i = 50 \text{ mm}$  and various mass flow rates.